GALLIE DAY 2023
ORAL PRESENTATIONS
TABLE OF CONTENTS

Translational Research

COMPREHENSIVE GENOMIC CHARACTERIZATION OF CDKN2A ALTERATIONS IN MENINGIOMAS

Justin Z. Wang[1,2] (SSTP), Vikas Patil[1,3], Farshad Nassiri[1,2,3], Gelareh Zadeh[1,2,3]

[1] MacFeeters Hamilton Neuro-Oncology Program, Princess Margaret Cancer Centre, University Health Network and University of Toronto, ON, Canada

[2] Division of Neurosurgery, Department of Surgery, University of Toronto, Toronto, ON, Canada

[3] Princess Margaret Cancer Centre, University Health Network, Toronto, ON, Canada

INTRODUCTION: Meningiomas are the most common brain tumor in adults.[1] Though the majority of meningiomas are benign, 20-30% are clinically aggressive and treatment refractory.[2-5] Compared to benign meningiomas, aggressive meningiomas harbour more copy number changes including focal deletions.[2,6] In particular, homozygous deletion (homodel) of the cyclin-dependent kinase inhibitor 2A (CDKN2A) gene on chromosome 9p21 have been associated with significantly shorter time to progression and is now a diagnostic criterion for grade 3 meningiomas.[7-11] However, even in cohorts enriched for high grade meningiomas, CDKN2A homodel is rare, reported in only 1.7-6.7% of patients and therefore requires large molecular datasets to effectively study.[2,8,12] Furthermore, the relationship between CDKN2A mRNA expression and clinical outcome, particularly for meningiomas without any CDKN2A deletions, appears to be more complex and has yet to be studied. This prompted us to comprehensively examine CDKN2A alterations in meningiomas using the largest combined cohort of previously published and unpublished multiomics datasets.[13,14]

METHODS: 1577 unique, clinically annotated meningiomas with matched molecular data were used in this study. We used 121 tumors from Toronto (Canada) with previously published multiplatform genomic and epigenomic data as the discovery cohort, 75 new samples from Tübingen (Germany) and publicly available data from recently published studies by Bayley et al. and Choudhury et al. comprised of 109 and 565 meningiomas as the “transcriptomic validation cohorts” given the availability of matched RNAseq data for these cases (N=109, N=185 in the Bayley et al. and Choudhury et al. respectively).[13,14] 567 meningiomas from the DKFZ (Germany) and 140 meningiomas from a separate independent institution with only DNA methylation data, both processed on the Illumina 450K array were included as validation cohorts for CDKN2A loss. 71 meningiomas from the DKFZ enriched for CDKN2A homodel (n=29/71, 41%) were used for p16 (the CDKN2A gene product) immunohistochemistry (IHC). Processing of DNA methylation, RNAseq, whole exome sequencing, and proteomics data were performed as previously published.[3] Copy number alterations were inferred from the methylation data using conumee.[15,16] Determination of CDKN2A deletion status were through manual inspection of genome-wide copy number variation (CNV) plots. For meningiomas without CDKN2A deletions, tumors with CDKN2A expression Z-score ≥ 1 in each cohort were designated as meningiomas with high CDKN2A expression ($CDKN2A^{high}$), while the remaining were designated to have low expression ($CDKN2A^{low}$). IHC using p16 antibody (Purified Mouse Anti-Human p16 antibody, component 51-1325GR) were carried out on 5 µm paraffin sections. Positivity was recorded in a semiquantitative manner based on the proportion of stained neoplastic cells (nuclear and cytoplasmic staining): 0 (0 positive cells), +1 (1-9% positive), +2 (10-69%), and +3 (>70%) by two experienced neuropathologists. Functional studies were performed using primary meningioma cell lines: mng_20, mng_50, mng_84, mng_46 and CH157 (CH-157MN; RRID:CVCL_5723) and IOMM-Lee (RRID:CVCL_5779) immortalized meningioma cell lines treated with CDK4/6 inhibitors palbociclib and abemaciclib (InvivoChem catalogue No. V1531, V1547), following which, cell viability was assessed using the CellTitre-Glo assay.

RESULTS: Overall CDKN2A deletion was rare, present in only 108 of 1506 patients (7.1%, excluding the IHC cohort) (**Fig 1a-d**). Three different patterns of CDKN2A loss were noted in

both the homodel and heterodel groups: 1) focal loss of the CDKN2A locus without loss of 9p, 2) loss of CDKN2A locus and a segment of 9p, and 3) loss of the entire 9p including the CDKN2A locus (**Fig 1b-e**). The degree of associated 9p loss did not appear to significantly alter the outcomes of meningiomas with CDKN2A homodel or heterodel (**Fig 1f,g**). Meningiomas with CDKN2A deletions appeared to have worse outcomes than CDKN2A intact/wt meningiomas in each molecular group (MG) except for MG4 (**Fig 1h**). When present, CDKN2A deletions (homodel and heterodel) were associated with significantly poorer PFS compared to CDKN2A intact/wt meningiomas (**Fig 1i-l**). There were no significant differences in the PFS of patients whose meningiomas had CDKN2A/B homodel vs heterodel in any cohort (**Fig j-l**).

As CDKN2A and CDKN2B mRNA expression highly correlated with one another (Pearson correlation R=0.79, $p=8.4x10^{-27}$; R=0.68, $p=3.0x10^{-34}$), we focused our subsequent analysis on CDKN2A expression (**Fig 1m,n**). Meningiomas with CDKN2A homodel had significantly lower CDKN2A mRNA expression compared to CDKN2A intact cases (**Figure 1o, p**). Meningiomas with CDKN2A heterodel had a more heterogenous level of mRNA expression.

As most meningiomas do not have any CDKN2A/B deletions, to facilitate between group comparisons within this cohort, we dichotomized CDKN2A intact meningiomas into 2 transcriptomic groups in each cohort based on their CDKN2A mRNA expression (**Fig 2a**), hereafter referred to as $CDKN2A^{high}$ and $CDKN2A^{low}$. On KM survival analysis, $CDKN2A^{low}$ meningiomas had the longest PFS, significantly better than both CDKN2A homo/heterodel and $CDKN2A^{high}$ meningiomas (**Fig 2b,c**). This finding also appeared to hold true within each WHO grade (**Fig 2d**). When controlling for other covariates, we found that higher CDKN2A mRNA expression was independently associated with poorer PFS (HR 1.25, 95% CI 1.04-1.49, p = 0.015) on multivariable Cox regression analysis. When meningiomas were classified into different molecular (MG) or methylation groups (MenG, MethG), regardless of group designation, CDKN2A mRNA expression increased with increasing biological aggressiveness of the groups as well as with increasing WHO grade (**Fig 2e-h**). When differential RNAseq analysis was performed comparing $CDKN2A^{high}$ to $CDKN2A^{low}$ meningiomas, there was significant upregulation of pathways involved in mitoses, cell cycling, cell cycle control (particularly at the G1-S transition), and apoptosis in $CDKN2A^{high}$ meningiomas consistent across all cohorts (**Fig 2i-l**). Although $CDKN2A^{high}$ meningiomas and meningiomas with CDKN2A deletions (homodel/heterodel) were mutually exclusive groups in our study, meningiomas with either alteration had poorer clinical outcomes. Therefore, we wanted to determine whether similar transcriptomic pathways may underlie this shared biological aggressiveness. Indeed, we saw significant up-regulation of nearly analogous cell cycle pathways in meningiomas with CDKN2A deletions as we observed in $CDKN2A^{high}$ meningiomas except these pathways generally centered around the G2M checkpoint/transition (**Fig 2m-o**).

In investigating whether DNA methylation changes could be associated with changes in CDKN2A mRNA expression, we found that CDKN2A promoter methylation was not significantly different between $CDKN2A^{high}$ and $CDKN2A^{low}$ meningiomas. However, there was hypermethylation of the CDKN2A gene, particularly at the gene body and 3' untranslated region (UTR) of $CDKN2A^{high}$ meningiomas compared to $CDKN2A^{low}$ tumors across all cohorts. Whether this represents a regulatory mechanism or is simply a passenger event in the context of global hypermethylation routinely seen in more biologically aggressive meningiomas is uncertain. To determine whether elevated CDKN2A could be related to copy number amplification at these gene loci, we generated and inspected genome-wide copy number profiles for each case. There were no $CDKN2A^{high}$ meningiomas with copy number gain of 9p at the chromosomal arm level or at the CDKN2A gene. When we correlated known meningioma driver mutations with CDKN2A deletions, *TERT* promoter (*TERTp*), *ARID1A*, and *PTEN* mutations were all associated with increased odds of having a CDKN2A deletion, although the latter two mutations are exceedingly rare in meningiomas. In the cohort of only CDKN2A intact/wt meningiomas, although having a *SMARCB1* or *RB1* mutation appeared to be associated with increased odds of having a

CDKN2A^{high} meningioma, these did not reach statistical significance and may be confounded by the relative rarity of particularly RB1 mutations in our cohort (and in meningiomas in general).

As the final step in the central dogma, we wanted to determine whether changes in gene expression of CDKN2A translated to differences in protein abundance. Overall p16 (the gene product of CDKN2A) levels appeared to increase with more aggressive MG, with MG4 meningiomas having the highest levels (**Fig 3a**), concordant with our mRNA expression data. When meningiomas were stratified by WHO grade, p16 also appeared to increase with higher WHO grade. p16 protein levels also showed a significant positive correlation with CDKN2A mRNA expression (**Fig 3d**). When p16 IHC were performed to confirm these findings, although the majority of meningiomas with CDKN2A homodel had minimal positivity (64%), there were still a large proportion of tumors with clear p16 immunoreactivity (36%, **Fig 3f,g**). This suggests that loss of p16 may not be a reliable IHC marker of CDKN2A loss. We did see however, that all CDKN2A intact meningiomas that highly expressed CDKN2A mRNA had strong p16 positivity, and that the degree of p16 positivity may increase with WHO grade (when CDKN2A deleted meningiomas are excluded), similar to what we observed with CDKN2A mRNA levels (**Fig 3h,i**).

Lastly, as phosphorylation of Rb is a key downstream nidus of control for cell cycle progression in the CDKN2A pathway, we wanted to assess its phosphorylation status in meningiomas from each CDKN2A group. Rb protein was present in all meningiomas with CDKN2A deletion and were hyperphosphorylated at both key regulatory serine sites in all tumors (S780, S807/811, **Figure 3e**) leading to its inactivation. In CDKN2A^{low} meningiomas, Rb was present in all samples, but only hyperphosphorylated at both sites in 3/17 (17%) tumors. In CDKN2A^{high} meningiomas, 58% of samples (N=7/12) were Rb-deficient and in the remaining 5 Rb-intact samples, 3 (60%) had clear Rb hyperphosphorylation. This suggests that Rb-deficiency may be more common in CDKN2A^{high} meningiomas, and those that are Rb-intact, may behave like meningiomas with CDKN2A deletions due to Rb hyperphosphorylation.

RNAseq of primary (mng_50, mng_20, mng_84, mng_46) and established meningioma cell lines (IOMM-Lee, CH157) demonstrated increased CDKN2A expression in mng_46 and mng_84 cell lines and decreased RB1 expression (**Fig 3j**). pRB western blot confirmed that these cell lines were Rb-deficient (**Fig 3k**). All 4 primary meningioma cell lines clustered together with clinical meningioma samples from the DKFZ classifier (v11.4) and the Toronto cohort based on DNA methylation (**Fig 3l**). Cell viability assay demonstrated that the Rb-deficient cell lines were resistant to treatment with selective CDK4/6 inhibitors abemaciclib and palbociclib but not the meningioma cell lines with CDKN2A deletion (p16-deficient) (**Fig 3m**).

CONCLUSION: Although CDKN2A copy number loss has been established as a biomarker of aggressive biology in meningiomas, its rarity as an alteration limits its use for the majority (~95%) of meningiomas clinically. Using a large repository of multiomic data, we have demonstrated the following in meningiomas for the first time: 1) CDKN2A deletion confers poor outcome regardless of homodel, heterodel, or the associated degree of 9p deletion, 2) CDKN2A mRNA expression is independently predictive of outcome and is a reproducible biomarker of clinically aggressive meningiomas regardless of cohort and classification method, 3) meningiomas with CDKN2A deletion and high mRNA expression (CDKN2A^{high}) both have deregulated cell cycling, but while the former is associated with loss of the tumor suppressor action of p16, leading to evasion of the G1/S checkpoint, the latter may be associated with Rb deficiency or Rb-hyperphosphorylation leading to compensatory CDKN2A expression in a futile effort to halt cell cycle progression at the G2M checkpoint, 4) p16 IHC may not be a reliable marker of CDKN2A deletion but may be a better marker of CDKN2A mRNA expression level, and 5) CDKN2A^{high} meningiomas are associated with Rb deficiency and lack of response to CDK4/6 inhibitors, which have been a proposed therapeutic strategy for some clinically aggressive meningiomas.

FIGURES & FIGURE LEGENDS:

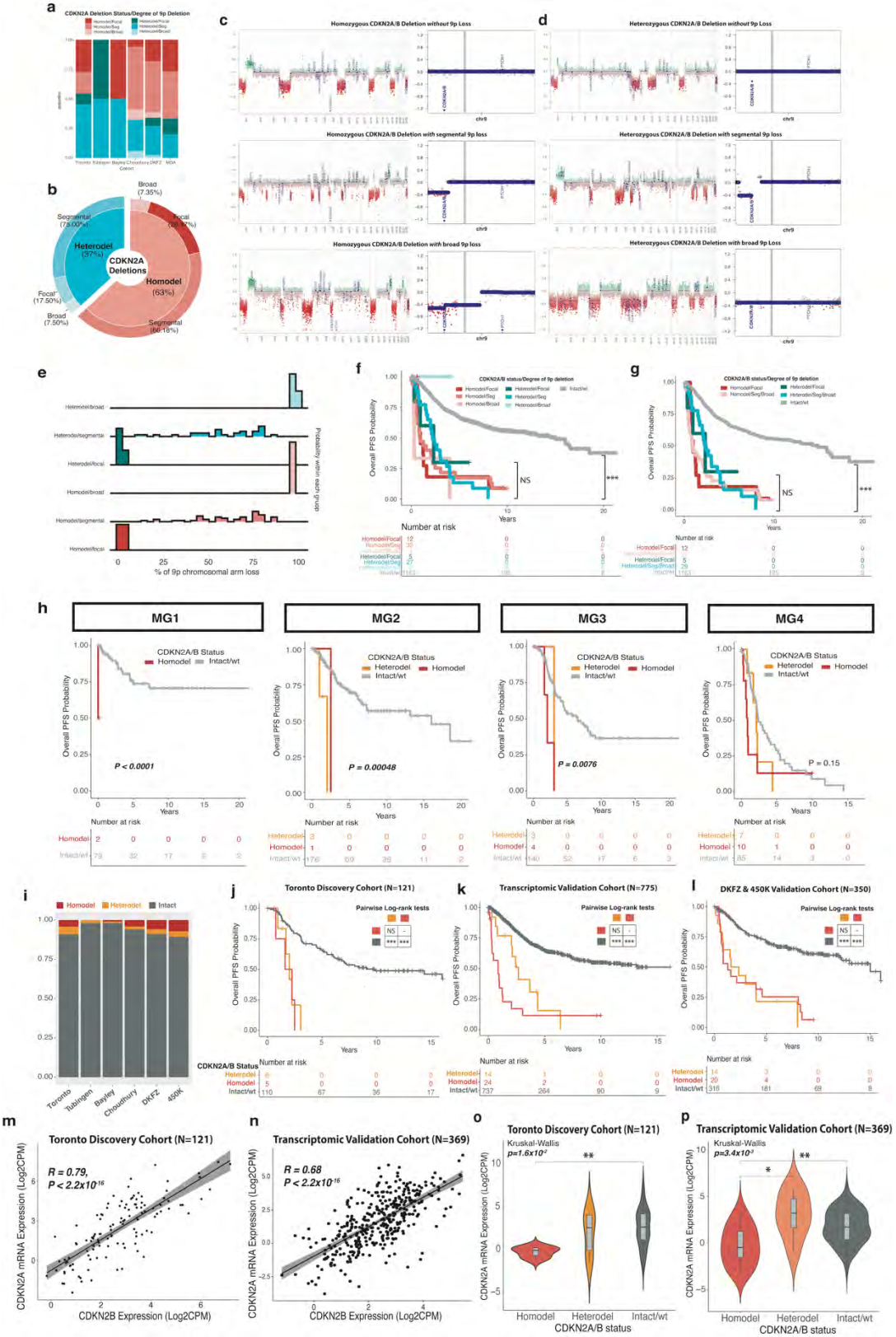

Figure 1. a, proportion of cases in each cohort with CDKN2A deletion stratified based on CDKN2A deletion type (homodel or heterodel) and by degree of associated 1p loss (focal,

segmental, or broad). **b,** proportional of cases in all cohorts combined stratified by CDKN2A deletion type (homodel or heterodel) and degree of associated 1p loss (focal, segmental, or broad). **c,** left, representative genome-wide copy number variation (CNV) plots of cases binned as CDKN2A/B homozygous deletion and the associated type of 9p loss, right, CNV plot of chromosome 9 from the same representative cases demonstrating the depth of CDKN2A/B loss relative to the rest of chr 9. **d,** left representative genome-wide CNV plots of cases binned as CDKN2A/B heterozygous deletion and the associated degree of 9p loss, right, chromosome 9 of the same representative cases. **e,** barplot demonstrating the associated degree of 9p loss (binned in segments of 5% of the chromosomal arm) in each CDKN2A deletion group. **f**, KM survival curve demonstrating PFS associated with CDKN2A deletions and their respective associated 9p loss. **g,** PFS associated with CDKN2A deletions when segmental and broad 9p deletions are grouped together vs focal CDKN2A deletions. **h,** PFS of meningiomas with CDKN2A homodel, heterodel, and intact/wt in each respective molecular group (MG). **i,** proportion of meningiomas in each cohort with CDKN2A homodel and heterodel. **j-l,** PFS of meningiomas in the Toronto discovery cohort, transcriptomic validation cohort, and DKFZ and 450k cohorts respectively stratified by CDKN2A homodel, heterodel, and intact/wt group. **m-n,** correlation plot of CDKN2A vs CDKN2B mRNA expression in the Toronto discovery cohort and transcriptomic validation cohort respectively. **o-p,** CDKN2A mRNA expression stratified by CDKN2A deletion group in the Toronto discovery cohort and transcriptomic validation cohort respectively.

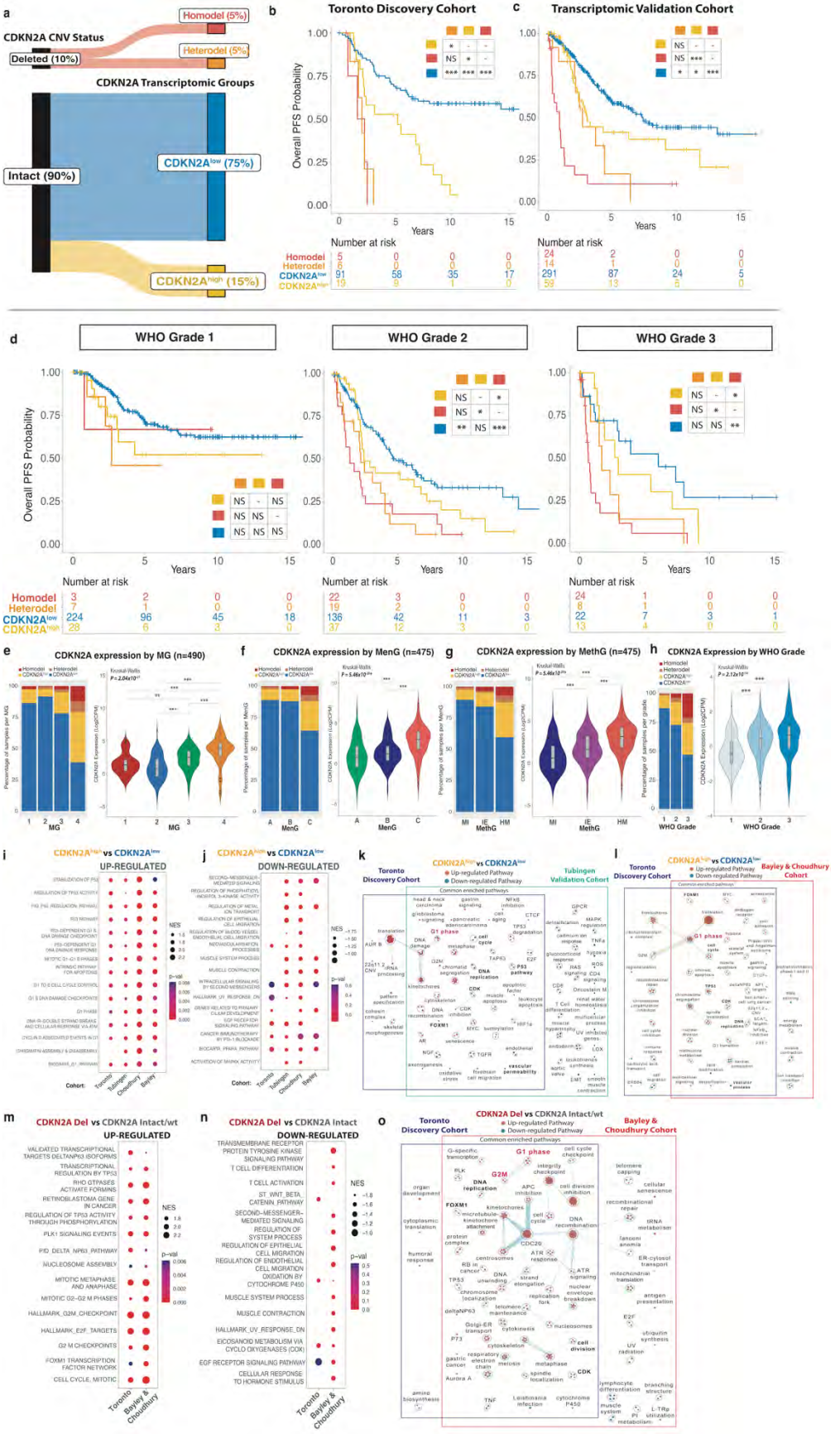
a
CDKN2A CNV Status
Homodel (5%)
Heterodel (5%)
Deleted (10%)
CDKN2A Transcriptomic Groups
Intact (90%)
CDKN2A^low (75%)
CDKN2A^high (15%)
b
Toronto Discovery Cohort
Overall PFS Probability
Years
Number at risk
Homodel 5 0 0 0
Heterodel 6 0 0 0
CDKN2A^low 91 58 35 17
CDKN2A^high 19 9 1 0
c
Transcriptomic Validation Cohort
Years
Number at risk
24 2 0 0
14 1 0 0
291 87 24 5
59 13 5 0
d
WHO Grade 1
WHO Grade 2
WHO Grade 3
Overall PFS Probability
Years
Number at risk
Homodel 3 2 0 0
Heterodel 1 0 0 0
CDKN2A^low 224 96 45 18
CDKN2A^high 28 6 3 0
22 3 0 0
19 2 0 0
136 42 11 3
37 12 3 0
24 1 0 0
8 1 0 0
22 7 3 1
13 4 0 0
e
CDKN2A expression by MG (n=490)
MG
f
CDKN2A expression by MenG (n=475)
MenG
g
CDKN2A expression by MethG (n=475)
MethG
h
CDKN2A Expression by WHO Grade
WHO Grade
i
CDKN2A^high vs CDKN2A^low
UP-REGULATED
Cohort: Toronto Tubingen Cloudhury Bayley
j
CDKN2A^high vs CDKN2A^low
DOWN-REGULATED
Cohort: Toronto Tubingen Cloudhury Bayley
k
CDKN2A^high vs CDKN2A^low
Up-regulated Pathway
Down-regulated Pathway
Toronto Discovery Cohort
Tubingen Validation Cohort
Common enriched pathways
l
CDKN2A^high vs CDKN2A^low
Up-regulated Pathway
Down-regulated Pathway
Toronto Discovery Cohort
Bayley & Choudhury Cohort
Common enriched pathways
m
CDKN2A Del vs CDKN2A Intact/wt
UP-REGULATED
Toronto
Bayley & Choudhury
n
CDKN2A Del vs CDKN2A Intact
DOWN-REGULATED
Toronto
Bayley & Choudhury
o
CDKN2A Del vs CDKN2A Intact/wt
Up-regulated Pathway
Down-regulated Pathway
Toronto Discovery Cohort
Bayley & Choudhury Cohort
Common enriched pathways

Figure 2. a, representative schematic of tumor assignment into different CDKN2A groups in the Toronto discovery cohort and the proportion of tumors in each group as a percentage of the entire cohort. **b, c,** Kaplan Meier (KM) survival plot denoting progression-free survival (PFS) probability of meningiomas in the Toronto discovery cohort and the combined validation cohort respectively based on CDKN2A copy number status and CDKN2A transcriptomic group (for meningiomas without any CDKN2A deletion). **d,** KM survival plot of meningiomas from all cohorts faceted by WHO grade. **e-g,** For each respective molecular classification indicated: left, stacked barplot showing the proportion of meningiomas belonging to each group coloured by CDKN2A status. Right, CDKN2A mRNA expression counts as a continuous variable in each group of tumors in each respective group. **h,** proportion of meningiomas belonging to each CDKN2A group and CDKN2A mRNA expression based on WHO grade in the combined cohort. **i,** Top 15 up-regulated pathways on GSEA of $CDKN2A^{high}$ vs $CDKN2A^{low}$ meningiomas that were significant (adj. $P < 0.05$) in at least 2 or more cohorts. **j,** Top 15-down regulated pathways on GSEA of $CDKN2A^{high}$ vs $CDKN2A^{low}$ meningiomas that were significant ($P < 0.01$) in at least 2 or more cohorts. **k,** Pathway enrichment analysis of significant pathways in $CDKN2A^{high}$ vs $CDKN2A^{low}$ meningiomas (adj. $P < 0.05$) in the Toronto vs. Tubingen cohorts. **l,** Pathway enrichment analysis of significant pathways in $CDKN2A^{high}$ vs $CDKN2A^{low}$ meningiomas (adj. $P < 0.05$) in the Toronto vs. combined Bayley and Choudhury cohorts. **m-n,** Top 15 significantly up- (adj. $P < 0.05$) and down-regulated pathways ($P < 0.01$) from GSEA in each respective cohort. **o,** Pathway enrichment analysis of common up- and down-regulated pathways (adj. $P < 0.05$) in the Toronto and the combined Bayley and Choudhury cohorts.

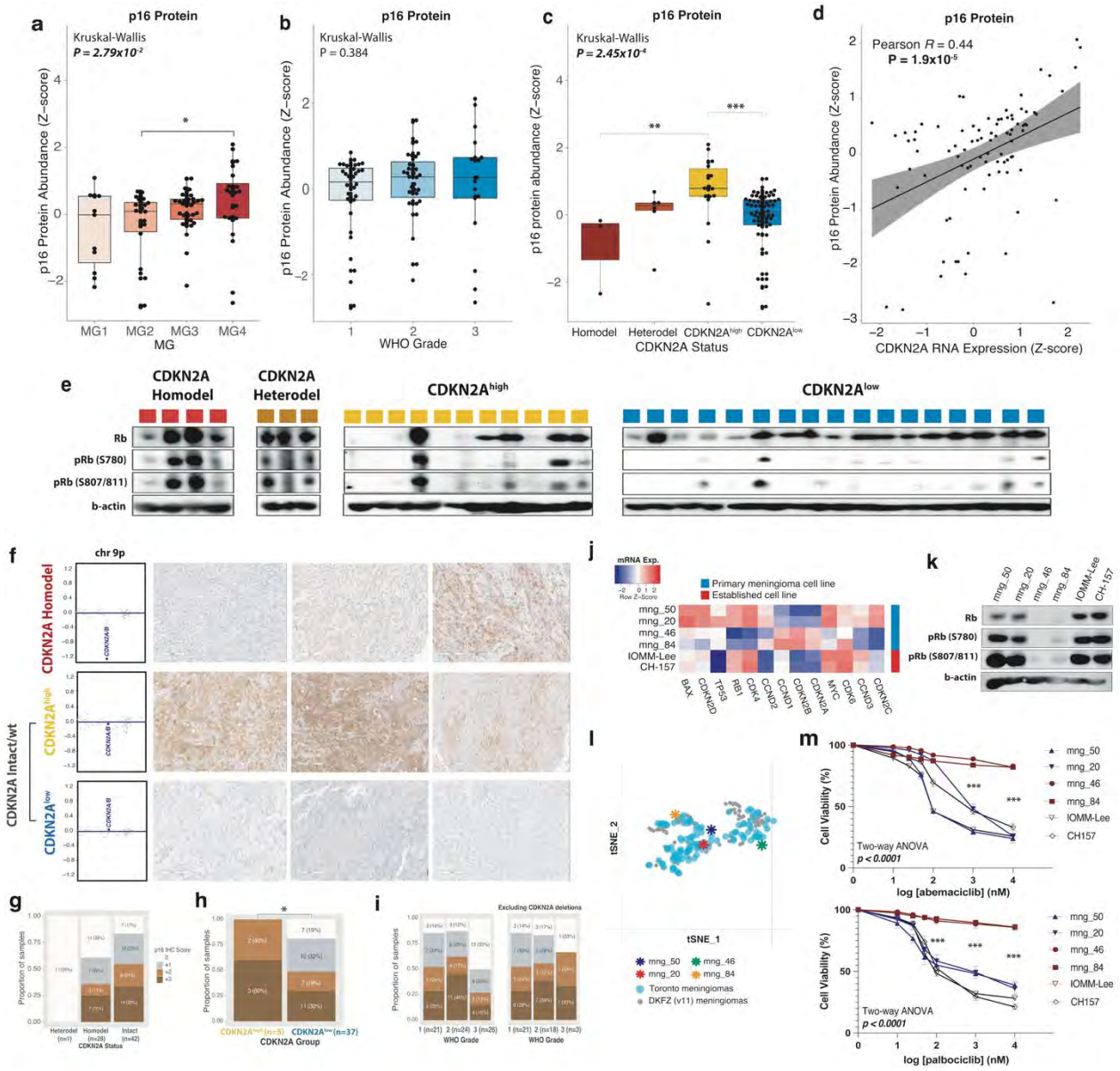

Figure 3. Protein data from the Toronto cohort. Boxplot of p16 protein abundance with **a,** molecular group (MG), **b,** WHO grade, **c,** CDKN2A status (homozygous deletion, heterozygous deletion, CDKN2A^{high}, CDKN2A^{low}). **d,** Correlation plot of p16 protein levels vs CDKN2A protein levels. **e,** Western blot of Rb phosphorylation at S780 and S807/811 in representative samples from each CDKN2A group. **f,** Representative p16 IHC images from meningiomas within each CDKN2A group. **g,** proportion of meningiomas with each degree of p16 positivity in CDKN2A deleted vs intact meningiomas. **h,** proportion of meningiomas with each degree of p16 positivity in CDKN2A^{high} vs CDKN2A^{low} meningiomas. **i,** proportion of meningiomas with p16 positivity in each WHO grade with and without the inclusions of CDKN2A deleted tumors. **j,** heatmap of mRNA expression of primary and established meningioma cell lines of cell cycling genes. **k,** pRB western blot in representative cell lines. **l,** panel from tSNE of DNA methylation of primary meningioma cell lines along with DKFZ classifier (v11.4) reference meningioma cases and Toronto clinical meningioma samples. **m,** cell viability assay at increasing doses of CDK4/6 inhibitors abemaciclib and palbociclib in primary and established meningioma cell lines. Adj. P from Kruskal Wallis test and post-hoc Dunn multiple comparisons test or two-sample test for

equality of proportions, and for cell viability data from two-way ANOVA and post-hoc Tukey's multiple comparisons test. *P<0.05; **P<0.01; ***P<0.001.

REFERENCES:

1. Ostrom QT, Cioffi G, Waite K, Kruchko C, Barnholtz-Sloan JS. CBTRUS Statistical Report: Primary Brain and Other Central Nervous System Tumors Diagnosed in the United States in 2014-2018. *Neuro Oncol.* 2021; 23(12 Suppl 2):iii1-iii105.

2. Driver J, Hoffman SE, Tavakol S, et al. A Molecularly Integrated Grade for Meningioma. *Neuro Oncol.* 2021.

3. Nassiri F, Liu J, Patil V, et al. A clinically applicable integrative molecular classification of meningiomas. *Nature.* 2021; 597(7874):119-125.

4. Bi WL, Mei Y, Agarwalla PK, Beroukhim R, Dunn IF. Genomic and Epigenomic Landscape in Meningioma. *Neurosurg Clin N Am.* 2016; 27(2):167-179.

5. Suppiah S, Nassiri F, Bi WL, et al. Molecular and translational advances in meningiomas. *Neuro Oncol.* 2019; 21(Suppl 1):i4-i17.

6. Nassiri F, Mamatjan Y, Suppiah S, et al. DNA methylation profiling to predict recurrence risk in meningioma: development and validation of a nomogram to optimize clinical management. *Neuro Oncol.* 2019; 21(7):901-910.

7. Boström J, Meyer-Puttlitz B, Wolter M, et al. Alterations of the tumor suppressor genes CDKN2A (p16(INK4a)), p14(ARF), CDKN2B (p15(INK4b)), and CDKN2C (p18(INK4c)) in atypical and anaplastic meningiomas. *Am J Pathol.* 2001; 159(2):661-669.

8. Guyot A, Duchesne M, Robert S, et al. Analysis of CDKN2A gene alterations in recurrent and non-recurrent meningioma. *J Neurooncol.* 2019; 145(3):449-459.

9. Perry A, Banerjee R, Lohse CM, Kleinschmidt-DeMasters BK, Scheithauer BW. A role for chromosome 9p21 deletions in the malignant progression of meningiomas and the prognosis of anaplastic meningiomas. *Brain Pathol.* 2002; 12(2):183-190.

10. Weber RG, Boström J, Wolter M, et al. Analysis of genomic alterations in benign, atypical, and anaplastic meningiomas: toward a genetic model of meningioma progression. *Proc Natl Acad Sci U S A.* 1997; 94(26):14719-14724.

11. Louis DN, Perry A, Wesseling P, et al. The 2021 WHO Classification of Tumors of the Central Nervous System: a summary. *Neuro Oncol.* 2021; 23(8):1231-1251.

12. Sievers P, Hielscher T, Schrimpf D, et al. CDKN2A/B homozygous deletion is associated with early recurrence in meningiomas. *Acta Neuropathol.* 2020; 140(3):409-413.

13. Choudhury A, Magill ST, Eaton CD, et al. Meningioma DNA methylation groups identify biological drivers and therapeutic vulnerabilities. *Nat Genet.* 2022; 54(5):649-659.

14. Bayley JCt, Hadley CC, Harmanci AO, Harmanci AS, Klisch TJ, Patel AJ. Multiple approaches converge on three biological subtypes of meningioma and extract new insights from published studies. *Sci Adv.* 2022; 8(5):eabm6247.

15. Hovestadt V, Zapatka M. Conumee: enhanced copy-number variation analysis using Illumina DNA methylation arrays. *R package version.* 2017; 1(0).

16. Kilaru V, Knight AK, Katrinli S, et al. Critical evaluation of copy number variant calling methods using DNA methylation. *Genet Epidemiol.* 2020; 44(2):148-158.

THE OBESITY PARADOX REVISITED: IS OBESITY STILL A PROTECTIVE FACTOR FOR PATIENTS WITH SEVERE COMORBIDITIES OR IN HIGH-RISK OPERATIONS?

Hyo Jin Son[1], Denise W. Gee[3], David Gomez[2], James Jung[2]
[1]Temerty Faculty of Medicine, University of Toronto, Toronto, Ontario
[2]Division of General Surgery, Department of Surgery, University of Toronto, Toronto, Ontario
[3]Division of General Surgery, Department of Surgery, Massachusetts General Hospital, Boston, Massachusetts

1. INTRODUCTION

With the rise in prevalence of obesity in Canada, there is a disproportionate burden of the obesity epidemic and its related medical comorbidities(1). As of 2018, approximately one in four Canadian adults (over 7 million people) are considered to have obesity. By 2031, the prevalence of obesity among Canadian adults is projected to hit more than 33% of the population(1). As the 5th leading cause of death worldwide, obesity is a major risk factor for multiple long-term comorbidities and lower life expectancy(2). However, studies have reported that in cases of acute stress, such as critical illness or surgery(3–7), patients with obesity appear to have better outcomes than normal-weight counterparts, a phenomenon known as the obesity paradox(8). Currently, it is unknown whether this paradox extends to patients with severe comorbidities and high-risk surgery. With a growing population of surgical patients with obesity, at risk of increased morbidity and mortality, a better understanding of this relationship is needed to meet the specific needs of this patient population.

2. METHODS

2.1 Study Design and Setting

We performed an observational study of adult patients who underwent surgery using the 2016-2019 American College of Surgeons National Surgical Quality Improvement Program (ACS-NSQIP) database to evaluate the relationship between Body Mass Index (BMI) and 30-day postoperative mortality. ACS-NSQIP is a nationally validated, risk-adjusted, outcome-based program that collects data from multiple hospital institutions about patient demographics, preoperative patient characteristics, and 30-day postoperative outcomes(9,10).

2.2 Study Cohort & Stratification

We analyzed the data from the NSQIP Participant Use Data Files, containing 4,126,058 adult patients who underwent major surgery between 2016 and 2019, in over 650 hospitals throughout the United States(11). After excluding patients for missing values for height and/or weight, demographic factors, and preoperative data, the remaining 3,085,582 patients were analyzed as our final study population.

We then constructed sub-cohorts stratified by patient comorbidity severity and procedural complexity. To assess patient comorbidity load, the NSQIP probability of 30-day mortality risk score and a modified Charlson comorbidity index (mCCI) was used. The NSQIP-derived mortality risk scores are calculated values that use preoperative characteristics to predict expected mortality rates for each patient based on risk models created from the entire NSQIP database(12,13). High comorbidity load was defined as patients with top 3% mortality probabilities.

Severity of comorbid disease was also calculated using the Charlson comorbidity index (CCI), modified (mCCI) to fit the available data and patient population(14). Previous studies have shown

that modified versions of the CCIs have been similar in efficiency and prognosis to the original CCI[15–17]. The comorbidities available in the NSQIP dataset used to determine the mCCI included (followed by corresponding point values): chronic obstructive pulmonary disease (COPD) (1), congestive heart failure (CHF) (1), diabetes mellitus (2), dialysis or end stage renal disease (2), ascites or end stage liver disease (3) and metastatic cancer (6). The point values were calculated and summed for a total mCCI score, according to the scoring system established by Charlson et al.[14]. Scores were then stratified into three groups: low, with mCCI scores of 0-2, moderate, with mCCI scores of 3-7 and high, with mCCI scores of ≥8.

In general, classification of high and low-risk surgery is not well defined as procedures can vary in terms of patient and operation-specific factors. Moreover, there is no comprehensive, universally validated list for high and low-risk surgical procedures. Therefore, for this study, high and low-risk surgery was classified by using Current Procedural Terminology (CPT) codes from previous studies that stratify procedure risk based on mortality[18,19] and blood transfusion risk[20]. Published guidelines and classification criteria including the Johns Hopkins Surgical Classification System[21] and the National Institute for Clinical Excellence (NICE) Specific Surgery Grades[22] were also used. Additionally, clinical judgment from three practicing surgeons, who independently examined the procedure-specific risk categorization, were used to stratify the procedures. Low risk procedures included certain laparoscopic cases, hernia repair and knee arthroscopy etc. High risk procedures included cases of abdominal aortic aneurysm repair, craniectomy and total colectomy etc.

2.3 Study Variables and Outcomes

The primary outcome of the study was 30-day postoperative mortality for patients undergoing major surgical procedures in both the inpatient and outpatient setting. BMI was calculated using the patient's weight, height, and the following non-metric conversion formula: BMI = [(weight in pounds / (height in inches)^2] x 703. BMI was further stratified into the World Health Organization (WHO) specific categories[23]: underweight (BMI <18.5 kg/m^2), normal (BMI 18.5-24.9 kg/m^2), overweight (BMI 25-29.9 kg/m^2), obesity class I (BMI 30-34.9 kg/m^2), class II (BMI 35-39.9 kg/m^2), and class III (BMI ≥ 40 kg/m^2).

The analyzed preoperative variables included patient demographics, comorbid conditions, and intraoperative variables. Three patient demographic factors including age as a continuous variable, sex (female or male) and race (Asian, White, African American, American Indian, Pacific Islander) were examined. Nineteen comorbid conditions were also analyzed including, functional status, sepsis or septic shock, history of diabetes mellitus, dyspnea, preoperative transfusions, American Society of Anesthesiology (ASA) class, smoking status, ventilator dependence, steroid use, preoperative weight loss of >10%, bleeding disorder, severe COPD, history of CHF, ascites, hypertension, currently requiring or on dialysis, disseminated cancer, and open wound infection. Lastly, three intra-operative variables including work relative value units, emergency case status, and operative time were examined.

2.4 Statistical Analysis

Continuous variables were summarized in terms of mean with standard deviation (SD) or median with interquartile range (IQR), whereas categorical variables were described in terms of frequency (%). We used χ^2 tests (categorical variables) or Kruskal-Wallis H tests (continuous variables) to test for significant differences among the BMI classes.

Multivariable logistic regression analysis was used to evaluate the relationship between BMI and 30-day postoperative mortality in the total study cohort and stratified subgroups. Risk adjustment for confounders considered significant on univariate analysis were included in the

regression models. The effects of BMI on mortality were calculated as odds ratios (OR) and corresponding 95% confidence intervals (CI) with normal BMI class as the reference.

Non-linear modeling for continuous BMI specification was done using fully adjusted restricted cubic spline models to characterize the dose-response relationship of BMI and mortality. Optimization of the number of knots was based on the Akaike information criteria (AIC), with ultimately 7 knots placed at equidistant percentiles[24] over the range of the BMI variable.

All analyses were performed using RStudio Version 2022.07.1+554. Statistical significance was indicated by $P < 0.05$.

3. RESULTS

Table 1 provides the baseline demographic and clinical characteristics of the total patient population included in the study. A total of 3,085,582 patients were included in our study, of whom 47.0% were patients with obesity (BMI ≥ 30 kg/m^2). The BMI distribution proportions were 1.4% (BMI <18.5 kg/m^2), 21.2% (BMI 18.5-24.9 kg/m^2), 30.4% (BMI 25-29.9 kg/m^2), 23.0% (BMI 30-34.9 kg/m^2), 12.8% (BMI 35-39.9 kg/m^2), 11.2% (BMI ≥ 40 kg/m^2). Most patients in this study were female (57.3%). Female patients showed a greater tendency to be underweight or obese. Patients with higher BMIs tended to be younger than patients with lower BMI. Majority of the patients in the study were Caucasians and compared to other racial groups, there was a higher prevalence of patients with obesity in the African American population.

In terms of comorbidities, diabetes and hypertension existed in significantly higher rates with increasing BMI, whereas, smoking, COPD, ascites and disseminated cancer were lower in patients with obesity. Mean operative time decreased with increasing BMI. The mean Work RVU of the total study population was 16.63 ± 8.74 units, which increased with higher BMI levels. Majority of the operations were elective cases (93.3%), and underweight patients were significantly more likely to undergo emergency cases (12.8%) compared to patients with obesity (5.8%).

Risk-adjusted multivariable logistic regression analysis was done to examine the relationship between BMI and 30-day postoperative. Figure 1 shows that in the total study population, there was a reverse J-shaped relationship between BMI and mortality, with highest and lowest odds in the underweight (OR 1.58 95%-CI 1.47-1.70) and obesity class II categories (OR 0.69 95%-CI 0.65-0.73), respectively, confirming the obesity paradox. Subgroup analysis was performed with the cohorts stratified by patient comorbidity severity and procedural complexity. Obesity status was no longer protective against mortality for patients who underwent high-risk procedures (BMI 30-34.9: OR 0.93 95%-CI 0.86-1.01; BMI 35-39.9: OR 0.92 95%-CI 0.83-1.03; BMI ≥ 40: OR 0.94 95%-CI 0.83-1.07), those with high comorbidity severity of mCCI ≥8 (BMI 30-34.9: OR 0.95 95%-CI 0.77-1.16; BMI 35-39.9: OR 0.78 95%-CI 0.60-1.02; BMI ≥ 40: OR 0.84 95%-CI 0.63-1.12) and with top 3% mortality probability (BMI 30-34.9: OR 0.96, 95%-CI 0.90-1.02; BMI ≥ 40: OR 0.94, 95%-CI 0.86-1.01).

4. CONCLUSION

The result of this study suggests that for the vast majority of adult patients undergoing major surgery, obesity status was associated with lower postoperative mortality. However, the obesity paradox did not hold true for patients with high comorbidity severity or those undergoing high-complexity cases. Associations between BMI and mortality varied by patient and procedure-specific factors suggesting that further analysis is needed to explore obesity as a determinant of health and evaluate risk factors that affect surgical outcomes in patients with obesity.

Table 1: Patient Characteristics of the Study Population

	Normal (Reference) (N=654176)	Underweight (N=41841)	Overweight (N=939025)	Obese I (N=710381)	Obese II (N=395958)	Obese III (N=344201)	Overall (N=3085582)	P-value
Age								
Mean (SD)	53.54 (16.95)	54.3 (17.6)	55.83 (15.36)	55.85 (14.39)	54.63 (14.02)	51.08 (13.97)	54.65 (15.3)	<0.001
Median [IQR]	57 [40, 68]	59 [41, 68]	59 [45, 68]	58 [46, 67]	56 [45, 66]	52 [41, 62]	57 [44, 67]	
SEX								
female	395514 (60.5%)	27930 (66.8%)	462544 (49.3%)	382452 (53.8%)	249041 (62.9%)	251349 (73.0%)	1768830 (57.3%)	<0.001
male	258662 (39.5%)	13911 (33.2%)	476481 (50.7%)	327929 (46.2%)	146917 (37.1%)	92852 (27.0%)	1316752 (42.7%)	
FNSTATUS2								
Independent	638767 (97.6%)	38801 (92.7%)	924742 (98.5%)	700243 (98.6%)	389836 (98.5%)	337496 (98.1%)	3029885 (98.2%)	<0.001
Partially Dependent	12108 (1.9%)	2164 (5.2%)	11864 (1.3%)	8699 (1.2%)	5322 (1.3%)	5897 (1.7%)	46054 (1.5%)	
Totally Dependent	3301 (0.5%)	876 (2.1%)	2419 (0.3%)	1439 (0.2%)	800 (0.2%)	808 (0.2%)	9643 (0.3%)	
PRSEPIS								
None	613454 (93.8%)	36967 (88.4%)	893489 (95.2%)	677055 (95.3%)	377327 (95.3%)	325798 (94.7%)	2924090 (94.8%)	<0.001
Sepsis	15393 (2.4%)	1868 (4.5%)	17469 (1.9%)	12739 (1.8%)	7185 (1.8%)	7096 (2.1%)	61750 (2.0%)	
Septic Shock	2698 (0.4%)	446 (1.1%)	2646 (0.3%)	1996 (0.3%)	1238 (0.3%)	1587 (0.5%)	10611 (0.3%)	
SIRS	22631 (3.5%)	2560 (6.1%)	25421 (2.7%)	18591 (2.6%)	10208 (2.6%)	9720 (2.8%)	89131 (2.9%)	
DIABETES								
NO	602849 (92.2%)	39077 (93.4%)	822300 (87.6%)	582940 (82.1%)	304754 (77.0%)	251415 (73.0%)	2603335 (84.4%)	<0.001
INSULIN	22422 (3.4%)	1640 (3.9%)	41993 (4.5%)	45513 (6.4%)	33204 (8.4%)	34857 (10.1%)	179629 (5.8%)	
NON-INSULIN	28905 (4.4%)	1124 (2.7%)	74732 (8.0%)	81928 (11.5%)	58000 (14.6%)	57929 (16.8%)	302618 (9.8%)	
DYSPNEA								
No	628479 (96.1%)	38430 (91.8%)	903337 (96.2%)	676516 (95.2%)	371167 (93.7%)	311634 (90.5%)	2929563 (94.9%)	<0.001
AT REST	2421 (0.4%)	476 (1.1%)	2562 (0.3%)	2258 (0.3%)	1532 (0.4%)	1946 (0.6%)	11195 (0.4%)	
MODERATE EXERTION	23276 (3.6%)	2935 (7.0%)	33126 (3.5%)	31607 (4.4%)	23259 (5.9%)	30621 (8.9%)	144824 (4.7%)	
TRANSFUS								
0	647978 (99.1%)	40744 (97.4%)	933536 (99.4%)	706633 (99.5%)	394053 (99.5%)	342306 (99.4%)	3065250 (99.3%)	<0.001
1	6198 (0.9%)	1097 (2.6%)	5489 (0.6%)	3748 (0.5%)	1905 (0.5%)	1895 (0.6%)	20332 (0.7%)	
WORKRVU								
Mean (SD)	16.47 (9.48)	18.09 (9.93)	16.45 (8.97)	16.62 (8.49)	16.81 (7.98)	17.06 (7.75)	16.63 (8.74)	<0.001
Median [IQR]	15 [9.45, 20.89]	17.4 [10.47, 22.83]	15.04 [9.75, 20.79]	15.37 [10.47, 20.72]	15.6 [10.47, 20.72]	16.84 [11.19, 20.72]	15.37 [10.17, 20.72]	
ASACLAS								
1-No Disturb	89659 (13.7%)	3089 (7.4%)	95617 (10.2%)	35694 (5.0%)	8137 (2.1%)	2613 (0.8%)	234809 (7.6%)	<0.001
2-Mild Disturb	322605 (49.3%)	14067 (33.6%)	493897 (52.6%)	367349 (51.7%)	174262 (44.0%)	79876 (23.2%)	1452056 (47.1%)	
3-Severe Disturb	207928 (31.8%)	19457 (46.5%)	311273 (33.1%)	278947 (39.3%)	197136 (49.8%)	240576 (69.9%)	1255317 (40.7%)	
4-Life Threat	32904 (5.0%)	5039 (12.0%)	37123 (4.0%)	27611 (3.9%)	15999 (4.0%)	20691 (6.0%)	139367 (4.5%)	
5-Moribund	1080 (0.2%)	189 (0.5%)	1115 (0.1%)	780 (0.1%)	424 (0.1%)	445 (0.1%)	4033 (0.1%)	
SMOKE								
No	506765 (77.5%)	26037 (62.2%)	775074 (82.5%)	596512 (84.0%)	336795 (85.1%)	296307 (86.1%)	2537490 (82.2%)	<0.001
Yes	147411 (22.5%)	15804 (37.8%)	163951 (17.5%)	113869 (16.0%)	59163 (14.9%)	47894 (13.9%)	548092 (17.8%)	
VENTILAT								
No	652136 (99.7%)	41503 (99.2%)	936953 (99.8%)	708772 (99.8%)	394979 (99.8%)	343095 (99.7%)	3077438 (99.7%)	<0.001
Yes	2040 (0.3%)	338 (0.8%)	2072 (0.2%)	1609 (0.2%)	979 (0.2%)	1106 (0.3%)	8144 (0.3%)	
HXCOPD								
No	624239 (95.4%)	36898 (88.2%)	905710 (96.5%)	683686 (96.2%)	379934 (96.0%)	329250 (95.7%)	2959717 (95.9%)	<0.001
Yes	29937 (4.6%)	4943 (11.8%)	33315 (3.5%)	26695 (3.8%)	16024 (4.0%)	14951 (4.3%)	125865 (4.1%)	
ASCITES								
No	651148 (99.5%)	41475 (99.1%)	936467 (99.7%)	708880 (99.8%)	395235 (99.8%)	343638 (99.8%)	3076843 (99.7%)	<0.001
Yes	3028 (0.5%)	366 (0.9%)	2558 (0.3%)	1501 (0.2%)	723 (0.2%)	563 (0.2%)	8739 (0.3%)	
HXCHF								
No	649911 (99.3%)	41397 (98.9%)	933556 (99.4%)	705730 (99.3%)	392939 (99.2%)	340630 (99.0%)	3064163 (99.3%)	<0.001
Yes	4265 (0.7%)	444 (1.1%)	5469 (0.6%)	4651 (0.7%)	3019 (0.8%)	3571 (1.0%)	21419 (0.7%)	
HYPERMED								
No	462160 (70.6%)	29524 (70.6%)	559876 (59.6%)	359892 (50.7%)	179056 (45.2%)	151032 (43.9%)	1741540 (56.4%)	<0.001
Yes	192016 (29.4%)	12317 (29.4%)	379149 (40.4%)	350489 (49.3%)	216902 (54.8%)	193169 (56.1%)	1344042 (43.6%)	
RENAFAIL								
No	651886 (99.7%)	41607 (99.4%)	936371 (99.7%)	708360 (99.7%)	394694 (99.7%)	342917 (99.6%)	3075835 (99.7%)	<0.001
Yes	2290 (0.4%)	234 (0.6%)	2654 (0.3%)	2021 (0.3%)	1264 (0.3%)	1284 (0.4%)	9747 (0.3%)	
DIALYSIS								
No	644009 (98.4%)	40827 (97.6%)	927730 (98.8%)	702100 (98.8%)	391172 (98.8%)	340183 (98.8%)	3046021 (98.7%)	<0.001
Yes	10167 (1.6%)	1014 (2.4%)	11295 (1.2%)	8281 (1.2%)	4786 (1.2%)	4018 (1.2%)	39561 (1.3%)	
DISCANCR								
No	632957 (96.8%)	39333 (94.0%)	917707 (97.7%)	697735 (98.2%)	390223 (98.6%)	340434 (98.9%)	3018389 (97.8%)	<0.001
Yes	21219 (3.2%)	2508 (6.0%)	21318 (2.3%)	12646 (1.8%)	5735 (1.4%)	3767 (1.1%)	67193 (2.2%)	
WNDINF								
No	635129 (97.1%)	38863 (92.9%)	918493 (97.8%)	695359 (97.9%)	387008 (97.7%)	334307 (97.1%)	3009159 (97.5%)	<0.001
Yes	19047 (2.9%)	2978 (7.1%)	20532 (2.2%)	15022 (2.1%)	8950 (2.3%)	9894 (2.9%)	76423 (2.5%)	
STEROID								
No	624627 (95.5%)	38544 (92.1%)	905626 (96.4%)	685922 (96.6%)	382556 (96.6%)	333438 (96.9%)	2970713 (96.3%)	<0.001
Yes	29549 (4.5%)	3297 (7.9%)	33399 (3.6%)	24459 (3.4%)	13402 (3.4%)	10763 (3.1%)	114869 (3.7%)	
WTLOSS								
No	638291 (97.6%)	36852 (88.1%)	930323 (99.1%)	706439 (99.4%)	394303 (99.6%)	343171 (99.7%)	3049379 (98.8%)	<0.001
Yes	15885 (2.4%)	4989 (11.9%)	8702 (0.9%)	3942 (0.6%)	1655 (0.4%)	1030 (0.3%)	36203 (1.2%)	
BLEEDDIS								
No	630232 (96.3%)	39306 (93.9%)	906395 (96.5%)	686016 (96.6%)	383013 (96.7%)	333398 (96.9%)	2978360 (96.5%)	<0.001
Yes	23944 (3.7%)	2535 (6.1%)	32630 (3.5%)	24365 (3.4%)	12945 (3.3%)	10803 (3.1%)	107222 (3.5%)	
EMERGNCY								
No	597085 (91.3%)	36504 (87.2%)	876083 (93.3%)	669033 (94.2%)	374955 (94.7%)	325465 (94.6%)	2879125 (93.3%)	<0.001
Yes	57091 (8.7%)	5337 (12.8%)	62942 (6.7%)	41348 (5.8%)	21003 (5.3%)	18736 (5.4%)	206457 (6.7%)	
OPTIME								
Mean (SD)	113.27 (96.57)	119.25 (104.97)	113.8 (93.92)	115.17 (92.97)	114.7 (90.45)	112.14 (84.22)	114.01 (92.97)	<0.001
Median [IQR]	85 [49, 145]	88 [50, 153]	87 [52, 145]	90 [54, 146]	91 [56, 144]	91 [57, 142]	88 [53, 145]	
RACE_NEW								
White	536791 (82.1%)	32895 (78.6%)	791021 (84.2%)	595227 (83.8%)	325735 (82.3%)	273113 (79.3%)	2554782 (82.8%)	<0.001
American Indian or Alaska Native	3368 (0.5%)	265 (0.6%)	5265 (0.6%)	4711 (0.7%)	2970 (0.8%)	2582 (0.8%)	19161 (0.6%)	
Asian	46321 (7.1%)	3039 (7.3%)	37647 (4.0%)	15133 (2.1%)	4974 (1.3%)	2659 (0.8%)	109773 (3.6%)	
Black or African American	65252 (10.0%)	5539 (13.2%)	101264 (10.8%)	91999 (13.0%)	60242 (15.2%)	63779 (18.5%)	388075 (12.6%)	
Native Hawaiian or Pacific Islander	2444 (0.4%)	103 (0.2%)	3828 (0.4%)	3311 (0.5%)	2037 (0.5%)	2068 (0.6%)	13791 (0.4%)	

Table 2: Adjusted Odds Ratios for Mortality in the Total Study Population and Sub-Cohorts Stratified by Patient Comorbidity Severity and Procedural Complexity

	BMI < 18.5	**BMI 18.5-24.9**	**BMI 25-29.9**	**BMI 30-34.9**	**BMI 35-39.9**	**BMI ≥ 40**
Total Study Population	1.58*	(Ref = 1)	0.78*	0.73*	0.69*	0.75*
High Risk Procedures	1.44*	(Ref = 1)	0.84*	0.93	0.92	0.94
Top 3% Mortality Probability	1.17*	(Ref = 1)	0.96	0.96	0.89*	0.94
mCCI ≥8	1.50*	(Ref = 1)	0.97	0.95	0.78	0.84

*P < 0.05

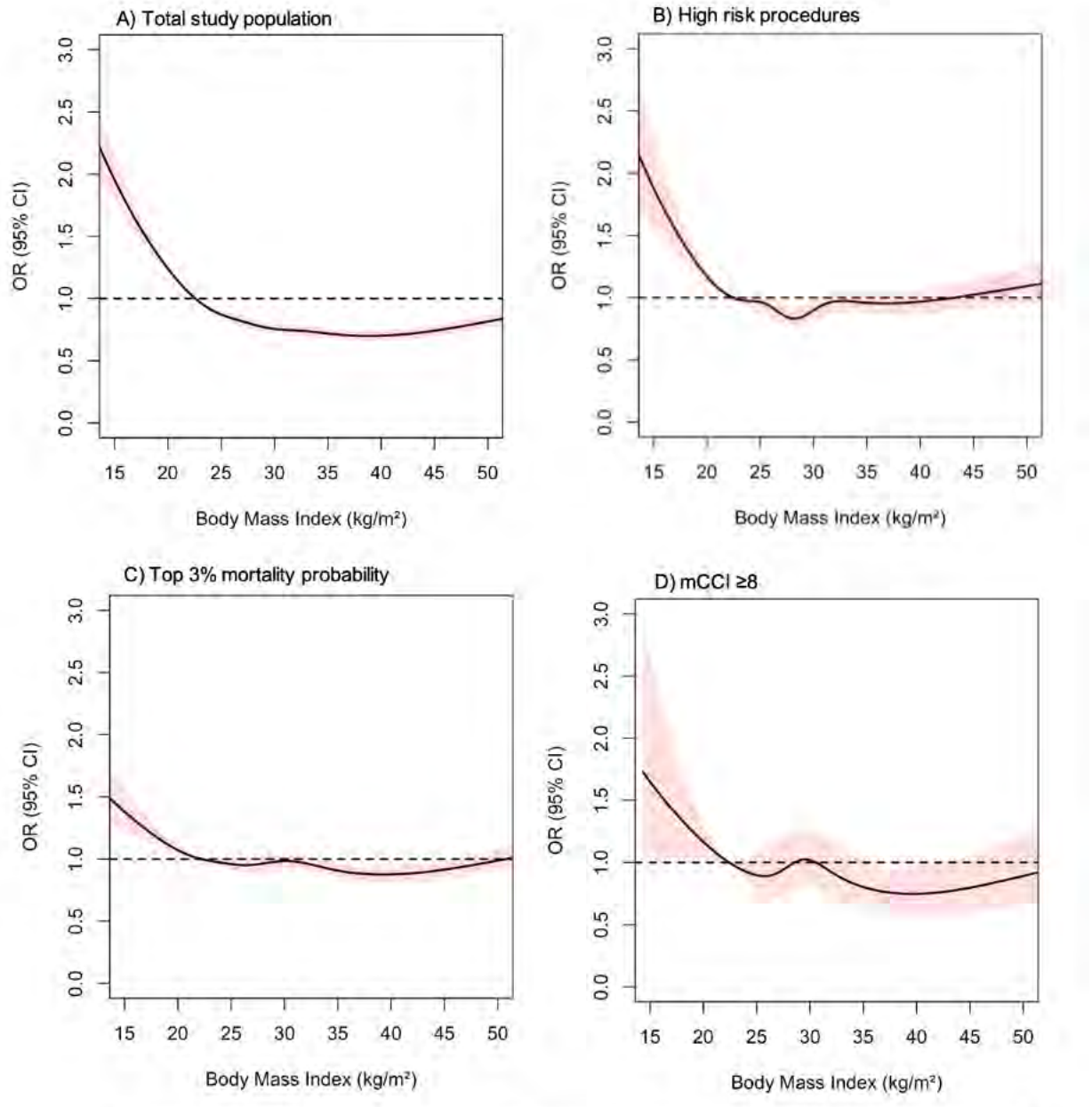

Figure 1. Distribution of odds ratios of 30-day postoperative mortality across patient BMI (reference BMI of 22kg/m^2) using restricted cubic spline curves for a) all patients, b) patients with high-risk procedures, c) patients with top 3% mortality probability, and d) patients with mCCI ≥8

REFERENCES

1. Bancej C, Jayabalasingham B, Wall RW, Rao DP, Do MT, de Groh M, et al. Evidence Brief – Trends and projections of obesity among Canadians. Health Promot Chronic Dis Prev Can. 2015 Sep;35(7):109–12.

2. Ng M, Fleming T, Robinson M, Thomson B, Graetz N, Margono C, et al. Global, regional, and national prevalence of overweight and obesity in children and adults during 1980–2013: a systematic analysis for the Global Burden of Disease Study 2013. The Lancet. 2014 Aug 30;384(9945):766–81.

3. Mullen JT, Moorman DW, Davenport DL. The Obesity Paradox: Body Mass Index and Outcomes in Patients Undergoing Nonbariatric General Surgery. Ann Surg. 2009 Jul;250(1):166–72.

4. Tsai S, Choti MA, Assumpcao L, Cameron JL, Gleisner AL, Herman JM, et al. Impact of Obesity on Perioperative Outcomes and Survival Following Pancreaticoduodenectomy for Pancreatic Cancer: A Large Single-Institution Study. J Gastrointest Surg. 2010 Jul 1;14(7):1143–50.

5. Fonarow GC, Srikanthan P, Costanzo MR, Cintron GB, Lopatin M. An obesity paradox in acute heart failure: Analysis of body mass index and inhospital mortality for 108927 patients in the Acute Decompensated Heart Failure National Registry. Am Heart J. 2007 Jan 1;153(1):74–81.

6. Tremblay A, Bandi V. Impact of Body Mass Index on Outcomes Following Critical Care. Chest. 2003 Apr;123(4):1202–7.

7. Hidvegi R, Puelacher C, Gualandro DM, Lampart A, Lurati Buse G, Hammerer-Lerchner A, et al. Obesity paradox and perioperative myocardial infarction/injury in non-cardiac surgery. Clin Res Cardiol. 2020 Sep;109(9):1140–7.

8. Gruberg L, Weissman NJ, Waksman R, Fuchs S, Deible R, Pinnow EE, et al. The impact of obesity on the short-term andlong-term outcomes after percutaneous coronary intervention: the obesity paradox? J Am Coll Cardiol. 2002 Feb;39(4):578–84.

9. Khuri SF, Daley J, Henderson W, Hur K, Demakis J, Aust JB, et al. The Department of Veterans Affairs' NSQIP: the first national, validated, outcome-based, risk-adjusted, and peer-controlled program for the measurement and enhancement of the quality of surgical care. National VA Surgical Quality Improvement Program. Ann Surg. 1998 Oct;228(4):491–507.

10. Bilimoria KY, Liu Y, Paruch JL, Zhou L, Kmiecik TE, Ko CY, et al. Development and evaluation of the universal ACS NSQIP surgical risk calculator: a decision aid and informed consent tool for patients and surgeons. J Am Coll Surg. 2013 Nov;217(5):833-842.e1-3.

11. ACS NSQIP Participant Use Data File [Internet]. ACS. [cited 2023 Mar 4]. Available from: https://www.facs.org/quality-programs/data-and-registries/acs-nsqip/participant-use-data-file/

12. Cohen ME, Liu Y, Ko CY, Hall BL. An Examination of American College of Surgeons NSQIP Surgical Risk Calculator Accuracy. J Am Coll Surg. 2017 May;224(5):787-795.e1.

13. Bilimoria KY, Liu Y, Paruch JL, Zhou L, Kmiecik TE, Ko CY, et al. Development and Evaluation of the Universal ACS NSQIP Surgical Risk Calculator: A Decision Aide and Informed Consent Tool for Patients and Surgeons. J Am Coll Surg. 2013 Nov;217(5):833-842.e3.

14. Charlson ME, Pompei P, Ales KL, MacKenzie CR. A new method of classifying prognostic comorbidity in longitudinal studies: development and validation. J Chronic Dis. 1987;40(5):373–83.

15. Sundararajan V, Henderson T, Perry C, Muggivan A, Quan H, Ghali WA. New ICD-10 version of the Charlson comorbidity index predicted in-hospital mortality. J Clin Epidemiol. 2004 Dec 1;57(12):1288–94.

16. Ehlert BA, Nelson JT, Goettler CE, Parker FM, Bogey WM, Powell CS, et al. Examining the myth of the “July Phenomenon” in surgical patients. Surgery. 2011 Aug 1;150(2):332–8.

17. D’Hoore W, Bouckaert A, Tilquin C. Practical considerations on the use of the charlson comorbidity index with administrative data bases. J Clin Epidemiol. 1996 Dec 1;49(12):1429–33.

18. Glance LG, Lustik SJ, Hannan EL, Osler TM, Mukamel DB, Qian F, et al. The Surgical Mortality Probability Model: derivation and validation of a simple risk prediction rule for noncardiac surgery. Ann Surg. 2012 Apr;255(4):696–702.

19. Schwarze ML, Barnato AE, Rathouz PJ, Zhao Q, Neuman HB, Winslow ER, et al. Development of a list of high-risk operations for patients 65 years and older. JAMA Surg. 2015 Apr;150(4):325–31.

20. Montroy J, Lavallée LT, Zarychanski R, Fergusson D, Houston B, Cagiannos I, et al. The Top 20 Surgical Procedures Associated with the Highest Risk for Blood Transfusion. BJS Br J Surg. 2020;107(13):e642–3.

21. Donati A, Ruzzi M, Adrario E, Pelaia P, Coluzzi F, Gabbanelli V, et al. A new and feasible model for predicting operative risk. Br J Anaesth. 2004 Oct 1;93:393–9.

22. Overview | Routine preoperative tests for elective surgery | Guidance | NICE [Internet]. NICE; 2016 [cited 2023 Mar 4]. Available from: https://www.nice.org.uk/guidance/ng45

23. Classification of Overweight and Obesity by BMI, Waist Circumference, and Associated Disease Risks. [Internet]. [cited 2023 Mar 4]. Available from: https://www.nhlbi.nih.gov/health/educational/lose_wt/BMI/bmi_dis

24. Harrell FE. Regression Modeling Strategies. 2020;

Translational Research

THE IMPACT OF MAGNETIC RESONANCE GUIDED HIGH INTENSITY FOCUSED ULTRASOUND GENERATED HYPERTHERMIA AND CHEMOTHERAPY ON THE IMMUNE PROFILE OF A MURINE MODEL OF RHABDOMYOSARCOMA

Julia Nomikos[1,2], Claire Wunker[1,2,3], Adam C. Waspe[4], Yael Babichev[2], Karolina Piorkowska[4], Suzanne Wong[4], Warren Foltz[5], J. Ted Gerstle[6], Elizabeth G. Demicco[7], Abha A. Gupta[4,5,7], Cynthia J. Guidos[8], James M. Drake[9], and Rebecca Gladdy[1,2,10]

[1]Institute of Medical Science, University of Toronto, Toronto, CA
[2]Lunenfeld-Tanenbaum Research Institute, Mount Sinai Hospital, Toronto, CA
[3] Saint Louis University, St. Louis, Missouri, USA
[4]Hospital for Sick Children, Toronto, CA
[5]Princess Margaret Hospital, University Health Network, Toronto, CA
[6]Memorial Sloan Kettering Cancer Centre, New York, USA
[7]Mount Sinai Hospital, Toronto, CA
[8]Department of Developmental & Stem Cell Biology, Hospital for Sick Children, Toronto, CA
[9]Division of Neurosurgery, Hospital for Sick Children, Toronto, CA
[10]Department of Surgery, University of Toronto, Toronto, CA

Introduction

Rhabdomyosarcoma (RMS) is the most common pediatric soft tissue sarcoma (STS)[1]. The most common subtype of pediatric RMS is embryonal RMS (ERMS)[2,3]. RMS treatment includes chemotherapy, radiation, and/or surgical resection. The current chemotherapeutic standard of care in North America is a combination of vincristine, actinomycin D, and cyclophosphamide[4]. In patients with recurrent or metastatic disease, the 5-year survival rate following aggressive treatment remains poor and variable at about 30%[5]. In these cases of recurrent or advanced RMS, alternate lines of chemotherapy include doxorubicin which, although effective, is associated with dose-limiting cardiotoxicity[4]. This demonstrates a need for novel therapies that are more efficacious and cause less systemic toxicity.

Immunotherapy has proven to be an effective treatment strategy in many types of solid tumours such as melanoma, but success in STS does not seem to be as robust[6]. The characterization of STS through immune profiling can be challenging due the heterogeneity of this disease. This data varies widely between the different types of STS[7]. Immune profiling data specific to RMS is sparse because it is often grouped in an "other" subtype category. Thus, this research seeks to better understand the immune profile of RMS, in particular following treatment with hyperthermia (HT) in combination with thermosensitive liposomal doxorubicin (TLD).

TLD consists of doxorubicin encapsulated in a thermosensitive liposome. The doxorubicin is released from the liposome at an elevated temperature of approximately 40°C[8]. To heat the drug *in vivo*, magnetic resonance-guided high intensity focused ultrasound (MRgHIFU) combines MRI and ultrasound to produce targeted and controlled HT[9,10]. The Gladdy lab has previously shown that tumour targeted HT in combination with TLD resulted in improved survival in an immunocompetent ERMS mouse model[8]. The HT+TLD treatment group also had the slowest tumour growth and had significantly lower levels of doxorubicin in the heart and liver compared to the free doxorubicin treatment group, which could suggest reduced toxicity[11].

Furthermore, HT can modulate the immune response through the increased release of immune stimulatory agents such as heat shock proteins and immunogenic targets from tumor cells[12-16]. Recent data suggests that the efficacy of immune checkpoint inhibitors (ICIs) can also be enhanced by tumour-localized HT therapy[17]. Therefore, if the HT from this already promising HT+TLD treatment is stimulating the immune system, immunotherapy in combination with HT+TLD treatment may be an even more effective treatment option.

Objectives and Hypothesis

The purpose of this project is to characterize the immune profile of a murine model of ERMS by investigating the quantity and location of immune cells within tumours, to determine what effect chemotherapy and HT have on immune infiltrates, and to analyze the immune response over time. We expect to see an increased immune response in HT treatment groups as HT has been shown to modulate the immune response[12]. Furthermore, we expect to see fewer B cells, and a higher macrophage population consistent with a previous study[18].

Methods

A syngeneic, immunocompetent ERMS mouse model previously developed by the Gladdy lab was employed[19]. p53 heterozygous mice were intramuscularly injected with ~10^4 p53 null, $FGFR4^{V550E}$ mutant murine myoblast cells into the right hind limb at 4-8 weeks of age. Mice were divided into 2 groups: HT vs. normothermia (NT). The HT group underwent localized heating of tumours via MRgHIFU at 40°C for 20 minutes, while the NT group received no heat treatment. Intravenous chemotherapy of either free doxorubicin (FD), vincristine (VINC) or TLD was administered 1.5 minutes into MRgHIFU treatment for the HT group, and at the desired time of treatment for the NT group. This resulted in 8 experimental groups: control (untreated), FD, VINC, TLD, HT, HT+FD, HT+VINC, and HT+TLD. Tumours were collected via necropsy at 24 and 168 hours (h) post-treatment and immunohistochemistry was performed on tumour sections

with antibodies against CD11b (macrophages, monocytes, natural killer cells, granulocytes), CD3 (T lymphocytes), and B220 (B lymphocytes). Positively stained cells in whole tumour sections were quantified using HALO image analysis software and sample tumour sections were manually counted and verified by sarcoma pathologist Dr. Elizabeth Demicco. Hyperion Imaging Mass Cytometry (IMC) was performed at the Centre for Advanced Single Cell Analysis at the Hospital for Sick Children under the supervision of Dr. Cynthia Guidos on a subset of OCT embedded tumour cross sections for two 1mm^2 regions of interest in each tumour sample. This panel of markers consisted of CD45, gp38, MHC2, aSMA, CD11b, CD22, CD8a, CD11c, FOXP3, Sirpa, CD3, CD31, Ly6G, CD64, CD4, B220, and DNA.

Results

There were distinct differences in the quantity of CD11b, CD3, and B220 positive cells in tumours. CD11b positive cells were the most abundant (0-50% of tissue area), followed by CD3 positive cells (0-5000/mm^2), and very few B220 cells (0-140/mm^2) (Figure 1). This indicates that the most prevalent immune cells in the tumours are macrophages/monocytes/natural killer cells/granulocytes, while B cells are sparse.

There was significantly more CD11b positive staining in the HT+TLD group compared to the TLD group at 24 hours post-treatment ($p= 0.0025$, Figure 1). Furthermore, there were more B220 positive cells in the HT treated tumours at 168 hours post-treatment when compared to the untreated tumours ($p=0.0125$, Figure 1). However, it should be noted that not all of the HT treated tumours had significantly different immune cell counts when compared to their respective control. Moreover, at 24 hours post treatment, the HT+FD treated tumours had significantly fewer CD3 positive cells when compared to the FD treated group alone. However, this is likely due to the small sample size of n=4 and the large variability observed in the FD group.

When observing immune cell counts irrespective of drug treatment, there was a significantly higher number of B220 positive cells in HT treated tumours when compared to NT tumours at 168 hours post treatment (Figure 2).

Comparison of tumour peripheral and central CD11b, CD3, and B220 staining revealed there were significantly more positively stained cells in the tumour periphery compared to the centre across all three markers (data not shown). The tumour periphery was defined as 1mm from the edge of tumours, and the centre was defined as any part of the tumour further than 1mm from the edge.

IMC was conducted on 4 samples for preliminary analysis: one untreated tumour, one HT 24h tumour, and one HT 168h tumour, and one spleen as a positive control. The most abundant markers expressed across all samples (excluding DNA) were aSMA, MHC2, gp38, Sirpa, CD11b, and CD64 (Figure 3A). The least abundant markers from the IMC panel were FOXP3, CD8a, B220, CD22, and Ly6G (Figure 3A).

When examining treatment specific differences in markers between IMC images, there seemed to be a higher number of CD64 positive cells in the tumour periphery in the HT 24 hour post-treatment tumour compared to untreated or HT 168h (Figure 3B). However, it should be noted that these results have not yet been quantified to confirm significance.

Discussion

B cell tumour expression has been correlated with significantly increased overall survival in soft tissue sarcoma[20]. The fact that this mouse model of ERMS is exhibiting low levels of B cells could suggest that this could contribute to the immunologically cold nature of these tumours. Tumour associated macrophages (TAMs) usually make up the majority of the immune infiltrate, and often increase tumour pathogenesis, blood vessel development, immune suppression, and metastasis[21]. Though CD11b is not a marker of the macrophage population alone, the high number in comparison to CD3 and B220 is consistent with the literature in sarcoma[21].

To more accurately characterize the subpopulations of immune cells within tumours and gain a more complete picture of the tumour microenvironment (TME), we employed IMC. There were high levels of myofibroblasts/perycites (aSMA) and fibroblasts/mesenchymal cells (gp38). This is expected in RMS, which generally originates from skeletal muscle. The combination of high MHC2, Sirpa, CD11b, and CD64 suggests a macrophage dominated TME, consistent with the literature[21]. Additionally, binding of CD47 on tumour cells to Sirpa on macrophages and dendritic cells incites a "don't eat me signal", allowing for tumour evasion, which could contribute to the immunologically cold nature of these tumours[7]. The combination of low FOXP3, CD8a, B220, CD22, and Ly6G indicated that there were few B cells and granulocytes in the TME, and that the majority of T cells present were CD4 helper T cells (due to low levels of cytotoxic and regulatory T cells).

Increased CD11b positive staining in the HT+TLD group compared to the TLD group at 24h post-treatment, increased B cells in the HT treated tumours at 168h post-treatment when compared to the untreated tumours, and a general increase in B cells in all HT treated tumours compared to NT tumours at 168h post treatment supports the hypothesis that HT could be increasing immune infiltrate through the release of heat shock proteins and immunogenic targets from cancer cells[12-16]. This antigen presentation modulates the immune response in a number of different ways, such as increased antigen presentation to T lymphocytes and increased natural killer (NK) cell activity at temperatures around 40 degrees Celsius (but below 42 degrees Celsius)[12-16]. Moreover, CD64 is a marker of macrophages and monocytes, and preliminary IMC results also indicate that CD64 positive cells are being recruited to the tumour periphery at 24h following HT treatment. However, it should be noted that the IMC images have not been quantified and each group currently only has a sample size of n=1. For this reason, these results are only speculation for the time being. The time periods associated with these results also align with the faster acting innate immune system (example: macrophages), for which significance was observed at 24h post treatment, and the adaptive immune system (B and T cells) which can take up to a week to mount a full response, with significance observed at 168h post treatment. However, not all HT groups had significantly different immune cell counts when compared to their respective NT control, suggesting that treatment with different chemotherapies can affect HT induced immune stimulation.

Significance and Future Directions

By characterizing the immune infiltrate in the tumours of an immunocompetent mouse model of ERMS, we will be able to understand the location and presence of immune cell populations in tumours over time to identify future immunotherapeutic targets. We conclude that the relative density of CD11b and B220 positive cells was similar to that of macrophages and B cells in human RMS indicating that this murine model is capable of modeling the human immune response. We will expand our mouse cohort for further characterization of immune infiltrate in this murine ERMS model with a goal of n=10 in each treatment group. Current results indicate potential for HT mediated immune stimulation at certain time points, but further data is needed to increase study power.

This research will allow us to understand whether we can harness HT-related immune stimulation from an already promising therapy (HT + TLD) to create an even greater synergistic effect with immune checkpoint inhibitors (ICIs) while maintaining reduced toxicity. Ultimately, the use of this data to inform the selection of an optimal time point and ICI to be administered in potential combination with HT+ drug will allow clinicians to develop a protocol that could be translated into a Phase 2 trial for pediatric patients with this devastating cancer.

Figures

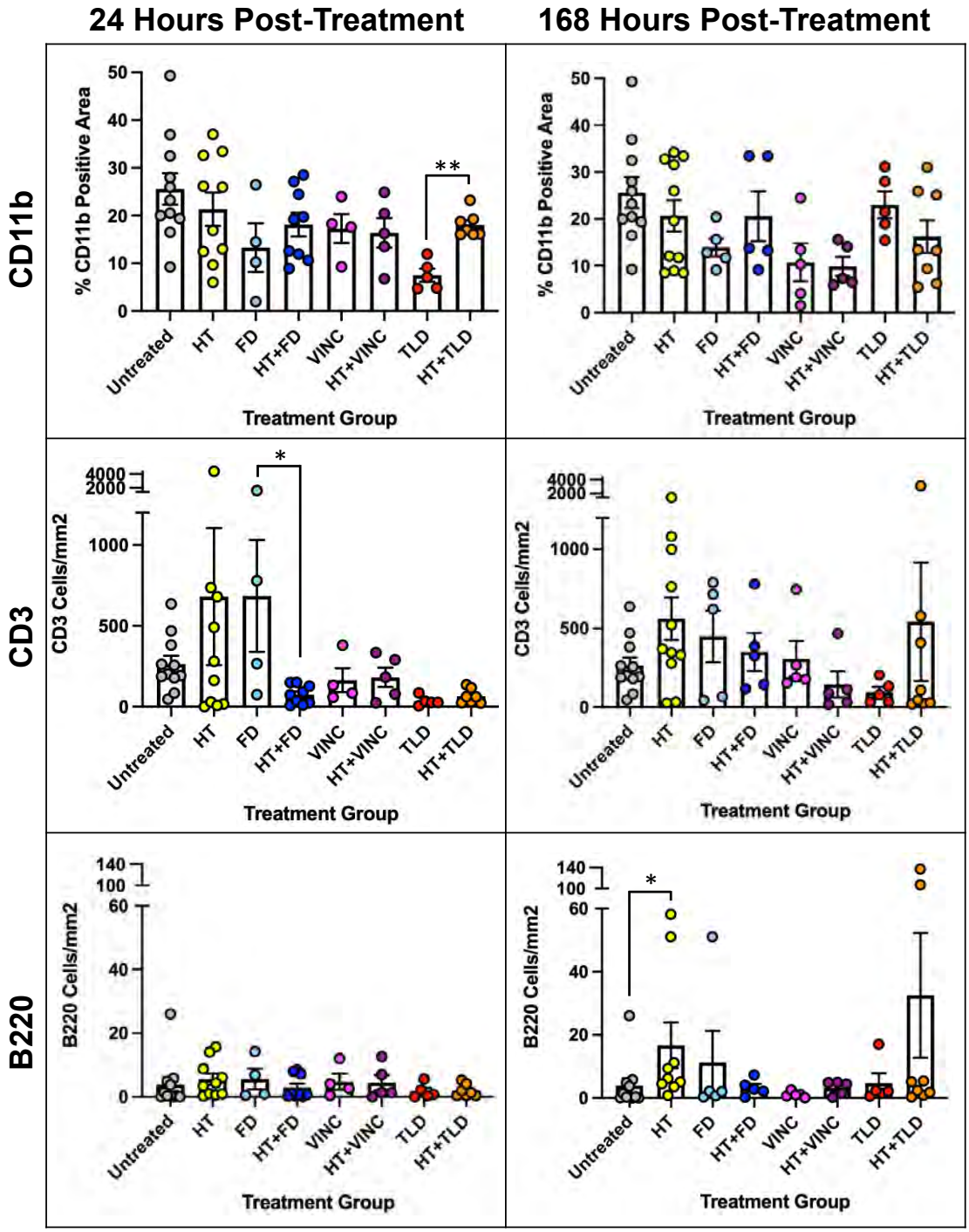

Figure 1. Quantification of CD11b, CD3, and B220 staining of whole cross sections of treated tumors (HT-hyperthermia, FD- doxorubicin, VINC-vincristine, TLD-temperature-sensitive liposomal doxorubicin). Scale bars vary between graphs. Total n=99. Error bars: mean ± SEM. * indicates significance with a p value < 0.05, ** indicates significance with a p value < 0.01. CD11b 24h TLD/HT+TLD: p=0.0025. CD3 24h FD/HT+FD: p=0.0336. B220 168h untreated/HT: p=0.0125.

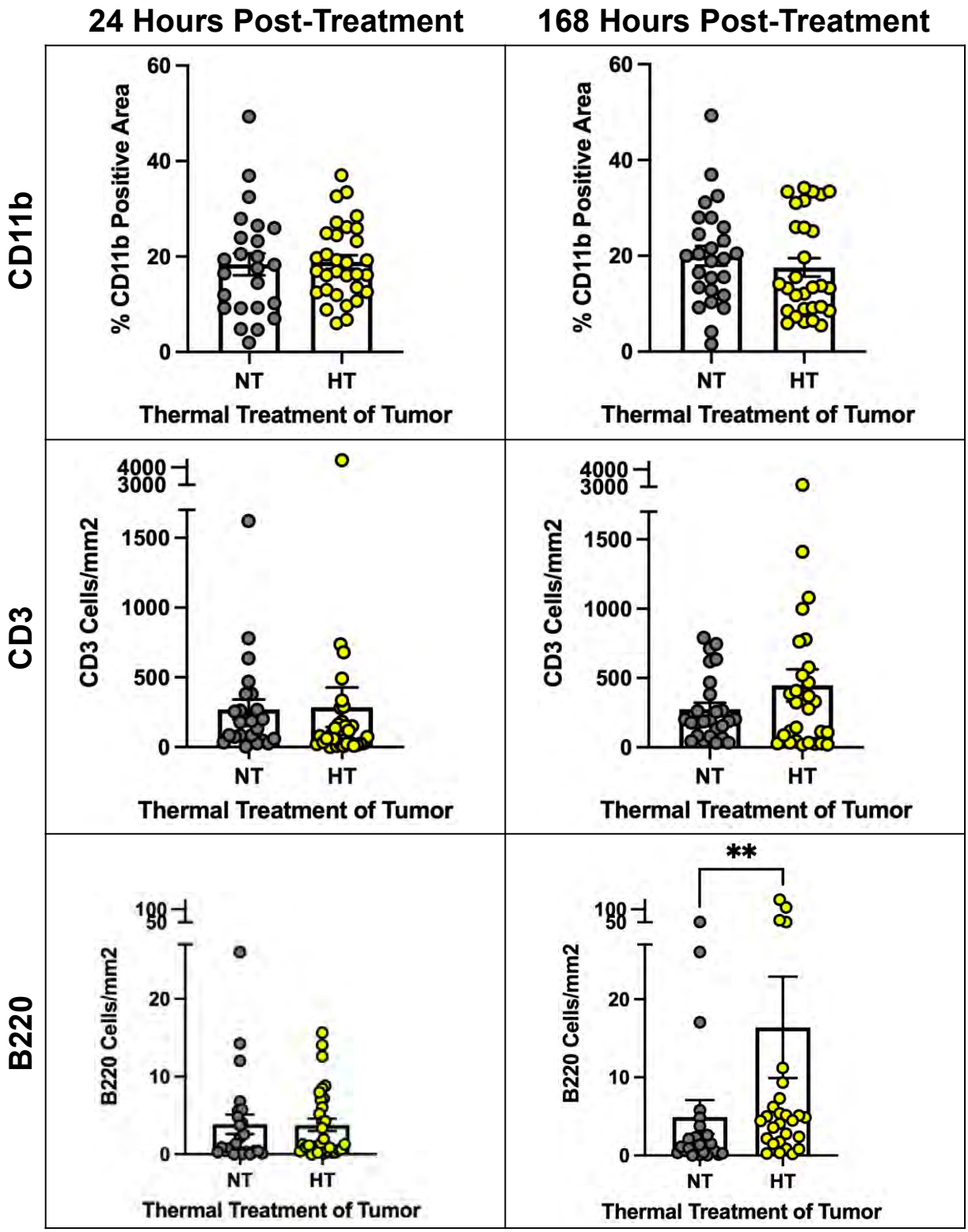

Figure 2. Quantification of B220, CD3 and CD11b staining of whole cross sections of treated tumors (NT-normothermia, HT-hyperthermia). Scale bars vary between graphs. n=99. Error bars: mean ± SEM. ** indicates significance with a p value < 0.01. B220 168h p=0.0042.

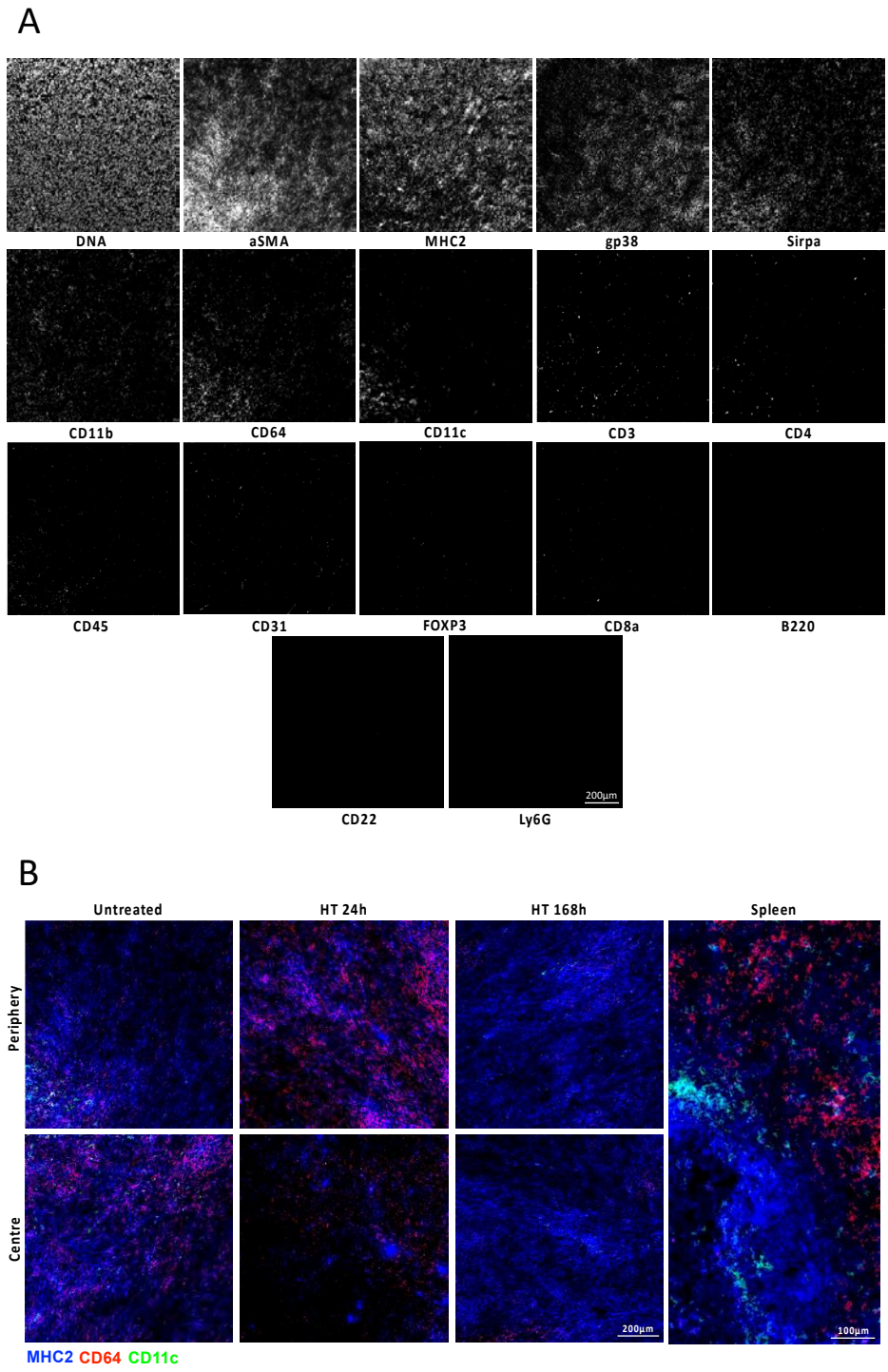

Figure 3. A) Imaging mass cytometry of one region of interest in the periphery of an untreated tumour. For information on the panel of markers used see table 4. Scale bar applies to all images. B) Imaging mass cytometry of MHC2 (blue), CD64 (red), and CD11c (green) markers of central and peripheral tumour regions of interest. HT = hyperthermia. Periphery: an ROI within 1mm of the tumour's edge. Centre: an ROI further than 1mm from the tumour's edge. Scale bars for tumour cross sections are all the same.

References

1. Ferrari A, Dirksen U, Bielack S. Sarcomas of Soft Tissue and Bone. *Tumors in Adolescents and Young Adults*. 2016;43:128-141. doi:10.1159/000447083
2. Williamson D, Missiaglia E, de Reyniès A, et al. Fusion gene-negative alveolar rhabdomyosarcoma is clinically and molecularly indistinguishable from embryonal rhabdomyosarcoma. *J Clin Oncol*. 2010;28(13):2151-2158. doi:10.1200/JCO.2009.26.3814
3. Walther C, Mayrhofer M, Nilsson J, et al. Genetic heterogeneity in rhabdomyosarcoma revealed by SNP array analysis. *Genes, Chromosomes and Cancer*. 2016;55(1):3-15. doi:10.1002/gcc.22285
4. Chen C, Dorado Garcia H, Scheer M, Henssen AG. Current and Future Treatment Strategies for Rhabdomyosarcoma. *Frontiers in Oncology*. 2019;9:1458. doi:10.3389/fonc.2019.01458
5. Oberlin O, Rey A, Lyden E, et al. Prognostic Factors in Metastatic Rhabdomyosarcomas: Results of a Pooled Analysis From United States and European Cooperative Groups. *JCO*. 2008;26(14):2384-2389. doi:10.1200/JCO.2007.14.7207
6. Ayodele O, Razak ARA. Immunotherapy in soft-tissue sarcoma. *Curr Oncol*. 2020;27(Suppl 1):17-23. doi:10.3747/co.27.5407
7. Dancsok AR, Gao D, Lee AF, et al. Tumor-associated macrophages and macrophage-related immune checkpoint expression in sarcomas. *Oncoimmunology.* 2020 9(1). doi: 10.1080/2162402X.2020.1747340.
8. Wunker C. *Effect of MRgHIFU Generated Hyperthermia in Combination with Thermosensitive and Non-Thermosensitive Doxorubicin on Tumor Growth and the Immune Microenvironment of Rhabdomyosarcoma in an Immunocompetent Murine Model*. MSc Thesis, unpublished. University of Toronto.
9. Ellis S, Rieke V, Kohi M, Westphalen AC. Clinical applications for magnetic resonance guided high intensity focused ultrasound (MRgHIFU): Present and future. *Journal of Medical Imaging and Radiation Oncology*. 2013;57(4):391-399. doi:10.1111/1754-9485.12085
10. Mougenot C, Quesson B, de Senneville BD, et al. Three-dimensional spatial and temporal temperature control with MR thermometry-guided focused ultrasound (MRgHIFU). *Magnetic Resonance in Medicine*. 2009;61(3):603-614. doi:10.1002/mrm.21887
11. Wunker C, Piorkowska K, Keunen B, et al. Magnetic resonance guided high intensity focused ultrasound generated hyperthermia: A feasable treatment method in a murine rhabdomyosarcoma model. *J Vis Exp.* 2023 (191), e64544, doi:10.3791/64544.
12. Shen RN, Lu L, Young P, Shidnia H, Hornback NB, Broxmeyer HE. Influence of elevated temperature on natural killer cell activity, lymphokine-activated killer cell activity and lectin-dependent cytotoxicity of human umbilical cord blood and adult blood cells. *International Journal of Radiation Oncology, Biology, Physics*. 1994;29(4):821-826. doi:10.1016/0360-3016(94)90571-1
13. van der Zee J. Heating the patient: a promising approach? | Elsevier Enhanced Reader. doi:10.1093/annonc/mdf280
14. Toraya-Brown S, Fiering S. Local tumour hyperthermia as immunotherapy for metastatic cancer. *Int J Hyperthermia*. 2014;30(8):531-539. doi:10.3109/02656736.2014.968640

15. Repasky EA, Evans SS, Dewhirst MW. Temperature Matters! And Why it Should Matter to Tumor Immunologists. *Cancer Immunol Res*. 2013;1(4):210-216. doi:10.1158/2326-6066.CIR-13-0118
16. Dewhirst MW, Lee CT, Ashcraft KA. The future of biology in driving the field of hyperthermia. *Int J Hyperthermia*. 2016;32(1):4-13. doi:10.3109/02656736.2015.1091093
17. Huang L, Li Y, Du Y, et al. Mild photothermal therapy potentiates anti-PD-L1 treatment for immunologically cold tumors via an all-in-one and all-in-control strategy. *Nat Commun*. 2019;10(1):4871. doi:10.1038/s41467-019-12771-9
18. Kather JN, Hörner C, Weis CA, et al. CD163+ immune cell infiltrates and presence of CD54+ microvessels are prognostic markers for patients with embryonal rhabdomyosarcoma. *Sci Rep*. 2019;9(1):9211. doi:10.1038/s41598-019-45551-y
19. McKinnon T, Venier R, Yohe M, et al. Functional screening of FGFR4-driven tumorigenesis identifies PI3K/mTOR inhibition as a therapeutic strategy in rhabdomyosarcoma. *Oncogene*. 2018;37(20):2630-2644. doi:10.1038/s41388-017-0122-y
20. Petitprez F, de Reyniès A, Keung EZ, et al. B cells are associated with survival and immunotherapy response in sarcoma. *Nature*. 2020;577(7791):556-560. doi:10.1038/s41586-019-1906-8
21. Qian BZ, Pollard JW. Macrophage diversity enhances tumor progression and metastasis. *Cell*. 2010;141(1):39-51. doi:10.1016/j.cell.2010.03.014

IN VIVO DRUG SCREENING OF TUMOR, IMMUNE, AND VASCULAR RESPONSE WITHIN THE TUMOR MICROENVIRONMENT

Dave Mealiea, Gary Yu, Lili Li, Jason Fish, Andrea McCart
Division of General Surgery, Department of Surgery, University of Toronto, Toronto, Ontario

Purpose and hypothesis: Elements of the tumor microenvironment (TME), such as tumor associated innate immune cells, can have a variety of impacts both on cancer development as well as treatment response. As such, preclinical models that incorporate these elements are of critical importance in developing novel treatment strategies (1). Here we use a novel screening approach using a zebrafish (ZF) tumor xenograft model, which integrates many of the benefits of both in vitro and in vivo screening platforms. The model facilitates examination of treatment efficacy and mechanism of action in a biologically relevant context (2), while realizing the efficiencies of in vitro approaches to screening. We sought to assess the effect of immune-modulating combination therapies on colorectal tumors using this platform. We hypothesized that the ZF model could be used to select chemotherapeutic agents for use in combination with the viral mimic and immune modulator poly I:C, and that these combination treatments could improve the anti-tumor effects of chemotherapy alone through their impacts on components of the TME.

Methods: Using MC38 murine colon cancer cells, we evaluated 30 FDA-approved chemotherapeutics including antimetabolite and alkylating compounds, hormonal agents, and targeted therapies such as anti-vascular drugs and multi-kinase inhibitors. The anti-tumor, anti-vascular, and immunomodulatory effects of these drugs combined with poly I:C were compared to poly I:C, compound, and vehicle alone groups using a streamlined approach with confocal fluorescent microscopy. Tumor cells were labeled with the Qtracker™ 585 Cell Labeling Kit (ThermoFisher Scientific, MA, USA). Cells were injected into the perivitalline space of ZF embryos 2 days post fertilization (DPF), which are transparent and allow in vivo confocal fluorescent imaging. Following 24 hours of tumor establishment to allow for neovascularization and immune cell infiltration, baseline tumor volumes were estimated using confocal microscopy and image analysis software and embryos were randomly assigned to treatment groups consisting of either vehicle bath, chemotherapeutic bath alone (based on dosing determined from toxicity studies), or chemotherapeutic bath combined with poly I:C intravascular injections. Tumors were then re-evaluated on 6 dpf, and ZF strains with endothelial and innate immune cell fluorescent reporter lines were used to assess blood vessels, neutrophils, and macrophages within the TME. Finally, an MTS assay was used to compare in vivo results obtained using the ZF model with treatment group impact on tumor cell viability in vitro, in order to evaluate the role that components of the TME such as vasculature and immune cells may be playing.

Results: After initially confirming that our screening approach was able to detect differences in chemotherapeutic effect consistent with the known clinical efficacy of these drugs (data not shown), we demonstrated variable anti-tumor efficacy across our 60 screened treatment groups. 9 out of 60 screened groups demonstrated partial tumor response by RECIST criteria, with the majority of these candidate treatments being combination therapy including poly I:C (figure 1). The treatment group displaying the most substantial percent decrease in tumor size was methotrexate + poly I:C, demonstrating a 53.7 percent decrease in tumor size (figure 1). Other groups with partial response when combined with poly I:C included doxorubicin, imiquimod, celecoxib, gefitinib, osimertinib, and erlotinib. Finally, osimertinib and doxorubicin achieved partial response in the screen when given alone. Xenografts treated with alectinib, apalutamide, tamoxifen + poly I:C, crizotinib, and niraparib all demonstrated progressive disease (figure 1).

As with anti-tumor response, tumor-associated macrophage (TAM) density varied widely between treatment groups. TAM infiltration into tumors followed a bimodal pattern, with a subset

of groups being associated with a substantial increase in macrophage density, while other groups saw very little tumor infiltration or even a decrease (figure 2). The imiquimod monotherapy and thioguanine combined with poly I:C groups showed the largest increase in TAM density, whereas niraparib and tamoxifen monotherapies were associated with the lowest densities. Treatment groups including poly I:C were associated with greater TAM infiltration as well as greater anti-tumor response. Unlike with TAM response, tumor associated neutrophil (TAN) density in all treatment groups increased over the course each screening experiment, however almost all treatment groups were associated with lower TAN presence than in the control group (data not shown). Additionally, while a range of increases in TAN number existed across treatment groups, there did not appear to be a similar bimodal response of limited versus substantial tumor infiltration as seen with TAMs. Imiquimod and dacarbazine combined with poly I:C were associated with the largest increases in TAN density, while niraparib and lenalidomide monotherapy groups showed the lowest increase. As with macrophages, treatment groups with poly I:C trended toward higher levels of TAN presence and greater overall anti-tumor response.

Tumor vascularization was measured as a ratio of tumor vascular volume to overall tumor volume. There was a decrease in tumor vascularization across all treatment groups compared to the control group, and while half of the tested groups showed increases in tumor vasculature during the experimental window, the remaining groups had reduced vascularization. Control and osimertinib groups were associated with the largest increase in tumor vascular density, while ponatinib and lenolidomide were associated with the greatest reduction (data not shown).

In comparing candidate drugs across all screens, drugs varied in terms of degree of anti-tumor effect and whether this was associated with increased immune cell infiltration into the treated tumors or reduction in tumor-stimulated angiogenesis (figure 3). Two treatment groups, gefitinib + poly I:C and imiquimod + poly I:C, demonstrated partial tumor response along with large increases in TAM and TAN presence within xenografts and large anti-vascular effects (figure 3). There were also treatment groups, such as Osimertinib + poly I:C, for which partial tumor responses were associated with large amounts of TAM and TAN infiltration but increases in tumor vascularization (figure 3). Finally, other treatment groups demonstrated either partial response with only TAM (doxorubixin + poly I:C) or TAN (erlotinib + poly I:C) increases. While not designed to detect statistically significant changes in TME characteristics between treatment groups, our screen did appear to demonstrate a trend toward increased anti-tumor effect and innate immune cell infiltration when candidate drugs were used in combination with poly I:C. Specifically, TAM and TAN dynamics trended toward greater tumor infiltration in those groups in which candidate drugs were combined with poly I:C. There also appeared to be a trend toward increased anti-vascular effect in treatment groups including poly I:C. There were however several candidate compounds that were associated with larger anti-tumor effects when given alone as compared to when given along with poly I:C, and also demonstrating increased immune cell infiltration in the monotherapy context.

Finally, using an MTS assay to assess the in vitro impact that treatment groups had on MC38 cells, the addition of poly I:C was associated with a decrease in percent viability following a 72-hour treatment period for the majority of the candidate compounds (figure 3). This was consistent with results obtained using the ZF model. Few groups were associated with a substantial increase in viability with the addition of poly I:C, including dacarbazine and thioguanine. Differences were seen between results from the ZF model and MTS assay. While certain groups were associated similar impacts on tumor cells across both models (e.g. monotherapy with erlotinib, lomustine, and olaparib), other treatment groups displayed marked differences (e.g. crizotinib). There were also differences in the impact that the addition of poly I:C had between the ZF model and MTS assay (figure 3). In general, poly I:C was associated with a greater inhibitory effect on tumor cells in the ZF model compared to the MTS assay. For instance, the addition of poly I:C to imiquimod was associated with an improved reduction in

tumor cell viability of 3.5% over imiquimod alone in the MTS assay, whereas in the ZF model adding imiquimod was associated with 37.6% improvement in anit-tumor effect (figure 3).

Conclusions: In summary, using a ZF tumor xenograft model as a screening platform for combinatorial treatment of colon cancer we have shown that induction of anti-viral responses within colorectal tumors with the viral mimic poly I:C may improve the anti-tumor effects of currently available chemotherapeutic agents. Additionally, in vivo screening using the ZF model is a novel and feasible approach to identifying candidate combinations for further in depth evaluation for colorectal cancer treatment.

Given that various elements of the TME are increasingly appreciated to impact tumor growth and treatment efficacy, preclinical models incorporating these elements are critically important in developing novel treatment strategies (1). The approach to drug screening used here employs an intact, biologically relevant TME through which to evaluate anti-tumor and TME-modulating effects of various combination therapies. Agents that produce anti-viral and immunogenic responses in the TME used with other treatment modalities such as cytotoxic chemotherapeutics may produce synergism through processes such as immune system activation (3). For instance, our lab previously shown that an oncolytic vaccinia virus used in combination with irinotecan potentiates the effects of this topoisomerase inhibitor, likely though cell cycle impacts of vaccinia infection and the enhanced apoptosis occurring in the context of S-phase accumulation in tumor cells (4).

Our data demonstrated a greater degree of anti-tumor effect and innate immune infiltration in those treatment groups including poly I:C. Out of the 9 treatment groups associated with partial tumor response, 7 were combinations of drug and poly I:C, and for 6 of these the corresponding drug monotherapy was not associated with partial response. MTS assessment of these treatments demonstrated different impact on tumor cells that suggested the possibility of other elements in the intact xenograft TME, such as innate immune cell and vascular dynamics, impacting treatment effect in our model. Previous studies have suggested mechanisms through which poly I:C may interact with chemotherapeutic agents in reinforcing ways. For instance, many drugs upregulate TLR3 receptor expression on tumor cells through processes such as p53 induction, which can lead to increased apoptosis following poly I:C exposure (5). This has been demonstrated in colorectal cancer cells specifically (5).

While some of the data suggesting synergism between poly I:C with other treatment modalities relies on tumor-specific adaptive immune responses, innate immune mechanisms are likely also at play (6). Interestingly, our screen showed that poly I:C in combination with imiquimod was associated with one of the largest anti-tumor effects as well as with the highest level of macrophage recruitment to tumors. Imiquimod also works in part through TLR signaling, and other groups have shown that combination therapy of poly I:C with other TLR agonists results in a greater degree anti-tumor macrophage polarization with associated TAM cytotoxicity against tumor cells and overall anti-tumor effect (7).

The colorectal TME is a complex system of interacting immune, vascular, and stromal structures above and beyond tumor cells themselves. Screening efforts to identify treatment approaches with potential benefit in colorectal cancer should strive to incorporate effects mediated through these variables. We have used the ZF xenograft model to evaluate how tumors are being modified by perceived viral challenge in combination with known chemotherapeutic agents, and how this may be harnessed for more efficacious treatment effect. Through this, we have identified treatment candidates that are associated with a partial tumor response by RECIST criteria in MC38 xenografts, with improved effect with poly I:C-based combination approaches over monotherapy, and modification of the TME, warranting further investigation for use in colorectal cancer treatment.

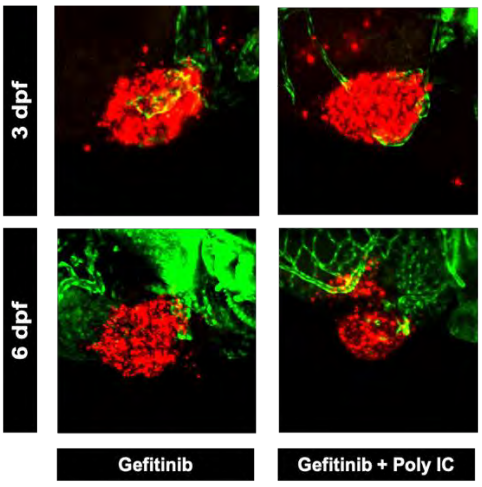

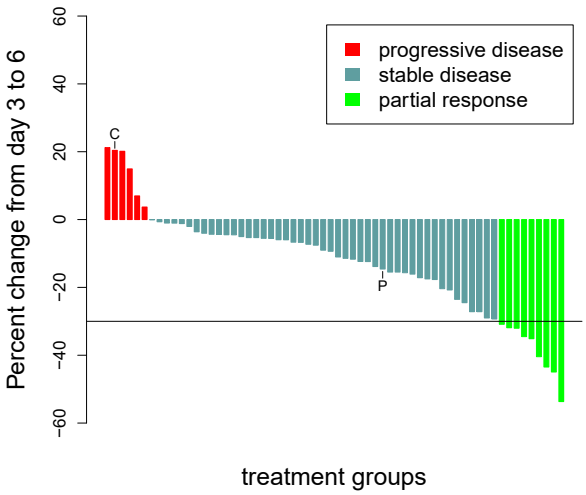

(a) (b)

alectinib	21.2	amifostine	-4.5	lomustine	-11.0	cyclophosphamide	-23.5
apalutamide	20.1	lenolidomide + poly I:C	-4.5	paclitaxel + poly I:C	-11.5	darcarbazine	-24.5
tamoxifen + Poly IC	14.9	thioguanine	-5.0	dacarbazine + poly I:C	-11.7	methotrexate	-27.2
crizotinib	7.0	idarubicin	-5.3	lomustine + poly I:C	-12.4	vincristine + poly I:C	-27.2
niraparib	3.7	idarubicin + poly I:C	-5.3	docitaxel + poly I:C	-12.4	cyclophosphamide + poly I:C	-29.0
crizotinib + poly I:C	-0.1	ponatinib + poly I:C	-5.6	raloxifene	-13.9	raloxifene + poly I:C	-29.3
alectinib + poly I:C	-0.7	trifluorodine	-5.6	votinostat + poly I:C	-15.5	doxorubicin	-30.9
talazoparib	-1.1	imiquimod	-6.0	vincristine	-15.5	erlotinib + poly I:C	-31.9
tamoxifen	-1.1	apalutamide + poly I:C	-6.0	gefitinib	-15.7	osimertinib + poly I:C	-32.1
ponatinib	-1.2	vorinostat	-6.7	thalidomide	-16.1	osimertinib	-34.5
olaparib	-2.1	docitaxel	-6.8	topotecan + poly I:C	-17.2	gefitinib + poly I:C	-35.2
trifluorodine + poly I:C	-3.6	talazoparib + poly I:C	-7.3	thalidomide + poly I:C	-17.5	celecoxib + poly I:C	-40.4
amifostine + poly I:C	-4.1	topotecan	-7.6	celecoxib	-17.7	imiquimod + poly I:C	-43.5
lenolidomide	-4.4	olaparib + Poly IC	-9.0	thioguanine + poly I:C	-20.4	doxorubicin + poly I:C	-45.0
nirapanib + poly I:C	-4.4	paclitaxel	-9.4	erlotinib	-20.8	methotrexate + poly I:C	-53.7

(c)

Figure 1. Tumor response. ZF implanted with fluorescent-labelled MC38 colon cancer cells (red) 2 days post fertilization (dpf) and treated with control (buffer) or candidate drug dissolved in ZF media beginning 3 dpf as well as either poly I:C or PBS injections into the common cardinal vein at 3 dpf. **a.** representative confocal images showing stable disease (gefitinib alone, left panels) versus progressive disease (gefitinib + poly I:C, right panels) **b.** waterfall plot, with treatment groups arranged along x axis from largest increase in tumor size to largest decrease, line denoting RESIST criteria cutoff for partial response, associated treatment group details listed in (c). **c.** treatment groups categorized as progressive disease (red, increase in tumor size), stable disease (dark green, no change to 30% decrease in size), and partial response (light green, >30% decrease in size).

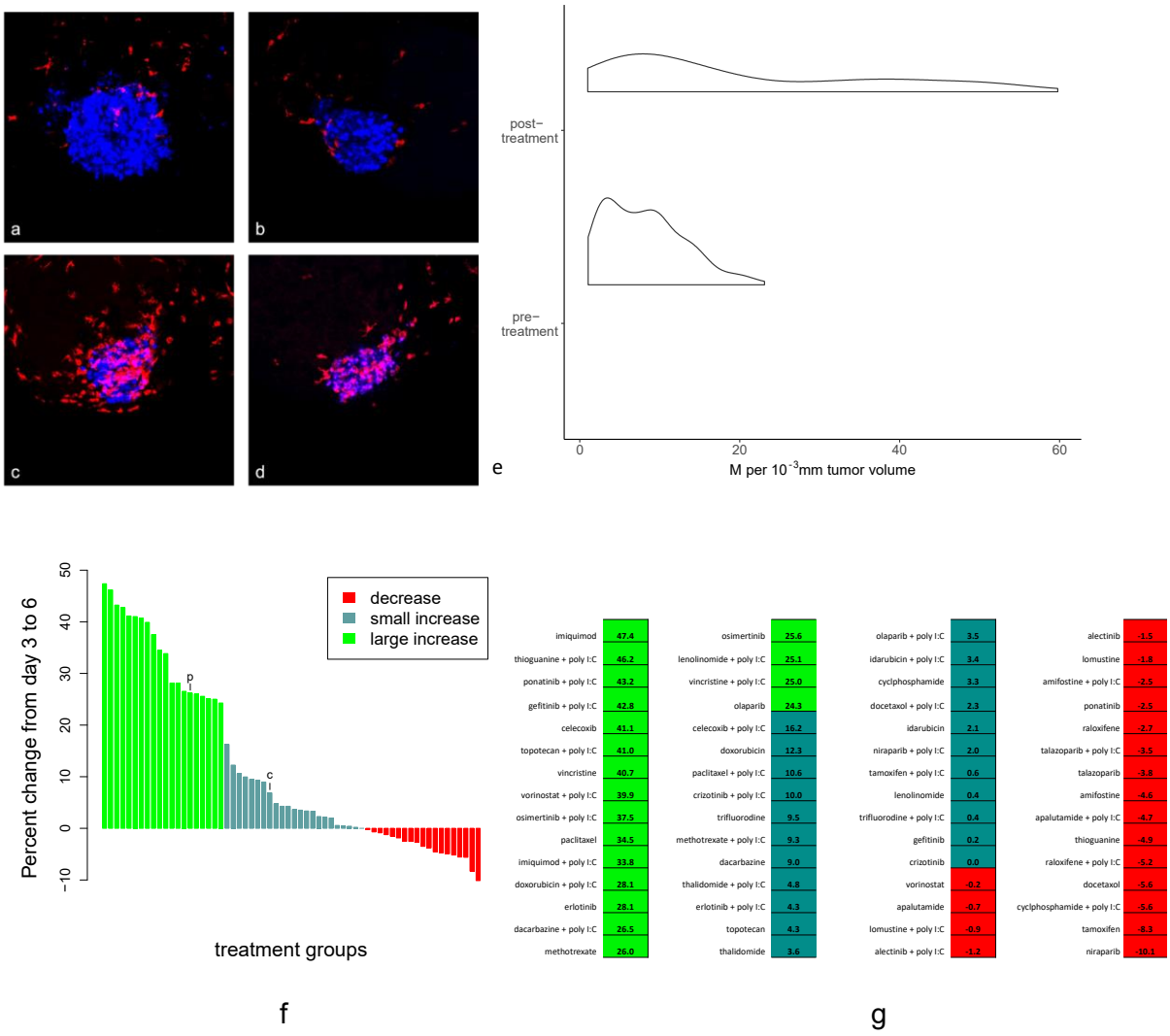

Figure 2. TAM response across treatment groups. ZF with macrophage reporter cell line (macrophages in red) implanted with blue Celltracker fluorescent-labelled MC38 cells. **a-d.** confocal fluorescent images comparing macrophage infiltration in tumors in those without (a,b) and with (c,d) substantial increase in TAM numbers. **e**. Raincloud plot comparing pre-treatment (green) and post-treatment (orange) TAM density, demonstrating bimodal macrophage response. The tail on the post-treatment distribution represents treatment groups associated with substantial increases in TAM presence, suggesting these treatment groups are stimulating activation in the TME. **f.** waterfall plot showing change in macrophage density (macrophages per 1 million cubic microns) from 3 to 6 dpf, with treatment groups arranged along x axis from largest increase in density to largest decrease, with the associated treatment group details listed in (g). **g**. Treatment groups categorized as decreased TAM density (red), small increase (dark green, 0-20/mm3), and large increase (light green, >20/mm3).

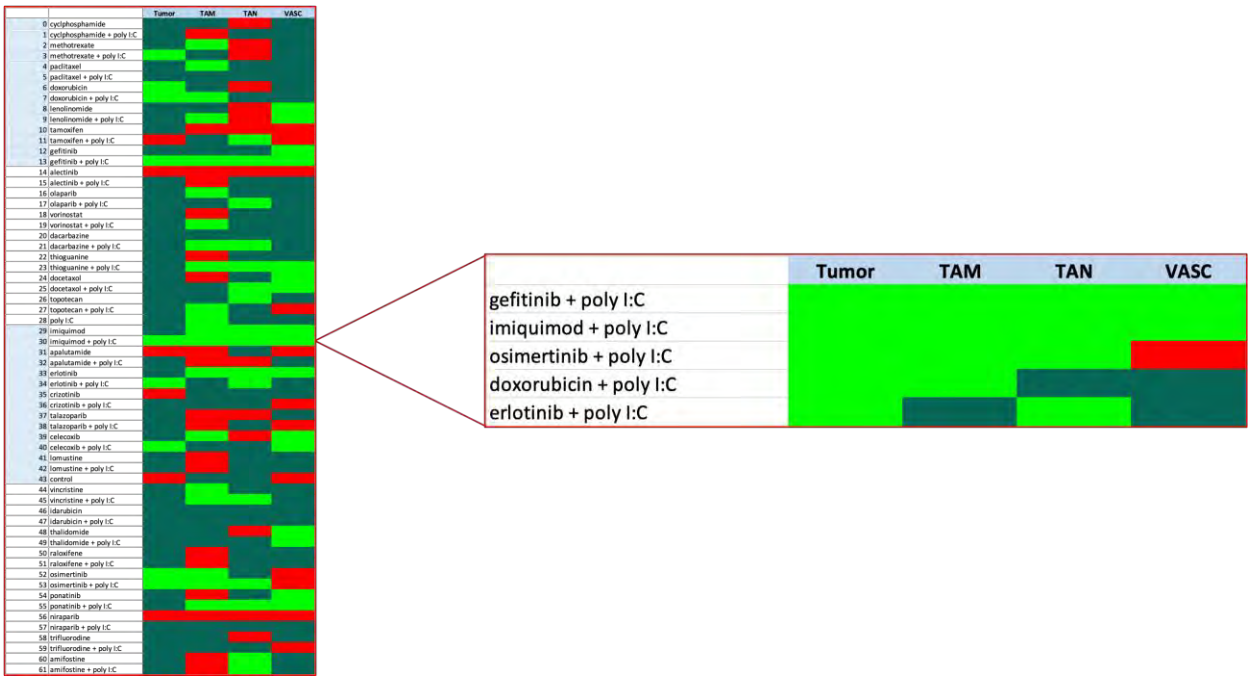

(a)

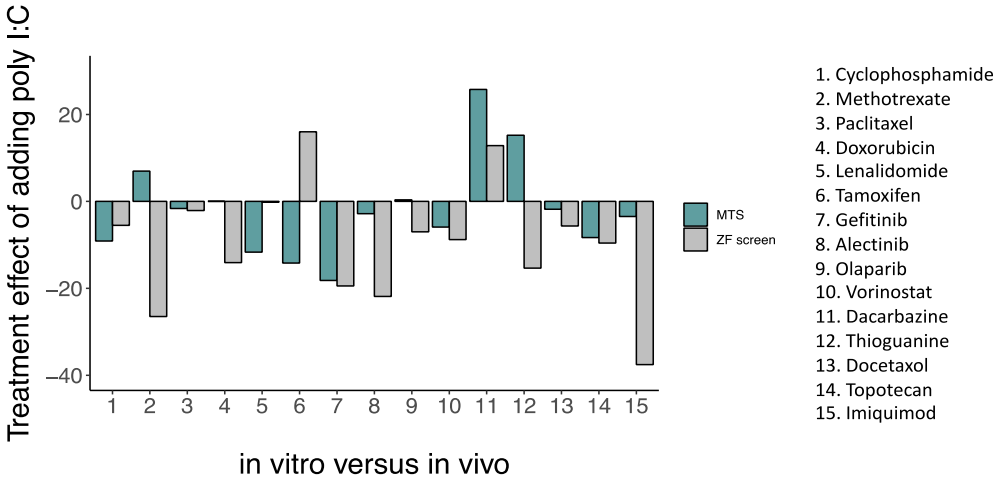

(b)

Figure 3. Overall screen results and comparison to in vitro data. **a.** Summary of screen result for all 30 candidate drugs with and without poly I:C, as well as poly I:C alone, comparing tumor response with innate immune and vascular changes with the tumor microenvironment. Right panel showing subset of candidate compounds selected for further in depth evaluation based on their anti-tumor, immunomodulatory, and vascular impacts. **b.** Comparison of change in anti-tumor effect with the addition of poly I:C in vitro and in vivo in a representative subset of treatment groups. Differences in change in tumor volume for each candidate compound when combination therapy with poly I:C is compared to treatment with candidate drug alone, as assessed using MTS assay (green bars) or using the ZF tumor xenograft model (grey bars). More positive values denote less anti-tumor effect in the poly I:C combination therapy group compared to the monotherapy group, while more negative values denote a great anti-tumor effect with poly I:C.

References

1. Yoon PS, Del Piccolo N, Shirure VS, Peng Y, Kirane A, Canter RJ, et al. Advances in Modeling the Immune Microenvironment of Colorectal Cancer. Frontiers in Immunology. 2021;11.
2. Cornet C, Dyballa S, Terriente J, Di Giacomo V. ZeOncoTest: Refining and Automating the Zebrafish Xenograft Model for Drug Discovery in Cancer. Pharmaceuticals. 2019;13(1):1.
3. Martin NT, Bell JC. Oncolytic Virus Combination Therapy: Killing One Bird with Two Stones. Molecular Therapy. 2018;26(6):1414-22.
4. Ottolino-Perry K, Acuna SA, Angarita FA, Sellers C, Zerhouni S, Tang N, et al. Oncolytic vaccinia virus synergizes with irinotecan in colorectal cancer. Mol Oncol. 2015;9(8):1539-52.
5. Taura M, Fukuda R, Suico MA, Eguma A, Koga T, Shuto T, et al. TLR3 induction by anticancer drugs potentiates poly I:C-induced tumor cell apoptosis. Cancer Science. 2010;101(7):1610-7.
6. Francis L, Guo ZS, Liu Z, Ravindranathan R, Urban JA, Sathaiah M, et al. Modulation of chemokines in the tumor microenvironment enhances oncolytic virotherapy for colorectal cancer. Oncotarget. 2016;7(16):22174-85.
7. Anfray C, Mainini F, Digifico E, Maeda A, Sironi M, Erreni M, et al. Intratumoral combination therapy with poly(I:C) and resiquimod synergistically triggers tumor-associated macrophages for effective systemic antitumoral immunity. J Immunother Cancer. 2021;9(9).

CHARACTERIZING HYPOXIA ASSOCIATED GENETIC FEATURES IN EXTREMITY SOFT TISSUE SARCOMA

Jen Dorsey[1,2], Joanna Przybyl[3,4], Peter Ferguson[5], Kim Tsoi[5], Jay Wunder[5], Peter Chung[6,7], Edward Taylor[6,8], Patrick Veit-Haibach[9], Elizabeth Demicco[10], Rebecca Gladdy[1,2,5], David Shultz[6,7]

[1]Institute of Medical Science, University of Toronto, Toronto, Canada
[2]Lunenfeld-Tanenbaum Research Institute, Toronto, Canada
[3]Department of Surgery, McGill University, Montreal, Canada
[4]Cancer Research Program, Research Institute – McGill University Health Centre, Montreal, Canada
[5]Department of Surgery, University of Toronto, Toronto, Canada
[6]Radiation Oncology, University of Toronto, Toronto, Canada
[7]Radiation Oncology, Princess Margaret Cancer Centre, Toronto, Canada
[8]Medical Physicist, Princess Margaret Cancer Centre, Toronto, Canada
[9]Medical Imaging, University of Toronto, Toronto, Canada
[10]Department of Pathology and Laboratory Medicine, Mount Sinai Hospital, Toronto, Canada

Translational Research

Introduction

Soft tissue sarcomas (STS) are a diverse group of mesenchymal tumors with over 100 histologically distinct types recognized by the World Health Organization (WHO) (Board, 2020). Two common STS types in adults are undifferentiated pleomorphic sarcoma (UPS) and myxofibrosarcoma (MFS). Both types are commonly found in the extremities (Board, 2020). Metastasis occurs in up to 50% of cases and as such, there is an apparent role for systemic therapy in improving rates of cure. Unfortunately, neither UPS nor MFS is highly sensitive to standard of care chemotherapeutics, such as doxorubicin, with response rates of about 20% (Seddon et al., 2017; Verschoor et al., 2020). Thus, there is a need to better understand the mechanisms of metastasis to improve outcomes.

One known driver of aggressive disease and metastasis in cancer is intratumoral hypoxia. Markers of hypoxia, such as HIF-1α, have been linked to STS growth and metastasis, however the mechanisms of this are not well elucidated (Eisinger-Mathason et al., 2013; El-Naggar et al., 2015; Forker et al., 2018; Kim et al., 2015; Li, Zhang, Li, & Tu, 2016; Nystrom, Jonsson, Werner-Hartman, Nilbert, & Carneiro, 2017). Transcriptome changes associated with hypoxia have been identified in STS (Aggerholm-Pedersen et al., 2016; Yang et al., 2018), which may occur through epigenetic modifications through inactivation of tumor suppressor genes such as *PTEN* and *ATM* (Thienpont et al., 2016). Overall, the mechanisms of hypoxia driven metastasis are yet to be fully understood and additional large-scale sequencing studies may provide valuable insight.

A formidable challenge in hypoxia research is that it is difficult to accurately measure intratumoral hypoxia in clinical specimens. IHC of HIF-1α, as well as proteins upregulated by HIF-1α such as CA-IX are frequently used to evaluate the presence of hypoxia in STS and correlate to worse survival (Forker et al., 2018; Kim et al., 2015; Li et al., 2016; Nystrom et al., 2017; Oda et al., 2009; Smeland et al., 2012). Hypoxia induced gene-expression signatures for STS have been reported (Aggerholm-Pedersen et al., 2016; Yang et al., 2018). In addition, exogenous hypoxia probes, such as pimonidazole, are available and have been validated in other solid tumors (Dhani et al., 2015). However, these methods rely on sampling specific regions of the tumor and therefore may not represent the total hypoxic fraction.

A potentially more accurate way of determining hypoxic fraction is through live imaging. One such way is with positron emission tomography (PET) in combination with a 2-nitroimadazole radiotracer of hypoxia, such as 18F-Fluoroazomycin arabinoside (FAZA). Assessing hypoxia in sarcoma was previously done with FAZA-PET/ CT in a small phase Ib/II clinical trial of STS where over 50% of tumors were characterized as hypoxic, which was associated with both radioresistance and local recurrence (Lewin et al., 2014). Further studies of how FAZA-PET combined with conventional imaging modalities can quantify hypoxia and relate to clinical outcomes are requires to better understand the clinical utility of hypoxia imaging.

To address both the question of how to quantity total hypoxic fraction in STS and its impact on survival and gene expression we conducted a Phase II clinical trial (ClinicalTrial.gov Identifier: NTC03418818). Hypoxia was assessed first with FAZA-PET/MRI and correlative studies were conducted post-surgery to better understand the impact of hypoxia on the methyl- and transcript-ome. Furthermore, pimonidazole was used to validate FAZA results. Finally, to further study hypoxia in a controlled environment, STS cell lines were also utilized. Overall, our studies showed that there is variability in tumor hypoxia percentages in UPS and MFS, based on both FAZA-PET/MRI and pimonidazole staining, which is associated with worse disease-free survival. Preliminary analysis also indicates that methylation may not be altered by hypoxia.

Methods

We conducted a dual arm, single centre, investigator-initiated study to investigate the use of FAZA-PET/MRI to measure hypoxia in STS before and after neo-adjuvant radiation (Arm A) or before surgery (Arm B). Patients in Arm B received pimonidazole approximately 16-20 hours

before surgery. Eligible patients were aged 18 years or older with histologically documented, high-risk. Patients with UPS or MFS were preferentially enrolled. Intention to treat using radiation/chemotherapy/surgery was according to the current treatment policies of the sarcoma site group at Princess Margaret Cancer Centre and Mount Sinai Hospital. FAZA-PET/MRI scans were performed at Toronto General Hospital. To calculate tumor hypoxic fraction, the average uptake of FAZA in the normal muscle plus three standard deviations defined positivity for hypoxia in the tumor. This was done individually for each patient.

Tissue was harvested immediately after tumor resection for correlative studies. Approximately six grossly viable regions were sampled and fixed in formalin. Additionally, one larger tumor sample, approximately 1 to 2 cm^3 was collected for dissociation. Viable regions were stained for pimonidazole, CA-IX and HIF-1α. An expert sarcoma pathologist (ED) scored the IHC staining and provided quantitative statements that included percent of tissue positive for each marker and intensity of the stain. Dissociated tumor cells were isolated based on pimonidazole status (positive (+) or negative (-)) using a MoFlo Astrios EQ cell sorter for downstream methylation analysis. DNA was extracted and bisulfite conversion was performed using the EZ DNA Methylation Kit. Samples were analyzed on the Illumina Infinium MethylationEPIC Array at the Princess Margaret Genomic Centre (PMGC). RNA was extracted and real-time quantitative polymerase chain reaction (RT-qPCR) acquisition was performed to quantify the expression of CA-IX in hypoxic cells (0.2% O_2) relative to normoxic (18.6% O_2).

Results

In total, 15 patients in Arm A and 10 patients in Arm B were accrued (n= 25) between 2018 and 2022. Patients with UPS and MFS were preferentially enrolled. Baseline demographics of patients enrolled in the study and specifically patients involved in correlative studies are shown in **Table 6-1 A** and **B**, respectively. Most patients were male (n=23/25), and the most common histology was MFS (n=11/25) followed by UPS (n=8/25). One patient had an MPNST, and as with standard clinical practice this tumor was not assigned a grade; for the remaining tumors, half were grade 2 (n=12/15) and half were grade 3 (n=12/25). In total 20 patients had at least one successful FAZA-PET/MRI (**Table 6-1 A**). One patient enrolled in Arm B did not take pimonidazole prior to surgery and was excluded from correlative studies. All patients in Arm A (n=15) and 70% patients in Arm B (n=7/10) underwent baseline FAZA-PET/MRI imaging to quantify the hypoxic fraction of the tumor. However, for 2 patients (Arm A n=1, Arm B n=1), FAZA/PET scans were compromised due to scanner errors and thus only 20 patients had usable scans. At baseline, 14 patients demonstrated quantitative evidence of hypoxia with a median of 16% [2 – 62%] of the tumor being FAZA avid and six patients appeared normoxic (0% of the tumor was FAZA avid).

Preliminary analysis indicates that hypoxia correlated to both disease-free and overall survival (**Figure 6-1 A** and **B,** respectively). One patient did not undergo surgical resection because they developed metastatic disease and thus, they were excluded from analysis. There was a statistically significant difference for disease-free survival only ($p<0.05$) (**Figure 6-1 A**). All patients enrolled had tumors of grade 2 or 3, this was not correlated to the percent of hypoxia in STS ($p=0.4064$) (**Figure 6-1 C**).

We aimed to assess the hypoxic fraction within viable tumor regions. To determine if the regions sampled were viable, H&E slides were reviewed by an expert sarcoma pathologist (ED). Early on, we noted that tumors treated with neoadjuvant radiation (n=3) had very low viability (1% median viable tumor) and thus we focused on performing correlative studies only on patients enrolled in Arm B (**Table 6-3, Figure 6-2 A**)**.** There was heterogeneity in the proportion of pimonidazole stain between patients (interpatient; range 0% to 90%) and between regions surveyed within the same tumor (intrapatient) (**Figure 6-2 B**). The largest intrapatient heterogeneity was seen in patient 10, with a range of 0% to 90%. Pimonidazole was detected in both the nucleus and cytoplasm. Pimonidazole staining was cord-like in some instances, as has

previously been reported (Dhani et al., 2015). In some tumors, pimonidazole was noted adjacent to necrotic regions in a serpiginous pattern. In others, pimonidazole was detected more diffusely or in small patches without a clear relationship to necrotic areas (**Figure 6-2 C**). Examples of quantification statements, with percentage pimonidazole positive and intensity of stain, as well as descriptions of staining location are provided in **Figure 6-2 D**. IF was also used to measure co-localization of pimonidazole, CA-IX, and HIF-1α to investigate the extent of single positive, double positive, and triple positive cells. Overall, we observed colocalization between hypoxia markers (**Figure 6-2 E**), validating pimonidazole in STS as a marker of hypoxia.

To determine if DNA methylation was altered by hypoxia, we are in the process of analyzing global methylation patterns and methylation within specific hypoxia related genes. In total, six patient tumors were sorted to isolate hypoxic (pimonidazole +) and normoxic (pimonidazole -) cells. Of the six patient samples sorted, four samples had an adequate amount of DNA. To compliment the *ex vivo* studies, we utilized hypoxic and normoxic STS cell lines for methylation analysis. Included were four UPS and five MFS cell lines, each of which was plated in a hypoxic (0.2% O_2) or normoxic (18.6% O_2) incubator for 72 hours prior to harvest. To confirm that STS cell lines responded to 72 hours of hypoxia (0.2% O_2), we quantified CA-IX mRNA expression. In all UPS and MFS cell lines there was an increase in CA-IX expression when compared to the normoxic cell lines. Preliminary analysis of these UPS cell lines indicated no hypoxia-induced global methylation changes.

Conclusion

Hypoxia is a known driver of metastasis in cancer, however, the mechanisms of this have not been fully elucidated. Furthermore, the gold standard of assessing hypoxia in clinical standards remains to be determined. Here, we demonstrated that measuring hypoxia with FAZA-PET/MRI is feasible for quantifying hypoxia in STS. Furthermore, we are currently investigating if hypoxia alters either the methyl- or transcript-ome, but preliminary analysis indicates that methylation may not be altered by hypoxia in STS cell lines.

Interim analysis of a small cohort of STS patients, hypoxia detected by FAZA-PET/MRI correlated with worse disease-free survival in STS. While overall survival was not significantly impacted by hypoxia, there does appear to be a trend towards worsened overall survival with hypoxia. The amount and patterns of pimonidazole staining varied between patients and within tumors. The majority of staining was cord-like, as has previously been described (Dhani et al., 2015), but we also observed diffuse and patchy staining, particularly in UPS and MFS tumors. While colocalization of pimonidazole to known hypoxia markers, HIF-1α and CA-IX, was not uniform, several regions stained positive for all three markers.

To further understand the mechanism of change induced by hypoxia, we assessed DNA methylation. Our preliminary analysis indicates that global methylation may not be affected by hypoxia. It is possible that with a larger sample size we would be able to detect differences either on the global or gene specific level.

Overall, we have shown that hypoxia can be detected and quantified in STS, which correlated to worse survival. Both FAZA-PET/MRI and pimonidazole are complimentary classifiers of hypoxia, as the total hypoxic fraction can be determined but also in relation to other morphologic features, such as necrosis. Currently, we are determining if there are methylation changes caused by hypoxia and in the future we would like to correlate this to transcriptome changes.

Translational Research

References

Aggerholm-Pedersen, N., Sorensen, B. S., Overgaard, J., Toustrup, K., Baerentzen, S., Nielsen, O. S., . . . Safwat, A. (2016). A prognostic profile of hypoxia-induced genes for localised high-grade soft tissue sarcoma. *Br J Cancer, 115*(9), 1096-1104. doi:10.1038/bjc.2016.310

Board, W. C. o. T. E. (2020). *WHO Classification of Tumors of Soft Tissue and Bone* (Vol. 3). Lyon, France: IARC Press.

Dhani, N. C., Serra, S., Pintilie, M., Schwock, J., Xu, J., Gallinger, S., . . . Hedley, D. W. (2015). Analysis of the intra- and intertumoral heterogeneity of hypoxia in pancreatic cancer patients receiving the nitroimidazole tracer pimonidazole. *Br J Cancer, 113*(6), 864-871. doi:10.1038/bjc.2015.284

Eisinger-Mathason, T. S., Zhang, M., Qiu, Q., Skuli, N., Nakazawa, M. S., Karakasheva, T., . . . Simon, M. C. (2013). Hypoxia-dependent modification of collagen networks promotes sarcoma metastasis. *Cancer Discov, 3*(10), 1190-1205. doi:10.1158/2159-8290.CD-13-0118

El-Naggar, A. M., Veinotte, C. J., Cheng, H., Grunewald, T. G., Negri, G. L., Somasekharan, S. P., . . . Sorensen, P. H. (2015). Translational Activation of HIF1alpha by YB-1 Promotes Sarcoma Metastasis. *Cancer Cell, 27*(5), 682-697. doi:10.1016/j.ccell.2015.04.003

Forker, L., Gaunt, P., Sioletic, S., Shenjere, P., Potter, R., Roberts, D., . . . West, C. M. L. (2018). The hypoxia marker CAIX is prognostic in the UK phase III VorteX-Biobank cohort: an important resource for translational research in soft tissue sarcoma. *Br J Cancer, 118*(5), 698-704. doi:10.1038/bjc.2017.430

Kim, J. I., Choi, K. U., Lee, I. S., Choi, Y. J., Kim, W. T., Shin, D. H., . . . Sol, M. Y. (2015). Expression of hypoxic markers and their prognostic significance in soft tissue sarcoma. *Oncol Lett, 9*(4), 1699-1706. doi:10.3892/ol.2015.2914

Lewin, J., Khamly, K. K., Young, R. J., Mitchell, C., Hicks, R. J., Toner, G. C., . . . Thomas, D. M. (2014). A phase Ib/II translational study of sunitinib with neoadjuvant radiotherapy in soft-tissue sarcoma. *Br J Cancer, 111*(12), 2254-2261. doi:10.1038/bjc.2014.537

Li, Y., Zhang, W., Li, S., & Tu, C. (2016). Prognosis value of Hypoxia-inducible factor-1alpha expression in patients with bone and soft tissue sarcoma: a meta-analysis. *Springerplus, 5*(1), 1370. doi:10.1186/s40064-016-3064-x

Nystrom, H., Jonsson, M., Werner-Hartman, L., Nilbert, M., & Carneiro, A. (2017). Hypoxia-inducible factor 1alpha predicts recurrence in high-grade soft tissue sarcoma of extremities and trunk wall. *J Clin Pathol, 70*(10), 879-885. doi:10.1136/jclinpath-2016-204149

Oda, Y., Tateishi, N., Matono, H., Matsuura, S., Yamamaoto, H., Tamiya, S., . . . Tsuneyoshi, M. (2009). Chemokine receptor CXCR4 expression is correlated with VEGF expression and poor survival in soft-tissue sarcoma. *Int J Cancer, 124*(8), 1852-1859. doi:10.1002/ijc.24128

Seddon, B., Strauss, S. J., Whelan, J., Leahy, M., Woll, P. J., Cowie, F., . . . Beare, S. (2017). Gemcitabine and docetaxel versus doxorubicin as first-line treatment in previously untreated advanced unresectable or metastatic soft-tissue sarcomas (GeDDiS): a randomised controlled phase 3 trial. *Lancet Oncol, 18*(10), 1397-1410. doi:10.1016/S1470-2045(17)30622-8

Smeland, E., Kilvaer, T. K., Sorbye, S., Valkov, A., Andersen, S., Bremnes, R. M., . . . Donnem, T. (2012). Prognostic impacts of hypoxic markers in soft tissue sarcoma. *Sarcoma, 2012*, 541650. doi:10.1155/2012/541650

Thienpont, B., Steinbacher, J., Zhao, H., D'Anna, F., Kuchnio, A., Ploumakis, A., . . . Lambrechts, D. (2016). Tumour hypoxia causes DNA hypermethylation by reducing TET activity. *Nature, 537*(7618), 63-68. doi:10.1038/nature19081

Verschoor, A. J., Litiere, S., Marreaud, S., Judson, I., Toulmonde, M., Wardelmann, E., . . . Gelderblom, H. (2020). Survival of soft tissue sarcoma patients after completing six cycles of first-line anthracycline containing treatment: an EORTC-STBSG database study. *Clin Sarcoma Res, 10*, 18. doi:10.1186/s13569-020-00137-5

Yang, L., Forker, L., Irlam, J. J., Pillay, N., Choudhury, A., & West, C. M. L. (2018). Validation of a hypoxia related gene signature in multiple soft tissue sarcoma cohorts. *Oncotarget, 9*(3), 3946-3955. doi:10.18632/oncotarget.23280

Table 6-1. Baseline demographics of (A) all patients enrolled in the hypoxia clinical trial and (B) those involved in correlative studies. Three patients in Arm B did not undergo the optional FAZA scan. Two patients (Arm A n=1, Arm B n=1) underwent the FAZA scan but there were issues with the PET scan.

A

Characteristic		Patients (n)
Sex		25
	Male	23
	Female	2
Histology		
	UPS	9
	MFS	10
	DDLPS	1
	MLPS	2
	MPNST	1
	PECOMA	1
	Synovial Sarcoma	1
Treatment Group		
	Arm A: neoadjuvant RT + surgery	15
	Arm B: surgery	10
Grade		
	2	12
	3	12
	Not graded (MPNST)	1
Successful FAZA Scan?		
	Yes	20
	No	5

B

Characteristic		Patients (n)
Sex		13
	Male	13
	Female	0
Histology		
	UPS	5
	MFS	5
	DDLPS	1
	MLPS	1
	MPNST	1
Treatment Group		
	Arm A: neoadjuvant RT + surgery	10
	Arm B: surgery	3
Grade		
	2	5
	3	7
	Not graded (MPNST)	1
Successful FAZA Scan?		
	Yes	9
	No	4

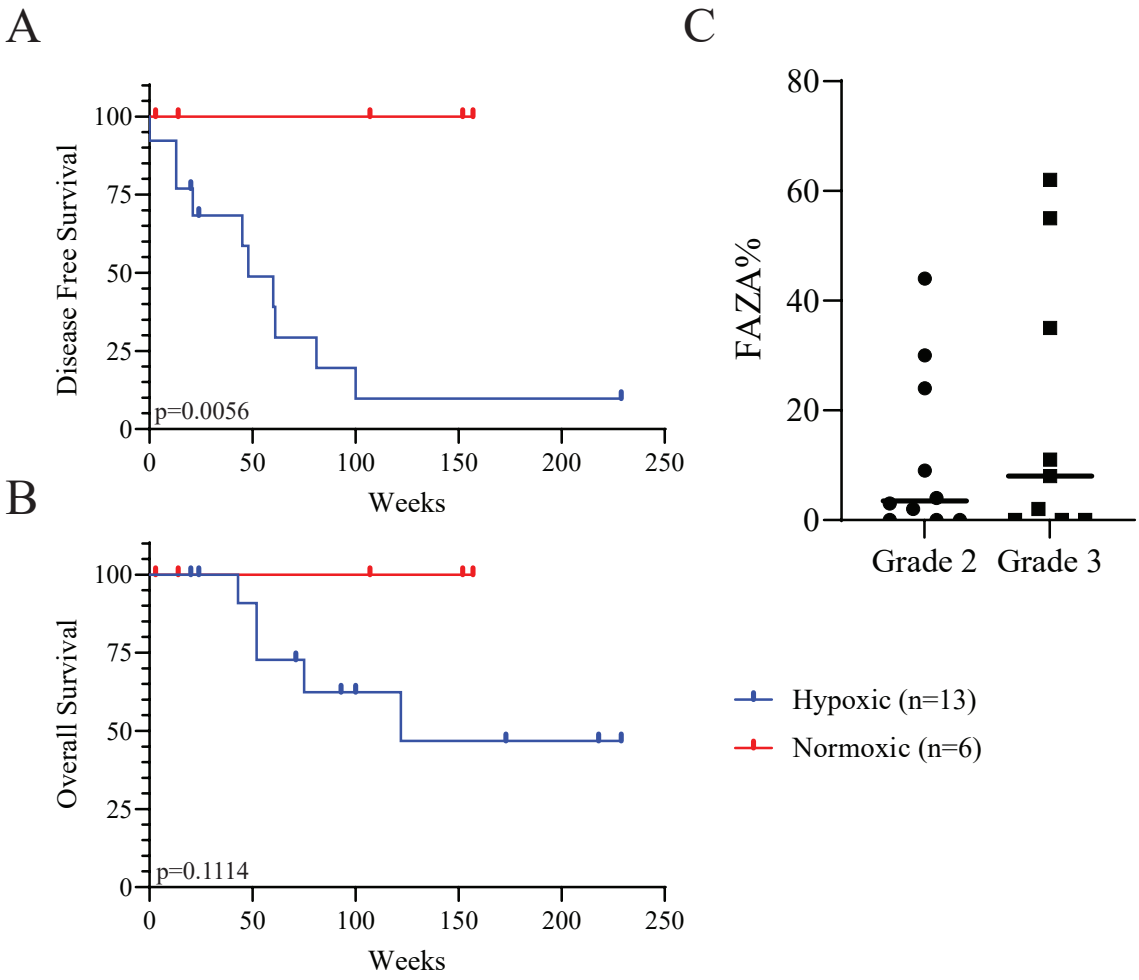

Figure 6-1. Survival of STS patients with hypoxic tumors is worse than those with normoxic tumors. Hypoxia was assessed using FAZA-PET/MRI imaging and hypoxic tumors were defined as any tumor that had FAZA avid regions. Although 20 patients underwent successful FAZA scans, one patient did not undergo surgery due to the detection of metastatic disease and thus was excluded from the analysis. (A) Disease free survival is significantly worse for patients with hypoxic tumors compared to normoxic tumors (p=0.0056). (B) There is a trend towards worse overall survival with patients with hypoxic tumors (p = 0.1114). (C) Hypoxia was not associated with tumor grade (p=0.4064).

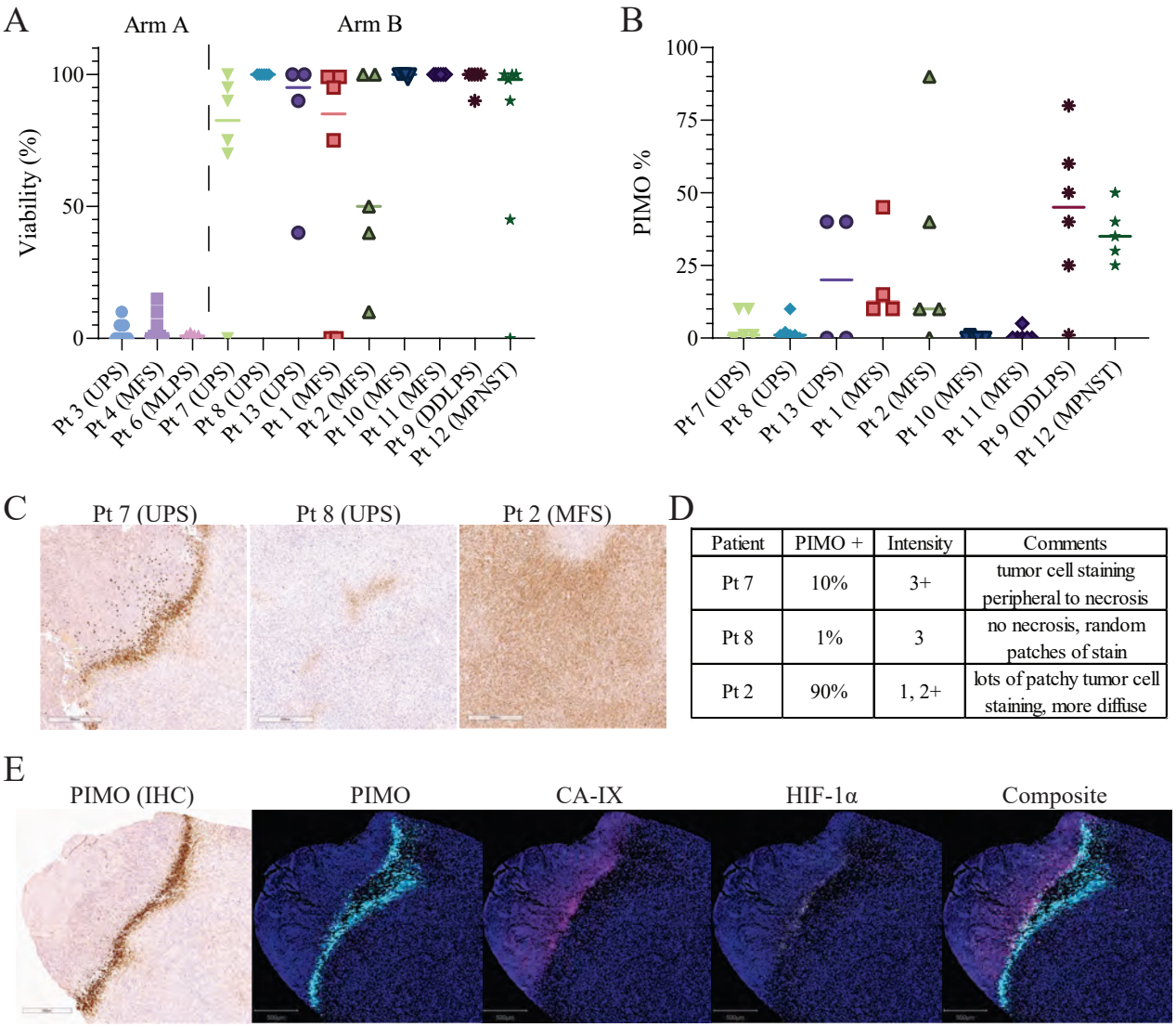

Patient	PIMO +	Intensity	Comments
Pt 7	10%	3+	tumor cell staining peripheral to necrosis
Pt 8	1%	3	no necrosis, random patches of stain
Pt 2	90%	1, 2+	lots of patchy tumor cell staining, more diffuse

Figure 6-2. Heterogeneity of pimonidazole is detected both interpatient and intrapatient in STS. Additionally, colocalization with endogenous hypoxia markers observed. (A) Tissue sampled from all patients enrolled in Arm A (neoadjuvant radiation) was significantly less viable than Arm B (surgery first). (B) Percent of tumor cells positive for pimonidazole (PIMO) in patients enrolled in Arm B (scored by an expert sarcoma pathologist (ED)). (C) Representative pimonidazole immunohistochemistry (IHC) for three patients with different staining patterns, left to right: cord like adjacent to necrosis (Pt 7 UPS), small patches (Pt 8 UPS), diffuse (Pt 2 MFS). From 8 patients, 29 slides were positive for pimonidazole with the following staining patterns: cord like (n=17), small patches (n=6), diffuse (n=2), cord like and diffuse (n=2), cord like and patches (n=2). (D) Table of percent and intensity, as well as description of pimonidazole stain of the three representative slides (ED). (E) Representative PIMO IHC with corresponding immunofluorescence (IF) of PIMO, CA-IX, HIF-1α, and composite image.

ESTABLISHMENT OF LUNG CANCER ORGANOIDS USING EBUS-TBNA SPECIMENS VIA XENOGRAFT TUMOR

Takamasa Koga[1], Hiroyuki Ogawa[1], Nhu-An Pham[2], Yuhui Wang[2], Ming Li[2], Nicholas Bernards[1], Alexander Gregor[1], Yuki Sata[1], Shinsuke Kitazawa[1], Yoshihisa Hiraishi[1], Tsukasa Ishiwata[1], Masato Aragaki[1], Fumi Yokote[1], Andrew Effat[1], Kate Kazlovich[1] Nikolina Radulovich[2], Ming-Sound Tsao[2], Kazuhiro Yasufuku[1, 3]

[1]Division of Thoracic Surgery, Toronto General Hospital, University Health Network, Toronto, Ontario

[2]Princess Margaret Cancer Center, University Health Network, Toronto, Ontario

[3]Institute of Biomedical Engineering, University of Toronto, Toronto, Ontario

Introduction and background

Patient-derived preclinical models, especially patient-derived organoids (PDO) using cancer cells, have been reported as novel approaches to predict drug-sensitivity and as a preclinical model to study drug resistance in multiple cancer types [1]. PDO using primary lung cancers also demonstrated potent ability to predict prognosis and drug sensitivity, as well as patient-derived xenografts (PDX) [2,3] . However, many of the reported lung cancer organoid (LCO) were derived from surgically resected samples of early-stage lung cancers. Even if we use the surgical resected lung cancer specimen, stable culture, especially passage more than ten of lung cancer cells is still difficult because of the contamination and outgrowth of normal endobronchial epithelial cells. According to the previous study, the success rate of establishment of surgical sample derived LCO models cultured for >10 passages were 7~17% [4,5].

Clinically, many patients who have advanced disease are not eligible for the radical surgery, therefore, it is difficult to collect enough tissue used for successful LCO development in metastatic/recurrent lung cancer patients. In many patients with advanced-stage or recurrent lung cancers who require drug therapy, bronchoscopy, especially endobronchial ultrasound-guided transbronchial needle aspiration (EBUS-TBNA) is usually used for diagnosis and staging as a standard clinical procedure. Data on establishing PDO and PDX from biopsy samples, including EBUS-TBNA, is very limited in lung cancer. Regarding to the biopsy sample-derived LCO, the initiation rate was reported as 50% (4/8 samples) but at only 7-days post processing and these cases were not validated whether they were truly LCO or not [6]. There is no previous report regarding EBUS-LCO culture stability and long-term passaging.

In our previous report, we successfully established lung cancer PDX models in 42.1% (8/19 cases) using EBUS-TBNA samples with rapid on-site cytological evaluation [7]. These EBUS-PDXs are all derived from lymph node metastasis, and patients are indicated to drug therapy. We have also experienced that xenograft derived organoid (XDO) were successfully established better than PDO [2]. Expansion of lung cancer cells as PDX can lead to better

establishment of LCO. In addition, xenograft culture can avoid normal air way cell expansion.

In this study, we explored xenograft-derived organoids (XDO) using lung cancer EBUS biopsy-based patient-derived xenografts (EBUS-PDX) as a strategy to improve the establishment of EBUS biopsy-based LCOs. We precisely validated pathological and genetical findings of established organoid models, and assessed drug sensitivity comparing the corresponding patient response.

Methods

A total of 16 cryopreserved EBUS-PDX tumors were engrafted subcutaneously in nonobese severe combined immune deficient gamma (NSG) mice. Clinical data of EBUS-PDX tumors were collected according to the review ethical board of UHN (11-0109-CE). PDX tumors reaching ~1000mm^3 were resected and digested to single cells using collagenase II. We extracted mouse derived cells in PDX tumor by labeling the mouse cells with H2K antibody and magnetic separation. Tumor cells were embedded in matrigel and cultured in M27 organoid culture medium developed at our institution.

XDOs were passaged more than 10 times and assessed histologically. We defined the "stable establishment" of XDO as (i) passage number ≥10, (ii) no mouse cell contamination by flowcytometry, (iii) retained pathologic features of the origin PDX tumor. For pathological assessment, formalin-fixed paraffin embedded block was prepared in XDO and PDX tumor. Mouse cell contamination in the established XDO was checked in flowcytometry by labelling mouse cells and human cells with H2K and EpCAM, respectively. DNA of PDX and XDO were extracted for checking the druggable mutations by sanger sequencing. Drug sensitivity assays were performed using XDOs of early passage and that met these stability criteria. Drug resistance model to target therapy was generated by chronic exposure in dose escalation manner. All statistical analysis was performed in GraphPad Prism 9 or EZR.

Results

All 16 cryopreserved EBUS-PDX tumors including nine adenocarcinoma (ADC), two squamous cell carcinoma (SQ) and three small cell lung cancer (SCLC), and each one of large cell neuroendocrine carcinoma (LCNEC) and large cell carcinoma, successfully achieved the 1000mm^3 threshold in NSG mice in a median period of 8.5 (2.9-14.5) weeks. We successfully established 12 stable EBUS-XDOs in 75% (12/16) success rate; six out of nine (67%) ADC, two (100%) SQ, three (100%) SCLC, and one (100%) LCNEC. Two ADC and a large cell XDO stopped growing in less than 10 passages, and remain one ADC was identified 100% of mouse cell outgrowth.

EBUS-XDOs and origin PDXs showed similar histological appearances in the H&E staining and maintained the expression of TTF-1 in ADC, p40 in SCC and neuroendocrine markers (chromogranin A, synaptophysin and CD56) in SCLC and LCNEC models (**Figure1**). As an

example, XDO4370 derived from a stage IIIB ADC showed maldistributed nuclei with intracytoplasmic mucinous lesion that also observed in original PDX4370 tumor. A LCNEC tumor, which was diagnosed as large cell lung cancer by EBUS-TBNA specimen in clinical setting, revealed to be positive staining of neuroendocrine markers in XDO and PDX. In genomic analysis for druggable mutations in lung cancer, KRAS G12C mutation was detected in two ADC models, both of XDO and PDX.

A SCLC EBUS-XDO demonstrated a response to chemotherapy consistent with that observed in the patient (**Figure 2**). On the other hand, an ADC XDO, whose patient was treated by chemotherapy and showed stable disease clinically, showed higher IC_{50} value than sensitive SCLC model.

An ADC XDO model harboring KRAS G12C mutation was sensitive to approved KRAS G12C inhibitors, sotorasib and adagrasive, in drug sensitivity assay (**Figure 3**). Killing assay also showed potent suppression of cell growth by presence of sotorasib and adagrasive for four weeks. In immunoblotting, down streaming signals, phospho-Erk (pErk) and pAkt, were suppressed in were suppressed in dose dependent manner by sotorasib in sensitive model, but not in resistance model. In addition, we successfully generated acquired resistant clones to KRAS G12C inhibitors by chronic exposure, and these models showed more than 100 times higher IC_{50} values to sotorasib and adagrasib than parental sensitive clone.

Conclusions and Knowledge Translation

We could establish LCOs using an XDO approach with a high success rate. XDO recapitulated the histological findings of PDX tumor. XDO can be a good option to generate stable patient derived LCO model using biopsy samples. Our data showed that in vitro drug sensitivity in XDO was correlated to clinical response in patient treated with systemic therapy. XDO is also available as *in vitro* model for the insight to acquired resistance mechanism to targeted therapy. The established EBUS-LCOs are being prepared for registration to the PMC living biobank. Thus, established models in this project are expected to contribute to lung cancer researchers in UHN laboratories.

Figures

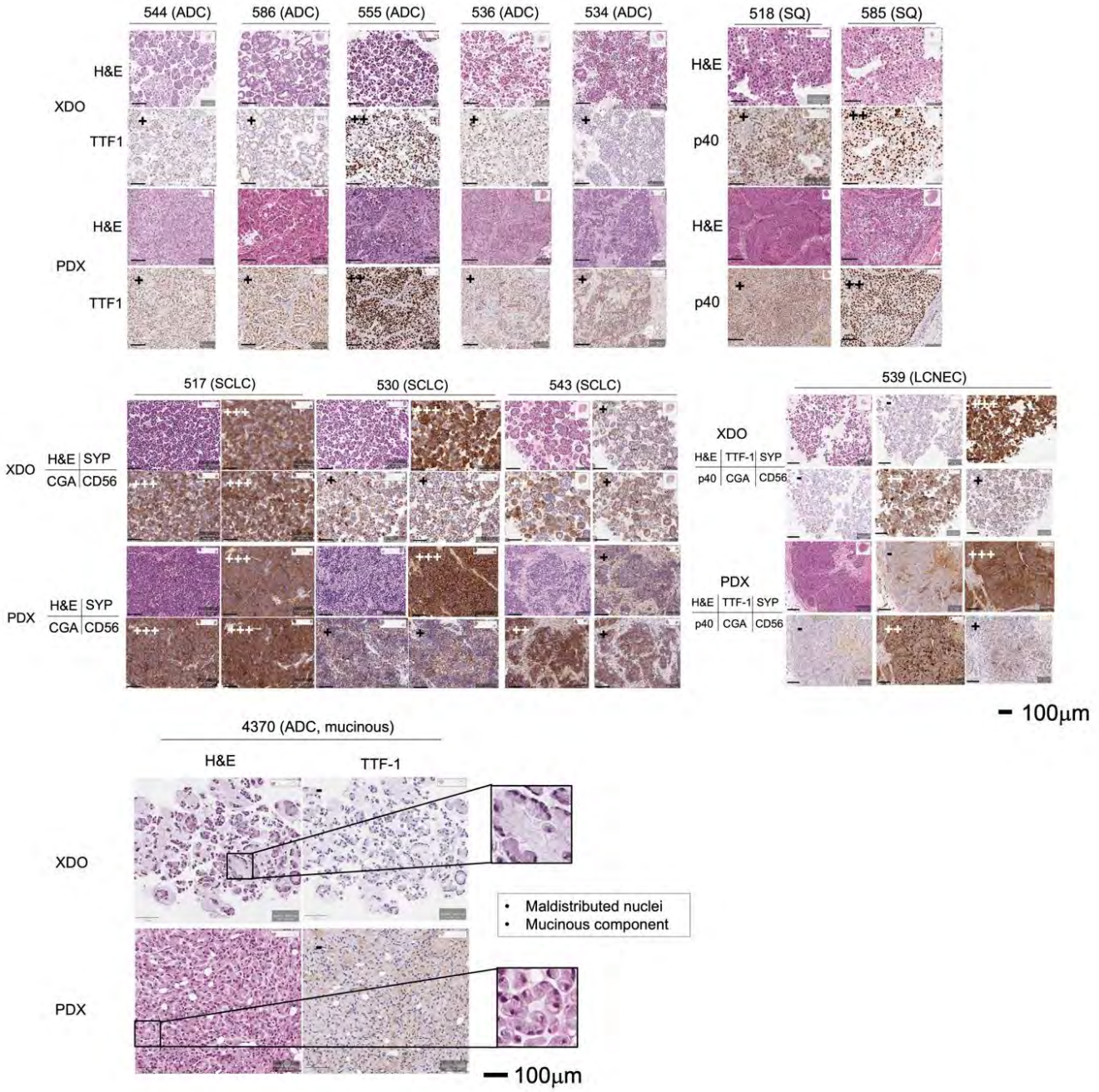

Figure 1. Pathological findings of established stable EBUS-XDO models.

TTF-1: thyroid transcription factor-1, SYP: synaptophysin, CGA: chromogranin A,

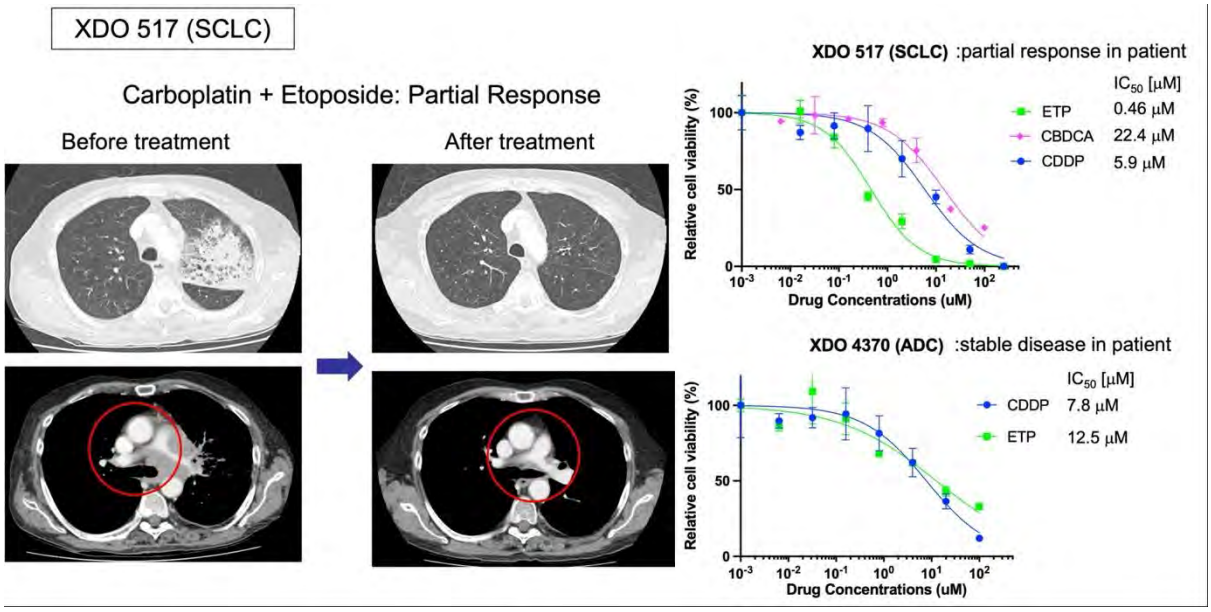

Figure 2. Clinical drug response in patient and in vitro drug sensitivity of XDO

CDDP: cisplatin, ETP: etoposide, CBDCA: carboplatin

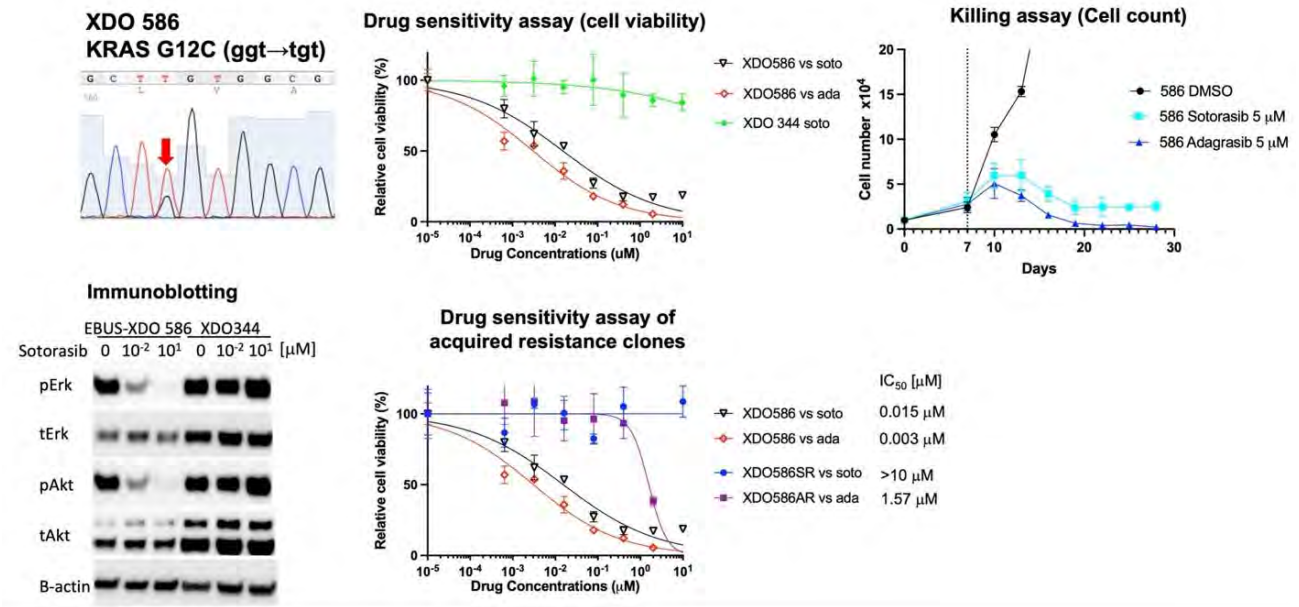

Figure 3. XDO as a preclinical model for drug sensitivity assay using targeted therapy and insight to the acquired resistance mechanism

SR: sotorasib resistance, AR: adagrasib resistance

References

1. Pauli C, Hopkins BD, Prandi D, et al. Personalized In Vitro and In Vivo Cancer Models to Guide Precision Medicine. *Cancer Discov*. May 2017;7(5):462-477. doi:10.1158/2159-8290.Cd-16-1154

2. Shi R, Radulovich N, Ng C, et al. Organoid Cultures as Preclinical Models of Non-Small Cell Lung Cancer. *Clin Cancer Res*. Mar 1 2020;26(5):1162-1174. doi:10.1158/1078-0432.Ccr-19-1376

3. John T, Kohler D, Pintilie M, et al. The ability to form primary tumor xenografts is predictive of increased risk of disease recurrence in early-stage non-small cell lung cancer. *Clin Cancer Res*. Jan 1 2011;17(1):134-41. doi:10.1158/1078-0432.Ccr-10-2224

4. Dijkstra KK, Monkhorst K, Schipper LJ, et al. Challenges in Establishing Pure Lung Cancer Organoids Limit Their Utility for Personalized Medicine. *Cell Rep*. May 5 2020;31(5):107588. doi:10.1016/j.celrep.2020.107588

5. Yokota E, Iwai M, Yukawa T, et al. Clinical application of a lung cancer organoid (tumoroid) culture system. *NPJ Precis Oncol*. Apr 12 2021;5(1):29. doi:10.1038/s41698-021-00166-3

6. Hu Y, Sui X, Song F, et al. Lung cancer organoids analyzed on microwell arrays predict drug responses of patients within a week. *Nat Commun*. May 10 2021;12(1):2581. doi:10.1038/s41467-021-22676-1

7. Nakajima T, Geddie W, Anayama T, et al. Patient-derived tumor xenograft models established from samples obtained by endobronchial ultrasound-guided transbronchial needle aspiration. *Lung Cancer*. Aug 2015;89(2):110-4. doi:10.1016/j.lungcan.2015.05.018

INTEGRATIVE PHOSPHOPROTEOMIC ANALYSIS REVEALS HUMAN THORACIC AORTIC ANEURYSMS DIFFER BY ANATOMIC SEGMENT: CONVENTIONAL & MACHINE LEARNING ANALYSIS

Malak Elbatarny (SSTP)[1,2], Uros Kuzmanov[2,4], Daniella Eliathamby[3], Vivian Chu[4], Rashmi Nedadur[2,4], Omar Hamed[1], Meghan McFadden[5], Raymond Kim[6], Craig Simmons[3], Jennifer CY Chung[1], Bo Wang[4], Maral Ouzounian[1], Anthony O Gramolini[2,5]

[1]Division of Cardiovascular Surgery, University of Toronto, Toronto, ON Canada
[2]Department of Physiology, University of Toronto, Toronto, ON Canada
[3]Department of Biomedical and Molecular Engineering, University of Toronto, Toronto, ON Canada
[4]Vector Institute of Artificial Intelligence, University of Toronto, Toronto, ON Canada
[5]Translational Biology & Engineering Program, Ted Rogers Centre, University of Toronto, Toronto, ON Canada
[6]Cardiac Genome Clinic, Hospital for Sick Children, Toronto, ON Canada

BACKGROUND: Acute Type A Aortic Dissection (ATAD) is a surgical emergency and ATAD mortality remains high (15-25%) in the modern era.[1–3] Although screening tools have improved thoracic aortic aneurysm disease (TAAD) detection, many small aneurysms do not progress, yet half of dissections occur at sub-surgical thresholds.[4] There is therefore an urgent need for patient-specific accurate prognostication tools to guide management. Natural history of TAAD varies considerably by aortic anatomic segment, and as a result root, ascending, arch, and descending aneurysms have distinct treatment thresholds and predicted outcomes. [5–8] Root aneurysms in particular have been identified to be particularly malignant relative to those in other thoracic aortic segments.[6] It is possible that TAAD from different aortic segments have distinct biochemical phenotypes, however mechanisms which underpin aortic segmental differences, if any, are unknown.

Mass spectrometry (MS) proteomics is a highly sensitive and precise tool for tissue phenotypic profiling with several important advantages: (1) protein profile is much closer to true tissue phenotype than DNA or RNA-based profiling, (2) high-throughput MS proteomics can facilitate resolution of subtle phenotypic differences even within the same organ,[9] and (3) MS provides the ability to examine the profile of post-translational modifications to proteins (e.g. phosphorylation) which can drastically alter protein function and offer yet another step closer to true tissue phenotype beyond even the protein-level.[10,11]

Within thoracic aneurysm, several studies have sought to characterize aortic tissue biochemical profile using MS proteomics, but generally lacked the granularity to elucidate differences in disease phenotype by anatomic segment.[12–19] Additionally, attempts to characterize aortic post-translational modifications in human aortic tissues have been performed only on limited sample numbers (N = 5 - 17) and only of subpopulations of TAAD or non-aneurysm pathologies.[12,15,20] Nevertheless, certain underlying causes of TAAD are known to preferentially affect isolated aortic segments.[21] Furthermore, animal studies have indicated thoracic aortic and abdominal tissues to have different histological characteristics,[22] however comparisons within thoracic aortic segments are lacking. In the context of human TAAD, one study identified distinctions among normal root and ascending aortic tissue biomechanic properties[23] although the number of donors included was limited, and in-depth biochemical characterization was outside of the study scope.

We therefore sought to perform comprehensive, high-throughput MS proteomics and phosphoproteomics to profile the largest cohort of human aortic tissues to date with high depth of coverage. We aimed to use this approach to resolve subtle differences in tissue biochemical profiles among root, ascending, arch, and descending thoracic aneurysms, which may explain the differences in natural history observed clinically among these phenotypes.

OBJECTIVES

(1) Develop a customized MS proteomic and phosphoproteomic protocol to improve proteomic depth of coverage in aortic tissues, improve characterization of cellular proteins, and overcome challenges associated with vascular tissue proteomics (high abundance extracellular and glycoproteomic content).
(2) Determine whether proteomic and phosphoproteomic profiles of thoracic aortic samples differ significantly by anatomic segment (among all pathological states and specifically in the context of aneurysm) using conventional statistics and machine learning analyses.
(3) Characterize functional biological consequences of proteomic and phosphoproteomic profile differences in aortic segments and validate selected significantly different proteins between aortic segments in the context of aneurysm.

METHODS & RESULTS: High-throughput deep proteomic & phosphoproteomic profiling of human thoracic aorta - Aortic tissue samples were collected prospectively (N=149) from 82 unique individuals incorporating root, ascending, arch, and descending thoracic aortic anatomic segments (**Fig 1A)**. Samples from multiple segments of included patients acted as within-patient controls. An optimized sample preparation workflow was developed to efficiently target biologically-active cellular proteins and overcome interference with high-abundance extracellular matrix proteins. This entailed urea-based tissue lysis/polytron homogenization, customized protein library generation, and Data Independent Acquisition (**Fig 1B**). A customized phosphoproteomic protocol was also developed involving two-step magnetic bead enrichment (combined Fe/Zr followed by TiO_2 enrichment and Data Dependent Acquisition) to detect phosphorylated peptides and minimize interference with high abundance, negatively-charged vascular tissue glycopeptides (**Fig 1C**). Using these technical modifications we achieved detection of 8339 unique proteins, and quantified 5660 to a minimum of 3 valid values across all samples (N=149). This represents a major increase in coverage (by several thousand proteins) compared to published vascular literature.[13,15,17] Phosphoproteomic analysis of N=139 samples further detected 1870 phosphoproteomic sites, of which 1036 could be quantified across all samples.

Deep proteomic and phosphoproteomic profiling reveals phenotypic differences among human aneurysms from different aortic segments - We next investigated whether biochemical profiles of aortic tissues differed by anatomic segment. Significantly different proteins ($p<0.05$) were indeed identified among all anatomic segmental comparisons in greatest quantities between: root vs ascending (715 proteins), root vs descending (1018 proteins), and ascending vs descending (1027 proteins) across the entire cohort (**Fig 2A**). Considering only those with aneurysm, **Fig 2B-D**, demonstrates the distribution of significantly different proteins by aortic segment. To determine whether samples clustered based on proteomic profile in accordance with differences in anatomic segment, we also performed unsupervised machine learning analyses including principal component analysis (PCA, **Fig 2E-J**) as well as t-distributed Stochastic Neighbour Embedding (t-SNE). Both PCA and t-SNE found aneurysm samples clustered distinctly based on proteomic profile with greatest separation among root vs descending as well as descending vs ascending samples (**Fig 2E-J**).

Clinical evidence suggests that root TAAD may be more malignant than ascending,[6] so we therefore performed additional phosphoproteomic comparison of root vs ascending tissues to determine whether differential phosphorylation events could explain differences in natural history among these phenotypes. We identified 120 significantly different phosphorylation sites (**Fig 2K**) which differentiated root vs aortic tissues including two sites of cytoskeletal regulatory proteins SYNPO2-Ser1107 and CTTN-Ser381. Importantly, SYNPO2 and CTTN were not significant at the proteomic level, suggesting true phosphorylation-specific regulatory changes.

Functional enrichment analyses demonstrate cellular adhesion, cytoskeletal regulation and mitochondrial metabolism differ among root vs ascending segments - Functional enrichment analyses were used to characterize the functions associated with significantly different proteins and phosphorylation sites among aortic segments (**Fig 1D**). At the proteomic level, Gene

Ontology terms identified cellular binding and metabolite conversion processes to be particularly relevant to root vs ascending segmental differences as well as cytoskeletal regulation by Rho-GTPase to root vs descending profiles. Kinase Enrichment Analyses predicted CSNK2A1 to be involved in regulating aortic segmental differences. This serine/threonine protein kinase complex associated with cell cycle progression through cytoskeletal regulation, as well as apoptosis, and transcription.[24–28] In Transcription Factor Enrichment Analysis of aortic segments two key transcription factors were identified in regulating aortic anatomic segmental differences: E2F1, a notable metabolic regulator [29] and TP53 which is known to regulate cell cycle progression.

We also performed integrative phosphoproteomic and proteomic Gene Set Enrichment Analysis in accordance with our previously established methods [11] to characterize gene sets with significant differences among root and ascending tissues of all pathological states. We therefore identified cellular binding, developmental processes and cytoskeletal organization gene sets to be negatively enriched while mitochondrial energetic gene sets to be positively enriched among root tissues in comparison to ascending.

Cell binding protein, MFAP4 is elevated in ascending vs other segment aneurysms - We identified MFAP4, a cellular binding protein and mediator of cell-matrix interactions,[12,30–32] to be significantly different among aneurysm samples of different aortic segments (**Fig 2B-D**). This protein had been previously identified in Marfan-associated TAAD, detected in blood, and therefore proposed as a potential biomarker for TAAD.[12] It however has only been associated with clinical risk in the distal, rather than proximal aorta, and given our findings of differential expression in aortic segments, we sought to validate this target further (**Fig 1E**) as a possible explanation of why serum MFAP4 levels correlated with distal but not proximal aortic events.[12] Immunoblotting identified a non-significant signal towards decreasing levels of MFAP4 expression in ascending, root, and descending aneurysm tissues in accordance with our MS findings (**Fig 3A-B**). We hypothesized that expression differences could be a cell-specific process. We therefore used immunofluorescence to localize MFAP4 and indeed found vascular smooth muscle cell-specific localization in human aneurysm tissues (**Fig 3C**). Immunofluorescence of the vascular smooth muscle-rich aortic tunica media comparing MFAP4 expression by aortic segment indeed identified significantly different expression in root vs ascending and ascending vs descending comparisons in accordance to MS proteomic findings (**Fig 3D-E**). Ascending aneurysms featured high MFAP4 expression which was significantly greater than root and descending aneurysm tissues (**Figure 3D-E**). MFAP4 expression was low among both root and descending aortic aneurysms and not significantly different between one another (**Fig 3D-E**).

CONCLUSIONS: We performed extensive proteomic and phosphoproteomic profiling of thoracic aortic tissue using modified protein extraction and enrichment techniques on the largest known cohort of human samples. We achieved significantly improved depth of coverage in comparison to existing literature and thus were able to perform the first comparison of anatomic segments within human thoracic aortic aneurysm patients. We identified significant differences among thoracic anatomic segments in cellular binding, cytoskeletal organization, and mitochondrial regulatory pathways. Of these, phosphorylation-specific events were identified pointing to the potential importance of post-translational modification profiling to characterizing aneurysm phenotypes. Validation of segment differences using immunoblotting and immunofluorescence was performed for a previously proposed aneurysm biomarker, offering an explanation for observed inconsistencies in prognostication by aortic segment. We hereby demonstrate the importance of anatomic segment-specific biochemical profiling which may constitute an important caveat to potential circulating biomarkers to TAAD aneurysm progression. Further analysis to pinpoint exact mechanistic differences between aneurysms of different aortic segments and to elucidate links to clinical outcomes is required. Nevertheless, we provide evidence that thoracic aneurysms of different anatomic segments indeed have different biochemical profiles which may explain differences in natural history and could potentially be leveraged for patient-specific prognostication and management.

Figure 1. Sample Details and Study Design.

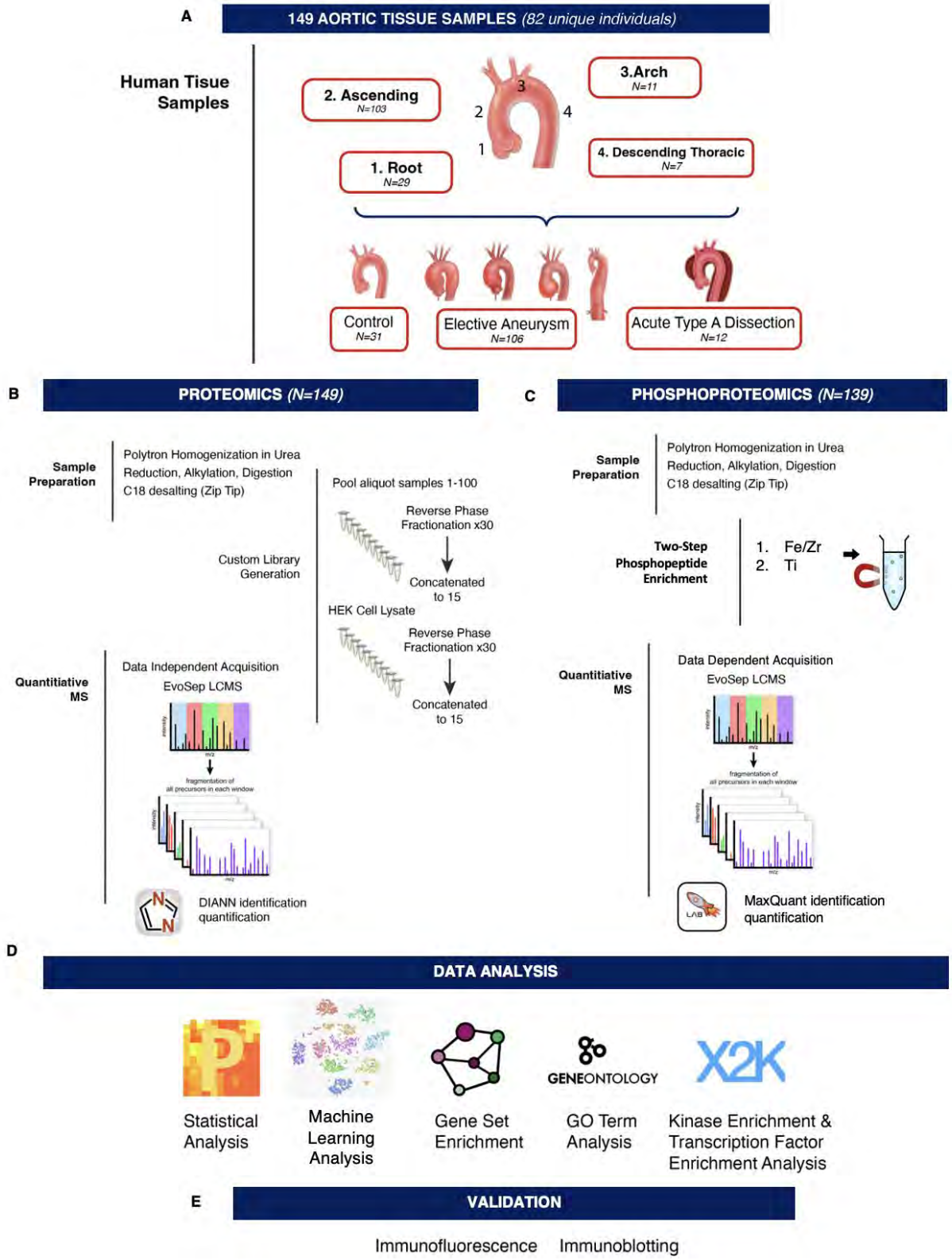

Figure 2. Proteomic and Phosphoproteomic Profiles of Analyzed Samples

A. Number of Significantly Different Proteins in Each Segmental Comparison (All Samples)

Segments Compared	Descending	Arch	Ascending
Root	1018	636	715
Ascending	1027	574	
Arch	456		

Proteomic Profile of Aortic Aneurysms by Aortic Segment

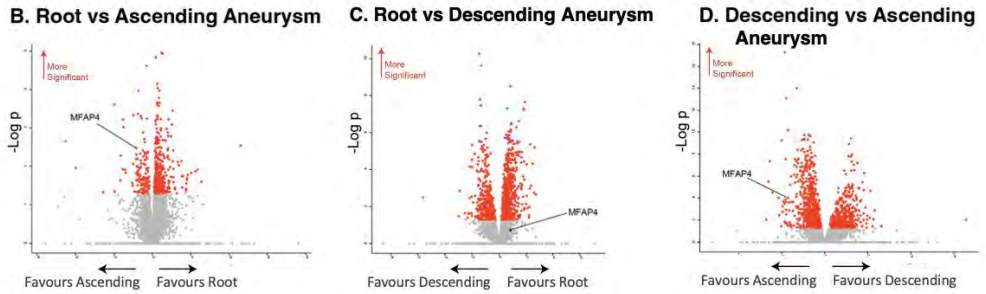

Principal Component Analysis by Aortic Segment

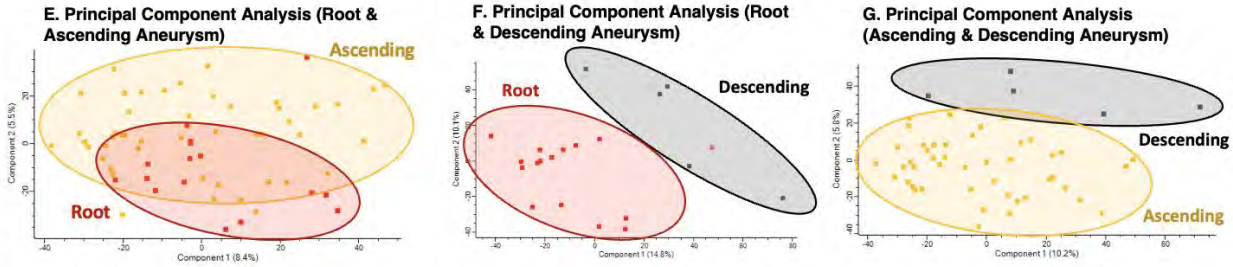

Phosphoproteomic Analysis by Aortic Segment

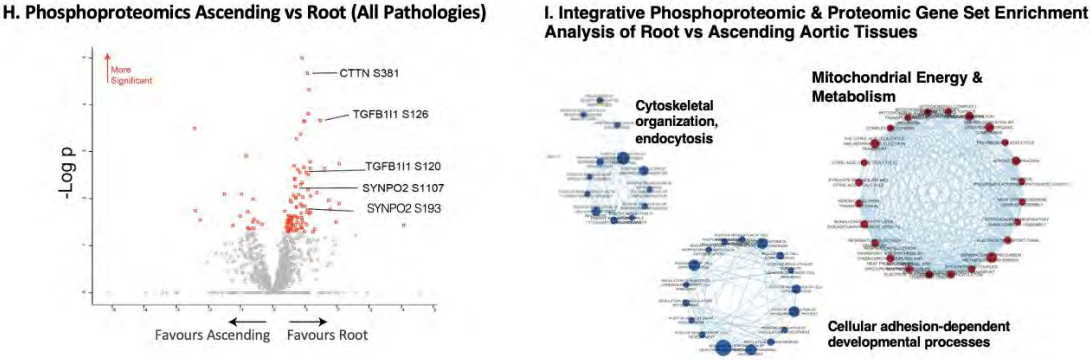

Figure 3. Cellular Binding Protein MFAP4 is Increased in Ascending Aneurysm Compared to Root and Descending Aneurysms

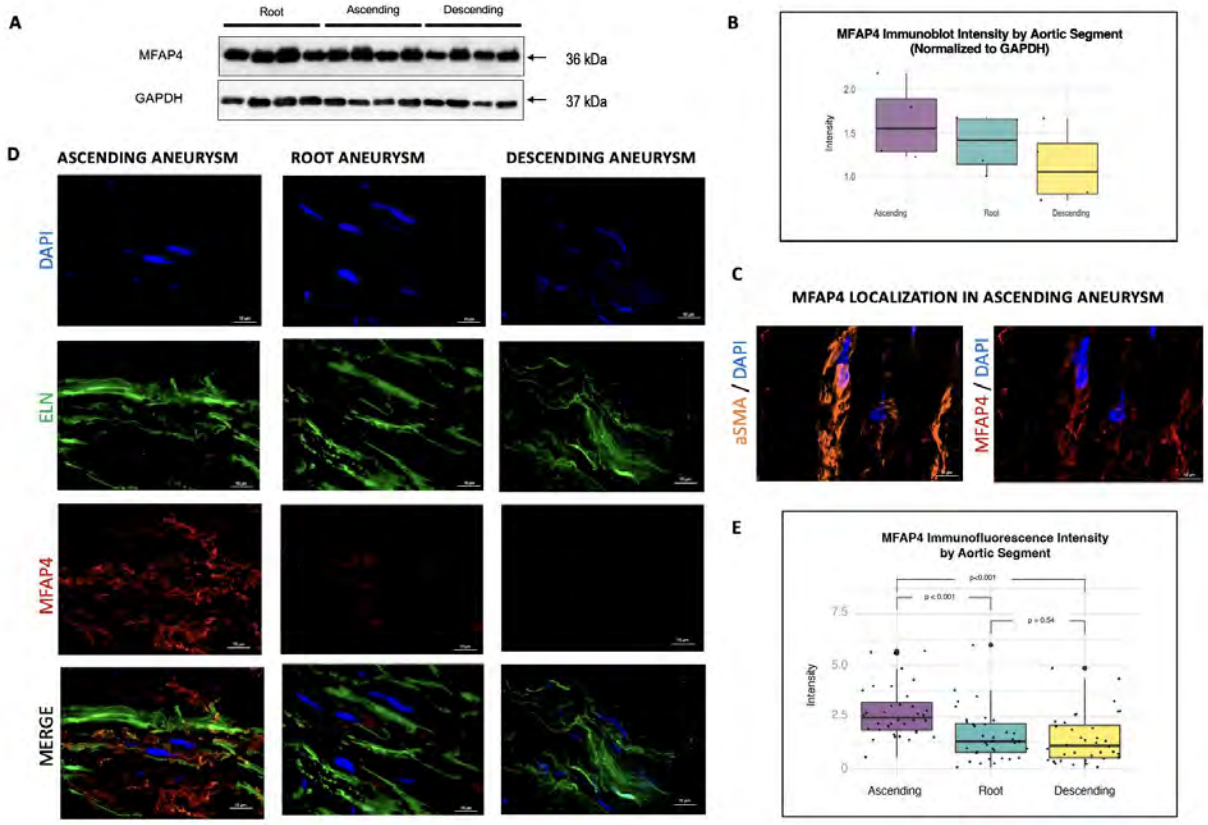

Figure Legends

Figure 1. Sample Details and Study Design. A) Breakdown of samples included by anatomic segment and pathological status. Customized workflow for B) proteomic and C) phosphoproteomic sample data acquisition. D) Proteomic and Phosphoproteomic data analysis methods including conventional statistics and machine learning analyses. E) Validation of proteomic targets using Immunofluorescence and Immunoblotting. MS = mass spectrometry, LCMS = liquid chromatography MS, GO = Gene Ontology.

Figure 2. Proteomic and Phosphoproteomic Profiles of Analyzed Samples. A) Table indicating the number of significantly different proteins between each segment regardless of sample pathological status. B-D) Volcano plots demonstrating distribution in proteomic profile by aortic segment among aneurysm samples only. MFAP4 (Microfibrillar Associated Protein 4) which was selected for further validation is highlighted. Proteins in red represent those with significantly different expression ($p<0.05$). E-G) Principal Component Analysis of aneurysm samples demonstrate distinct clustering by aortic segment. H) Volcano plot demonstrating distribution in phosphorylation sites in root vs ascending samples pooled across all pathological states. Phosphorylation sites related to cytoskeletal regulation are highlighted. I) Integrative proteomic and phosphoproteomic gene set enrichment analysis of root vs ascending samples. Red indicates positive enrichment and blue, negative enrichment in root compared to ascending.

Figure 3. Cellular Binding Protein MFAP4 is Increased in Ascending Aneurysm Compared to Root and Descending Aneurysms. A) Immunoblotting MFAP4 for N=4 human aneurysm samples per aortic segment (upper) and corresponding GAPDH (lower). B) MFAP4 intensities normalized by GAPDH intensity trend towards increased ascending expression but do not reach statistical significance. Root vs Ascending $p=0.206$, Ascending vs Descending $p=0.079$, Root vs Descending $p=0.196$. C) Colocalization of MFAP4 with aSMA suggests MFAP4 is localized to vascular smooth muscle cells in human ascending aneurysm. D) Human aortic aneurysm samples (representative images from N=12: 4 ascending, 4 root, 4 descending patients) stained for MFAP4 (red) and DAPI (blue). Elastin (ELN) autofluorescence (green) is also shown for reference. E) Intensity measurements for MFAP4 for each aortic segment derived from 9 fields of view per sample show significantly increased MFAP4 expression in ascending aneurysm compared to root and descending.

References

1. Evangelista A, Isselbacher EM, Bossone E, et al. Insights from the international registry of acute aortic dissection: A 20-year experience of collaborative clinical research. *Circulation*. 2018;137(17):1846-1860. doi:10.1161/CIRCULATIONAHA.117.031264
2. Ghoreishi M, Sundt TM, Cameron DE, et al. Factors associated with acute stroke after type A aortic dissection repair: An analysis of the Society of Thoracic Surgeons National Adult Cardiac Surgery Database. *Journal of Thoracic and Cardiovascular Surgery*. 2020;159(6):2143-2154.e3. doi:10.1016/j.jtcvs.2019.06.016
3. Czerny M, Schoenhoff F, Etz C, et al. The Impact of Pre-Operative Malperfusion on Outcome in Acute Type A Aortic Dissection: Results From the GERAADA Registry. *J Am Coll Cardiol*. 2015;65(24):2628-2635. doi:10.1016/j.jacc.2015.04.030
4. Pape LA, Tsai TT, Isselbacher EM, et al. Aortic diameter ≥5.5 cm is not a good predictor of type A aortic dissection: Observations from the International Registry of Acute Aortic Dissection (IRAD). *Circulation*. 2007;116(10):1120-1127. doi:10.1161/CIRCULATIONAHA.107.702720
5. Isselbacher EM, Preventza O, Black JH, et al. 2022 ACC/AHA Guideline for the Diagnosis and Management of Aortic Disease: A Report of the American Heart Association/American College of Cardiology Joint Committee on Clinical Practice Guidelines. *Circulation*. Published online December 13, 2022. doi:10.1161/cir.0000000000001106
6. Kalogerakos PD, Zafar MA, Li Y, et al. Root dilatation is more malignant than ascending aortic dilation. *J Am Heart Assoc*. 2021;10(14). doi:10.1161/JAHA.120.020645
7. Erbel R, Aboyans V, Boileau C, et al. 2014 ESC guidelines on the diagnosis and treatment of aortic diseases. *Russian Journal of Cardiology*. 2015;123(7):7-72. doi:10.15829/1560-4071-2015-07-7-72
8. Hiratzka LF, Bakris GL, Beckman JA, et al. 2010 ACCF/AHA/AATS/ACR/ASA/SCA/SCAI/SIR/STS/SVM guidelines for the diagnosis and management of patients with Thoracic Aortic Disease: a report of the American College of Cardiology Foundation/American Heart Association Task Force on Practice Guidelines, A. *Circulation*. 2010;121(13):e266-369. doi:10.1161/CIR.0b013e3181d4739e
9. Mertins P, Yang F, Liu T, et al. Ischemia in tumors induces early and sustained phosphorylation changes in stress kinase pathways but does not affect global protein levels. *Molecular and Cellular Proteomics*. 2014;13(7):1690-1704. doi:10.1074/mcp.M113.036392
10. Kuzmanov U, Guo H, Buchsbaum D, et al. Global phosphoproteomic profiling reveals perturbed signaling in a mouse model of dilated cardiomyopathy. *Proc Natl Acad Sci U S A*. 2016;113(44):12592-12597. doi:10.1073/pnas.1606444113
11. Kuzmanov U, Wang EY, Vanderlaan R, et al. Integrative Phosphoproteomic Profiling of Clinical Samples, Animal and Organ-on-a-Chip Models: Mapping Cardiac Fibrosis. *Nat Biomed Eng*. 2020;4:889–900.
12. Yin X, Wanga S, Fellows AL, et al. Glycoproteomic analysis of the aortic extracellular matrix in Marfan patients. *Arterioscler Thromb Vasc Biol*. 2019;39(9):1859-1873. doi:10.1161/ATVBAHA.118.312175
13. Maleki S, Kjellqvist S, Paloschi V, et al. Mesenchymal state of intimal cells may explain higher propensity to ascending aortic aneurysm in bicuspid aortic valves. *Sci Rep*. 2016;6(June):1-16. doi:10.1038/srep35712
14. Martinez-Pinna R, Burillo E, Madrigal-Matute J, et al. Label-free proteomic analysis of red blood cell membrane fractions from abdominal aortic aneurysm patients. *Proteomics Clin Appl*. 2014;8(7-8):626-630. doi:10.1002/prca.201400035

15. Skeffington KL, Bond AR, Abdul-Ghani S, et al. Bicuspid Aortic Valve Alters Aortic Protein Expression Profile in Neonatal Coarctation Patients. *J Clin Med*. 2019;8(4):517. doi:10.3390/jcm8040517
16. Cebull HL, Rayz VL, Goergen CJ. Recent Advances in Biomechanical Characterization of Thoracic Aortic Aneurysms. *Front Cardiovasc Med*. 2020;7(May):1-11. doi:10.3389/fcvm.2020.00075
17. David M Herrington, MD, MHS1,*, Chunhong Mao, PhD2, Sarah J Parker, PhD3, Zongming Fu, PhD4, Guoqiang Yu, PhD5, Lulu Chen, MS5, Vidya Venkatraman, MS3, Yi Fu5, Yizhi Wang, MS5, Timothy D Howard, PhD6, Goo Jun, PhD7, Caroline F Zhao1, Yongmei Liu, PhD8, Ge P. Proteomic Architecture of Human Coronary and Aortic Atherosclerosis. *Circulation*. 2018;47(3):549-562. doi:10.1097/CCM.0b013e31823da96d.Hydrogen
18. Abudupataer M, Zhu S, Yan S, et al. Aorta smooth muscle-on-a-chip reveals impaired mitochondrial dynamics as a therapeutic target for aortic aneurysm in bicuspid aortic valve disease. *Elife*. 2021;10. doi:10.7554/eLife.69310
19. Saddic L, Orosco A, Guo D, et al. Proteomic analysis of descending thoracic aorta identifies unique and universal signatures of aneurysm and dissection. *JVS Vasc Sci*. 2022;3:85-181. doi:10.1016/j.jvssci.2022.01.001
20. Pan L, Lin Z, Tang X, et al. S-Nitrosylation of Plastin-3 Exacerbates Thoracic Aortic Dissection Formation via Endothelial Barrier Dysfunction. *Arterioscler Thromb Vasc Biol*. 2020;40(1):175-188. doi:10.1161/ATVBAHA.119.313440
21. Loeys BL, Dietz HC, Braverman AC, et al. The revised Ghent nosology for the Marfan syndrome. *J Med Genet*. 2010;47(7):476-485. doi:10.1136/jmg.2009.072785
22. Tonar Z, Kubíková T, Prior C, et al. Segmental and age differences in the elastin network, collagen, and smooth muscle phenotype in the tunica media of the porcine aorta. *Annals of Anatomy*. 2015;201:79-90. doi:10.1016/j.aanat.2015.05.005
23. Xuan Y, Wisneski AD, Wang Z, et al. Regional biomechanical and failure properties of healthy human ascending aorta and root. *J Mech Behav Biomed Mater*. 2021;123. doi:10.1016/j.jmbbm.2021.104705
24. St-Denis NA, Derksen DR, Litchfield DW. Evidence for Regulation of Mitotic Progression through Temporal Phosphorylation and Dephosphorylation of CK2α. *Mol Cell Biol*. 2009;29(8):2068-2081. doi:10.1128/mcb.01563-08
25. Keller DM, Zeng X, Wang Y, et al. *A DNA Damage-Induced P53 Serine 392 Kinase Complex Contains CK2, HSpt16, and SSRP1 as Phosphorylation and Acetylation (Shieh et al These Modifications Allow Rapid Modulation*. Vol 7. Lakin and Jackson; 2001.
26. Sayed M, Pelech S, Wong C, Marotta A, Salh B. *Protein Kinase CK2 Is Involved in G2 Arrest and Apoptosis Following Spindle Damage in Epithelial Cells*.; 2001. www.nature.com/onc
27. Dominguez I, Sonenshein GE, Seldin DC. CK2 and its role in Wnt and NF-κB signaling: Linking development and cancer. *Cellular and Molecular Life Sciences*. 2009;66(11-12):1850-1857. doi:10.1007/s00018-009-9153-z
28. St-Denis NA, Litchfield DW. From birth to death: The role of protein kinase CK2 in the regulation of cell proliferation and survival. *Cellular and Molecular Life Sciences*. 2009;66(11-12):1817-1829. doi:10.1007/s00018-009-9150-2
29. Denechaud PD, Fajas L, Giralt A. E2F1, a novel regulator of metabolism. *Front Endocrinol (Lausanne)*. 2017;8(NOV). doi:10.3389/fendo.2017.00311
30. Schlosser A, Pilecki B, Hemstra LE, et al. MFAP4 Promotes Vascular Smooth Muscle Migration, Proliferation and Accelerates Neointima Formation. *Arterioscler Thromb Vasc Biol*. 2016;36(1):122-133. doi:10.1161/ATVBAHA.115.306672

31. Dorn LE, Lawrence W, Petrosino JM, et al. Microfibrillar-Associated Protein 4 Regulates Stress-Induced Cardiac Remodeling. *Circ Res*. 2021;128(6):723-737. doi:10.1161/CIRCRESAHA.120.317146
32. Wulf-Johansson H, Johansson SL, Schlosser A, et al. Localization of microfibrillar-associated protein 4 (MFAP4) in human tissues: Clinical evaluation of serum MFAP4 and its association with various cardiovascular conditions. *PLoS One*. 2013;8(12). doi:10.1371/journal.pone.0082243

THE ROLE OF OPERATING ROOM PROFESSIONS IN SETTING THE TONE FOR TEAMWORK: A CONSTRUCTIVIST GROUNDED THEORY STUDY

Hillary Lia[1,2,3], Melanie Hammond Mobilio[1,4], Frank Rudizcz[2,3,5,6], Carol-anne Moulton[1,2,7]
[1]The Wilson Centre, Toronto General Hospital, University Health Network, Toronto, ON, Canada
[2]Institute of Medical Science, Temerty Faculty of Medicine, University of Toronto, Toronto, ON, Canada
[3]Vector Institute for Artificial Intelligence, Toronto, ON, Canada
[4]Institute of Health Policy, Management and Evaluation, Temerty Faculty of Medicine, University of Toronto, Toronto, ON, Canada
[5]Department of Computer Science, University of Toronto, Toronto, ON, Canada
[6]Faculty of Computer Science, Dalhousie University, Halifax, NS, Canada
[7]Division of General Surgery, University Health Network, Toronto, ON, Canada

Introduction

The tone of the operating room is an under-studied construct that describes the collective and dynamic understanding of team environment, often described as the mood or atmosphere among team members (Leach et al., 2011). Previous studies suggest that the tone of the operating room may promote or deter the quality of communication, cooperation, and teamwork among operating room teams (Leach et al., 2011; Nurok et al., 2010), factors which are known to affect patient safety. The tone is thought to emerge from the interactions of the attending surgeon with other operating room team members. These interactions foster an environment which is either conducive or detrimental to the emergence of high-quality teamwork (Leach et al., 2011). The collective sense of teamwork fostered by a positive tone of the operating room may translate to highly coordinated team responses to changes and unexpected events throughout the operation (Leach et al., 2011). Although tone may be an important aspect of dynamic team functioning, there does not currently exist a framework which clearly defines how tone emerges, how it is experienced by OR team members, and its mechanism for shaping team performance. Our aim is to develop an in-depth framework for understanding how tone emerges in intraoperative teams and the role of tone in team performance.

Methods

18 semi-structured interviews were conducted and analysed using a constructivist grounded theory methodology. To capture a breadth of experiences and perspectives, study participants included surgeons, nurses, anesthetists, and perfusionists with varying subspeciality and levels of experience. A purposive sampling strategy was used where members of the research team suggested initial participants. Following initial interviews, the participants were asked to suggest other staff members for subsequent interviews who may have a unique or nuanced perspective. Interviews were coded by two members of the research team and then reviewed together line-by-line to explore emerging concepts and areas of difference. Coded transcripts were presented and discussed at research team meetings to discuss emerging directions of the coded concepts and categories. Interview data were analysed iteratively to allow for exploration of emerging concepts in subsequent interviews. Data collection and analysis remain ongoing.

Results

The tone of the OR is a dynamic construct that emerges from interpersonal interaction among team members and helps team members understand the social and procedural requirements of the operation.

Role of each profession in constructing tone.

The tone is co-constructed by members of the operating room team, however tone is shaped and experienced differently by each individual, depending on the professional role they occupy. The tone of the operating room is perceived to be set primarily by the attending surgeon. Attending surgeon participants felt that setting the tone was part of their role, one surgeon explains,

> *"I think that surgeon role is being almost like a skipper, you know, of a ship. We need to make sure that this ship is … going well. It's really important when things go bad. Let's say there's major bleeding or something unexpected happens. That's when really the skipper needs to … lead the group. If the skipper is in [a] panic, everyone is gonna be in [a] panic." S1.*

Non-surgeon staff agreed that the surgeon sets the tone and largely agreed that this was due to their position in the hierarchy,

> *"If you look at the hierarchy in the room, you have surgeons and then you have anesthesia and then you have everybody else. Right? So, the anesthetist could certainly set the tone as well ... But to a much lesser degree." P1.*

While anesthetists are not perceived to set the tone, they have a role in modifying the tone. An anesthetist explains,

> *"I change the tone, for sure. … Sometimes I come into a room and it's … just paralytically serious. I will lighten that mood a lot. And sometimes I find it's not serious enough and I will make sure it's more serious and I will make sure that the surgeon understands that I'm concerned about this situation, right? So, I don't try and set the tone, but I try to modify the tone as best I see it." A3.*

Nurses described a different experience with tone. Rather than setting the tone or modifying the tone, they saw themselves in a role to support and set the stage for a productive tone. Based on their demeanor and their degree of preparation for the case, the surgeon may be more likely to set a positive tone. Moreover, during critical phases, nurses saw their role as supporting a focused tone,

> *"It's part of our job to kind of go around the room and say, 'OK this quiet time,' like, 'OK, something's happening right now. Let's all pay attention.' … ' [The surgeon] needs to concentrate right now.'" N3*

Implications of tone for team performance.

The tone, emerging from team interaction, has important implications for team performance by affecting key team constructs. The tone of the OR may facilitate a *shared mental model* by signaling to team members changes in events of the procedure and the relevant change in taskwork and teamwork required as a result,

> *"I think the tone in voice is really important when you hear it … [it] tells us or indicates 'OK, this is something serious we need to just concentrate.'" N2.*

Moreover, the tone facilitates the degree of *psychological safety* experienced dynamically throughout the case which may influence patient safety concerns. A perfusionist explains,

> *"If … there's a positive atmosphere, people will speak up more … If there's something going wrong, or … if they've done something wrong, they'll actually own up to it, right?" P1.*

The experience of working in the operating room is modified by the tone and can affect resilience and wellness,

> *"I think mentally it [tone] helps when you're having those really long days, you're working overtime, you had a really stressful situation, you know, if you lose a patient or that kind of stuff, I think that it helps to feel valued." P3.*

Discussion and Conclusion

Our study of tone illuminates more precisely how tone is experienced in the operating room. The tone is shaped by all members of the operating room team. However, factors of power and hierarchy shape the effect each individual has on the tone and, as a result, how they may experience varying tones in the operating room. Understanding the role of each profession in shaping the tone of the operating room provides a lens through which can understand *how* interpersonal interactions shape teamwork. Using the lens of tone and hierarchy, we may understand why and how the behaviors of each individual shape those of others. For instance, we may start to understand why a surgeons' negative behaviour rapidly changes team tone while the negative behaviour of other staff members has a lesser effect. Similarly, we may help operating staff members understand their role in shaping the tone for teamwork so that they may modify their own attitudes and behaviours to contribute to constructive teamwork.

Our study has outlined key constructs that are shaped by tone: shared mental model, psychological safety and resilience. These are important team constructs which have been studied and found to be central to team performance. By studying tone, we have proposed a lens that can help us understand how to foster these team constructs and how they emerge and change over time. Psychological safety, for example, has traditionally been studied as a static construct, however, there have been calls for study design which acknowledges psychological safety as a dynamic construct (Edmondson & Lei, 2014). We have identified tone as a force which dynamically shapes team constructs in the operating room. As a result, we provide a window with which we can study these constructs, how they interact and how they ultimately impact teamwork quality and patient safety. Continued study of tone in the operating room can provide a deepened understanding of how teams interact in the intraoperative environment to produce environments supportive of safe patient care. We may eventually leverage this knowledge to identify new facets for training that produces intraoperative teams dynamically responsive to changes and challenges for safe and efficient intraoperative care.

References

Edmondson, A. C., & Lei, Z. (2014). Psychological Safety: The History, Renaissance, and Future of an Interpersonal Construct. *Annual Review of Organizational Psychology and Organizational Behavior*, *1*(1), 23–43. https://doi.org/10.1146/annurev-orgpsych-031413-091305

Leach, L. S., Myrtle, R. C., & Weaver, F. A. (2011). Surgical teams: Role perspectives and role dynamics in the operating room. *Health Services Management Research*, *24*(2), 81–90. https://doi.org/10.1258/hsmr.2010.010018

Nurok, M., Lipsitz, S., Satwicz, P., Kelly, A., & Frankel, A. (2010). A Novel Method for Reproducibly Measuring the Effects of Interventions to Improve Emotional Climate, Indices of Team Skills and Communication, and Threat to Patient Outcome in a High-Volume Thoracic Surgery Center. *Archives of Surgery*, *145*(10), 489–495.

Translational Research

CLOSED-LOOP DECODING AND CONTROL OF ATTENTION IN CHILDREN

Nebras M. Warsi[1,2]; Simeon M. Wong[2,3]; Olivia N. Arski[3]; Hrishikesh Suresh[1,2]; Jürgen Germann[4]; Alexandre Boutet[4,5]; Lauren Erdman[6,7,8]; Flavia Venetucci Gouveia[3]; Elizabeth Kerr[9]; Mary Lou Smith[3,10]; Ayako Ochi[11]; Hiroshi Otsubo[11]; Rohit Sharma[11]; Puneet Jain[11]; Shelly Weiss[11]; Elizabeth J. Donner[11]; Andres M. Lozano[4]; O. Carter Snead[11]; Margot J. Taylor[3,12]; George M. Ibrahim[1,2,3]

[1] Division of Neurosurgery, The Hospital for Sick Children, 555 University Ave., Toronto, Ontario, Canada
[2] Institute of Biomedical Engineering, University of Toronto, Toronto, Ontario, Canada
[3] Program in Neuroscience and Mental Health, Hospital for Sick Children, Toronto, Ontario, Canada
[4] Division of Neurosurgery, Toronto Western Hospital, University Health Network, Toronto, Ontario, Canada
[5] Joint Department of Medical Imaging, University of Toronto, Toronto, Ontario, Canada
[6] Vector Institute for Artificial Intelligence, University Health Network, Toronto, Ontario, Canada
[7] Department of Computer Science, University of Toronto, Toronto, Ontario
[8] Center for Computational Medicine, SickKids Research Institute, Toronto, Ontario
[9] Department of Psychology, The Hospital for Sick Children, 555 University Ave., Toronto, Ontario, Canada, M5G 1X8 Department of Psychology, University of Toronto, Toronto, Canada
[10] Department of Psychology, University of Toronto Mississauga, Toronto, Ontario, Canada, M5G 1X8 Department of Psychology, University of Toronto, Toronto, Canada
[11] Division of Neurology, The Hospital for Sick Children, 555 University Ave., Toronto, Ontario, Canada
[12] Diagnostic Imaging, The Hospital for Sick Children, 555 University Ave., Toronto, Ontario, Canada

Attention defines our perceptions[1], memories[2,3], and interactions[4] with the world around us. Selective attention allows us to filter relevant information from distractors while attentional flexibility is critical to adapt behaviour and predicts greater satisfaction in nearly every facet of life[5,6]. Deficits in these core attentional domains are common to several childhood-onset neuropsychiatric disorders including attention deficit/hyperactivity disorder (ADHD)[7,8] and epilepsy[9]. Despite modern, evidence-based, treatment a majority of these children continue to suffer from severe and recurrent lapses in attention that contribute to academic difficulties, psychosocial isolation, and erode future opportunities[9–11]. The limited efficacy of existing psychostimulant medications is thought to relate to their inherent lack of specificity within the brain[12]. An urgent need therefore exists to develop novel targeted neurotherapeutics for attentional disorders in children. While neurostimulation can directly target the provenance of attention deficits within fundamental brain circuits[13], the ability to modulate human attention has remained elusive.

Through study of stereotactic intracranial recordings in children undergoing epilepsy monitoring, we present a first-in-human approach to decode and control attentive behaviour in real-time. Twenty-six children performed a flexible attentional task (Fig. 1a) while tandem eye tracking and intracranial electrophysiologic signals were recorded (Fig. 1b). Given that the electrodes in these children were implanted solely for clinical seizure monitoring, we first assessed the ability of these implantations to sample *in vivo* human attentional circuitry. Across the 26 participants, we show that activity within a convergent set of brain regions was associated with single-trial reaction time (RT) for each subject computed through logistic regression (Fig. 1c). Most commonly, these regions included the frontal, insular, and anterior cingulate cortices (ACC). To determine whether activity within these brain regions could predict lapses in attention, we developed a convolutional neural network (CNN) tailored to each participant's unique brain rhythms (Fig. 1d). Pre-stimulus single-trial periodograms ranging from the 4-60Hz frequencies were computed via Welch's method from selected channels (Fig. 1c) to serve as the training features for the classifier. The test set comprised data obtained during an unseen task session performed on a different day. Between repeated sessions, the CNN accurately and reliably predicted impending lapses in attention indexed by slowed single-trial RT (Figs. 1d, e; aggregate AUC=0.63, $p<10^{-14}$ compared to chance performance). Importantly, these predictions were driven

by elevated theta (4-8Hz) and reduced beta power (12-20Hz) within midline brain regions (Fig. 1f). These activity patterns are characteristic of the resting ADHD brain[14,15], and we show for the first time that lapses in human attention transiently recapitulate an ADHD phenotype.

We next identified a convergent brain network predictive of attentional lapses that independently generalized to several populations (Fig. 1g). Specifically, we examined patterns of large-scale functional connectivity in relation to the predictive brain regions we identified (Fig. 1c). In both a large normative adult connectomic dataset (n=1,000 healthy controls; 57% female; age range: 18-35y; available from http://neuroinformatics.harvard.edu/gsp/)[16] and the study sample (n=12; 67% female; age range: 10-17y), these regions functionally connected to a common circuit we termed the attentional lapse network ($p<0.05$ cluster-corrected, Fig. 1g). The identified network consistently involved the ACC and other nodes of two core human attentional networks, the salience (SN) and default mode networks (DMN, Fig. 1g) [17–19]. Critically, we independently reproduced the attentional lapse network in a public dataset of children with ADHD (n=223; 37% female; age range: 7-18y; available from http://preprocessed-connectomes-project.org/adhd200/)[20], wherein it predicted their clinical symptom severity ($p<0.05$ cluster-corrected, Fig. 1f). Taken together, these results identify a conserved attentional lapse network that may serve as a valuable substrate for human attentional modulation.

We subsequently deployed the CNN to direct real-time closed-loop stimulation of the attentional lapse circuit during an additional task session (Fig. 2a). Closed-loop stimulation denotes a novel form of brain stimulation that activates in response to changes in specific biomarkers[21,22], in contrast to traditional neurostimulation that is continuously active. In our system, brain stimulation was activated in response to classifier-predicted lapses in attention with an aim to restore normal attentive behaviour. We specifically chose the ACC for stimulation due its role in coordinating inter-regional communication between the two main components of the identified circuit, the SN and DMN[17,23]. The effects of stimulation on attention were indexed through eye tracking measures and single-trial RT. These measures were chosen as eye movements are the most intimate correlate of human attentive behaviour[24,25] and slowed RT strongly predicts functional impairment in children with attentional disorders[26].

During closed-loop sessions (n=10), when the CNN classifier predicted a fast RT (attentive), no stimulation was delivered. When a slow RT (attentional lapse) was predicted, the intended stimulation was either i) delivered or ii) randomly withheld to control for the effects of attention on RT. In all subjects, closed-loop stimulation of the identified network during predicted lapses rescued target-directed attention indexed by eye tracking ($p<0.05$ cluster-corrected linear mixed-effects model, Fig. 2b) and improved task performance ($p=0.005$ mixed-effects model Fig. 2b). Separate trials of stimulation during attentive rather than inattentive trials disrupted target-directed attention ($p<0.05$ cluster-corrected linear mixed-effects model) and worsened performance ($p=0.026$ mixed-effects model, Figs 2a, c). These results demonstrate that precisely timed neurostimulation of the attentional lapse network can directly control attentive behaviour in humans.

We subsequently sought to determine the downstream neural effects of closed-loop stimulation. To examine this question, we compared task-related neural responses in the post-stimulus epoch between unstimulated attentional lapse trials and closed-loop trials. Here, we found that lapses in attention were associated with elevated theta (4-8Hz, $p=0.016$ mixed-effect model) and reduced beta (12-20Hz, $p=0.034$ mixed-effects model) power in the attentional lapse network, which was readily normalized by stimulation ($p=0.012$ for the theta band and $p=0.02$ for the beta band, Fig. 2d). During lapses in attention, we thus show that closed-loop stimulation rapidly rescues neural processing within the attentional lapse circuit.

In this work, we demonstrate that a core attentional lapse network can be used to both decode and control human attentive behaviour. These findings were derived from a highly unique dataset of stereotactic human intracranial recordings obtained from children undergoing surgical invasive monitoring for epilepsy localization. Through analysis of these data, we present several important first-in-human findings. First, we identify a conserved brain network responsible for the genesis of lapses in attention based on *in vivo* human recording data. Furthermore, we show that closed-loop modulation of this circuit can rapidly rescue lapses of attention in humans. Critically, we do so using computationally-efficient neural features compatible with existing implantable neurostimulation devices[21]. Direct clinical translation of our closed-loop system therefore represents an immediate follow-up to our work. Indeed, the ability to leverage individual brain rhythms to target neural circuit dysfunction represents a major scientific advance that is likely to redefine the clinical treatment of attention deficits in children. Moreover, the ability to control attention–the most fundamental of all human behaviours–carries significant ethical, moral, and legal implications for society-at-large that must be addressed in ongoing work.

Figure 1: <u>Spectral changes within a common brain network predict attentional lapses in humans.</u>

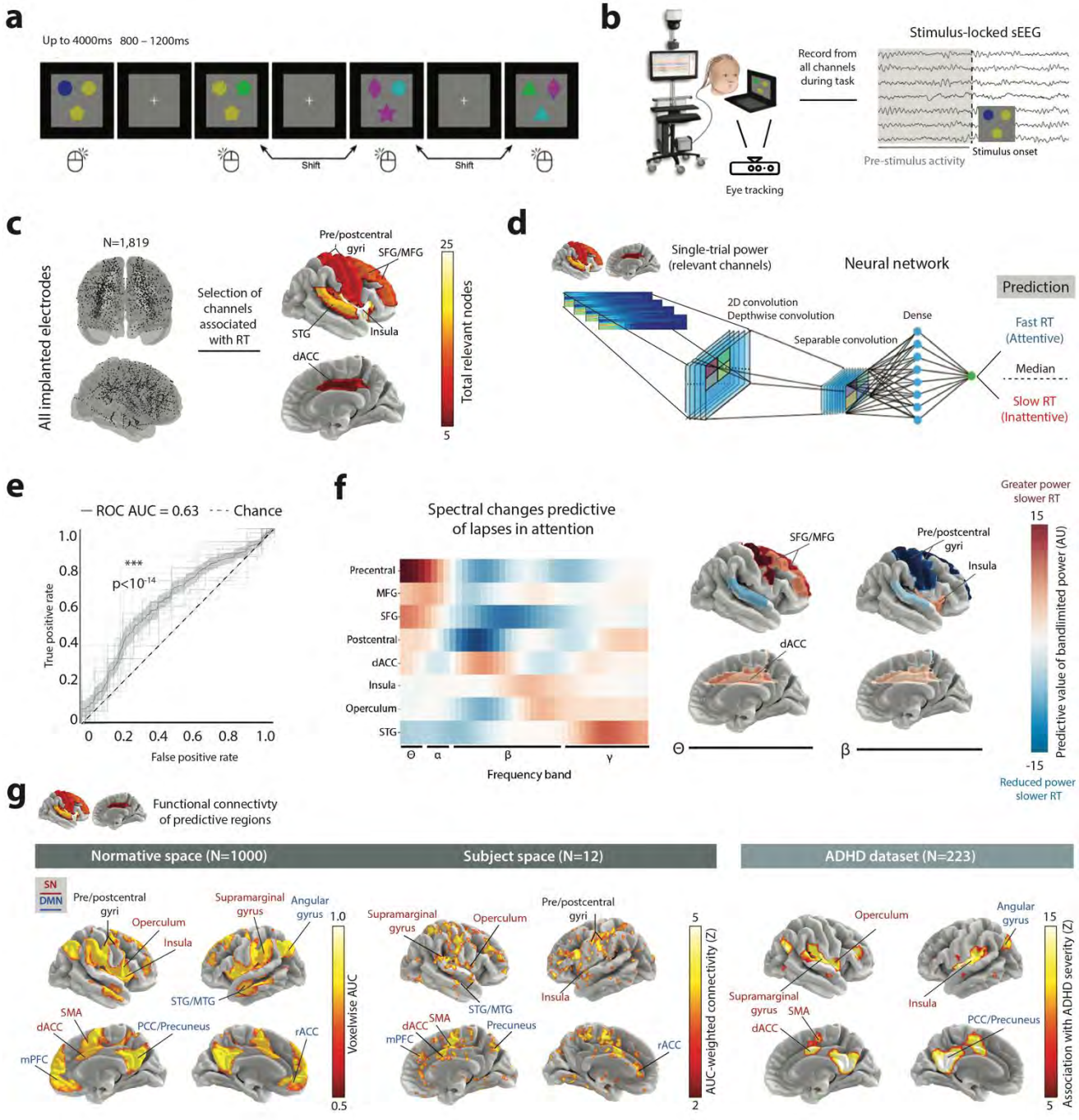

a) Schematic overview of the attentional set-shifting task. Participants (n=26) were required to match one of two target stimuli in the upper row with a lower comparator stimulus based on an implicit rule. Responses were registered through a mouse click. Attentional shift trials, in which the matching rule was changed without cueing, were randomly interspersed throughout the session to engage flexible attentional processing.

b) Collection of tandem eye tracking and pre-stimulus sEEG data during task performance.

c) Anatomic distribution of all implanted intracranial recording sites in the 26 study participants (n=1,819). Despite significant heterogeneity in implantation montages across subjects, activity within a core subset of brain regions was associated with task performance. This included the frontal cortex, insula, and anterior cingulate. Color axis represents the number of nodes associated with task performance across subjects.

d) Machine learning architecture. The CNN was trained on single-trial pre-stimulus power from a subset of predictive channels selected via logistic regression (panel c) to predict lapses in attention. To maintain balanced strata, lapses in attention were defined as trials with a predicted RT slower than the 50^{th} percentile across trials.

e) Aggregate performance of all trained classifiers showing significantly above-chance performance on unseen data obtained from a subsequent task session on another day (ROC-AUC=0.63). Shaded region represents 95% confidence interval and dashed line shows chance level. *** $p<10^{-14}$ by a bootstrap t-test.

f) Heatmap of spectral features predictive of lapses in attention. Across participants, elevated frontal theta and reduced beta power strongly predicted lapses in attention. Color axis represents the contribution of increased (red) or decreased (blue) spectral power to predicted attentional lapses.

g) Predictive brain regions converge upon a common human attentional lapse circuit. Left portion of panel shows connectivity of predictive regions computed in a large normative human connectomic dataset (n=1,000; available from http://neuroinformatics.harvard.edu/gsp/). Middle shows representation of the network in the study sample (n=12). The network consisted of nodes of two core human attentional networks, namely the SN (red) and DMN (blue). In both panels, the color axis represents the predictive value of functionally connectivity within each region. The network was independently reproduced in a cohort of children with ADHD (n=223, Right panel). Connectivity within this circuit predicted greater clinical symptom severity. dACC – dorsal ACC; mPFC – medial prefrontal cortex; PCC – posterior cingulate cortex; rACC – rostral ACC; SMA – supplementary motor area.

Figure 2: Closed-loop control of attention in children.

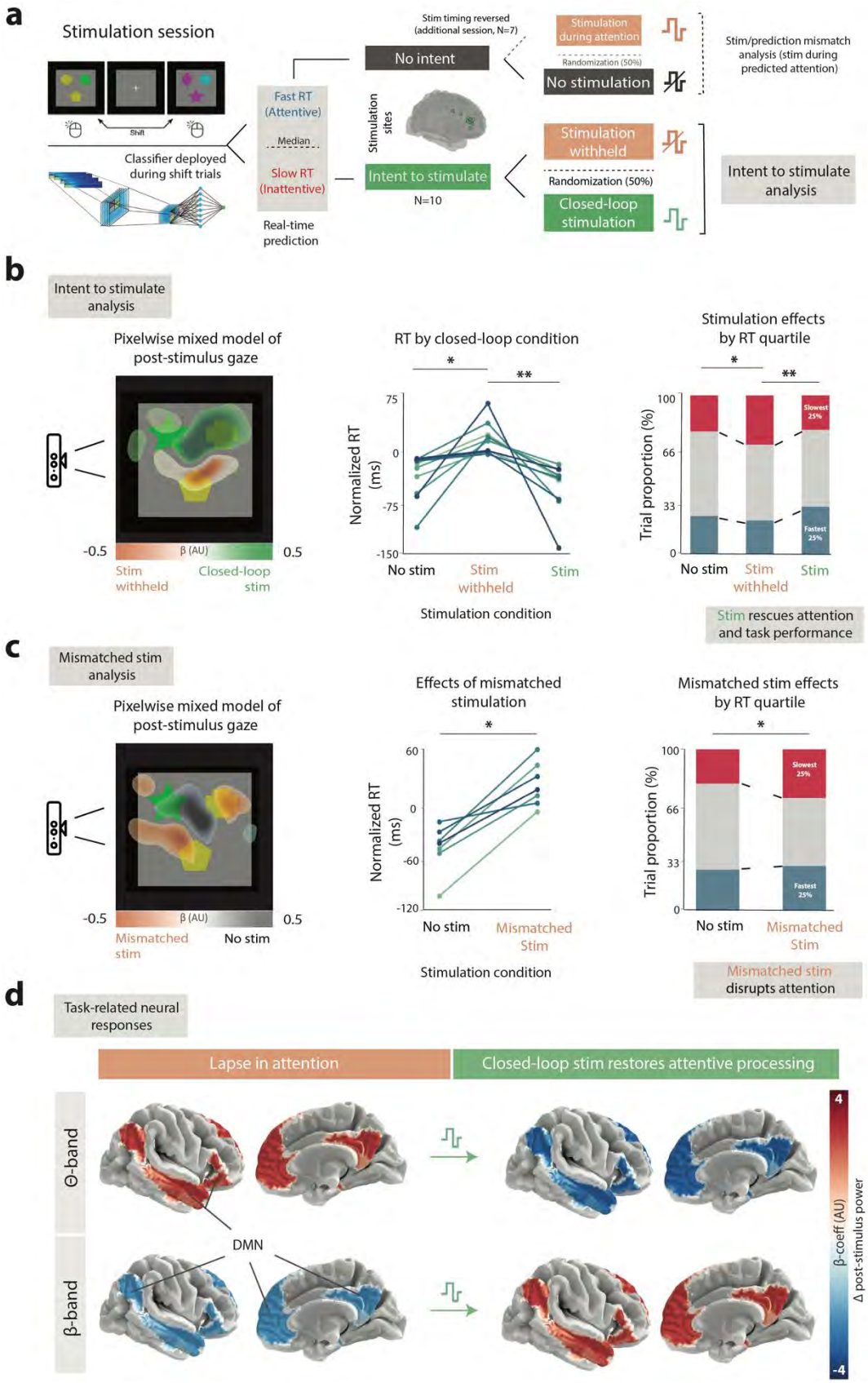

a) Overview of closed-loop stimulation trial design and distribution of stimulation sites in the ACC. Ten participants performed a closed-loop stimulation session in which the previously validated predictive models were deployed to trigger stimulation during lapses in attention. Stimulation was randomly withheld in 50% of these trials to control for the effects of attentional state on RT. Seven participants performed another session in which stimulation was instead timed to target attentive trials rather than attentional lapses (mismatched stimulation).

b) Closed-loop rescue of attention. Left of panel shows significant greater target-directed gaze with closed-loop stimulation (green) compared with attentional lapse trials in which stimulation was withheld (orange). Middle panel shows effects of closed-loop stimulation on RT during the task. Right portion of panel shows distribution of the effect across RT quartiles. During classifier-predicted lapses in attention, all participants demonstrated slowed RT that could be rescued through closed-loop stimulation. *$p<0.05$, ** $p<0.001$ (linear mixed-effects model).

c) Closed-loop attentional disruption. We performed a similar analysis as in panel b for data obtained during a separate session in which stimulation was delivered during attentive trials. Mismatched stimulation was associated with significant greater off-target gaze (left of panel, orange) and worsened task performance (middle and right of panel). * $p<0.05$ (linear mixed-effects model).

d) Closed-loop stimulation restores normative large-scale processing in the attentional lapse network. Brain surface maps show significant differences in post-stimulus neural responses in the theta (4-8Hz) and beta (12-20Hz) frequency bands. No significant differences were observed in the alpha (8-12Hz) and gamma (20-60Hz) bands. The left portion of the panel shows post-stimulus spectral characteristics of lapses in attention (no stimulation) relative to attentive trials. Comparatively, closed-loop stimulation during attentional lapses rapidly normalized theta/beta oscillatory activity within the attentional lapse network. Color axis represents linear mixed model coefficients for change in band-limited spectral power.

References

1. Jensen O, Gips B, Bergmann TO, Bonnefond M. Temporal coding organized by coupled alpha and gamma oscillations prioritize visual processing. Trends Neurosci. 2014; 37(7):357–69.

2. Lückmann HC, Jacobs HIL, Sack AT. The cross-functional role of frontoparietal regions in cognition: internal attention as the overarching mechanism. Prog Neurobiol. 2014; 116:66–86.

3. Madore KP, Khazenzon AM, Backes CW, Jiang J, Uncapher MR, Norcia AM, et al. Memory failure predicted by attention lapsing and media multitasking. Nature. 2020; 587(7832):87–91.

4. Gottlieb J, Balan P. Attention as a decision in information space. Trends Cogn Sci. 2010; 14(6):240–8.

5. Dajani DR, Uddin LQ. Demystifying cognitive flexibility: implications for clinical and developmental neuroscience. Trends in neurosciences. 2015; 38(9):571–8.

6. Uddin LQ. Cognitive and behavioural flexibility: neural mechanisms and clinical considerations. Nat Rev Neurosci. 2021; 22(3):167–79.

7. Roshani F, Piri R, Malek A, Michel TM, Vafaee MS. Comparison of cognitive flexibility, appropriate risk-taking and reaction time in individuals with and without adult ADHD. Psychiatry Research [Internet]. 2020; . Available from: http://dx.doi.org/10.1016/j.psychres.2019.112494

8. Oades RD, Christiansen H. Cognitive switching processes in young people with attention-deficit/hyperactivity disorder. Archives of Clinical Neuropsychology [Internet]. 2008; . Available from: http://dx.doi.org/10.1016/j.acn.2007.09.002

9. Reilly C, Atkinson P, Das KB, Chin RFMC, Aylett SE, Burch V, et al. Neurobehavioral comorbidities in children with active epilepsy: a population-based study. Pediatrics. 2014; 133(6):e1586-93.

10. Besag F, Gobbi G, Caplan R, Sillanpää M, Aldenkamp A, Dunn DW. Psychiatric and Behavioural Disorders in Children with Epilepsy (ILAE Task Force Report): Epilepsy and ADHD. Epileptic Disord [Internet]. 2016; . Available from: http://dx.doi.org/10.1684/epd.2016.0811

11. Cohen R, Senecky Y, Shuper A, Inbar D, Chodick G, Shalev V, et al. Prevalence of epilepsy and attention-deficit hyperactivity (ADHD) disorder: a population-based study. J Child Neurol. 2013; 28(1):120–3.

12. Cortese S, Adamo N, Del Giovane C, Mohr-Jensen C, Hayes AJ, Carucci S, et al. Comparative efficacy and tolerability of medications for attention-deficit hyperactivity disorder in children, adolescents, and adults: a systematic review and network meta-analysis. Lancet Psychiatry. 2018; 5(9):727–38.

13. Lozano AM, Lipsman N, Bergman H, Brown P, Chabardes S, Chang JW, et al. Deep brain stimulation: current challenges and future directions. Nat Rev Neurol. 2019; 15(3):148–60.

14. Arns M, Conners CK, Kraemer HC. A decade of EEG Theta/Beta Ratio Research in ADHD: a meta-analysis. J Atten Disord. 2013; 17(5):374–83.

15. Luo N, Luo X, Zheng S, Yao D, Zhao M, Cui Y, et al. Aberrant brain dynamics and spectral power in children with ADHD and its subtypes. Eur Child Adolesc Psychiatry [Internet]. 2022; . Available from: http://dx.doi.org/10.1007/s00787-022-02068-6

16. Thomas Yeo BT, Krienen FM, Sepulcre J, Sabuncu MR, Lashkari D, Hollinshead M, et al. The organization of the human cerebral cortex estimated by intrinsic functional connectivity. Journal of Neurophysiology. 2011; 106(3):1125–65.

17. Seeley WW. The Salience Network: A Neural System for Perceiving and Responding to Homeostatic Demands. J Neurosci. 2019; 39(50):9878–82.

18. Menon V, Uddin LQ. Saliency, switching, attention and control: a network model of insula function. Brain Struct Funct. 2010; 214(5–6):655–67.

19. Kucyi A, Daitch A, Raccah O, Zhao B, Zhang C, Esterman M, et al. Electrophysiological dynamics of antagonistic brain networks reflect attentional fluctuations. Nat Commun. 2020; 11(1):325.

20. Bellec P, Chu C, Chouinard-Decorte F, Benhajali Y, Margulies DS, Craddock RC. The Neuro Bureau ADHD-200 Preprocessed repository. Neuroimage. 2017; 144(Pt B):275–86.

21. Skarpaas TL, Jarosiewicz B, Morrell MJ. Brain-responsive neurostimulation for epilepsy (RNS® System). Epilepsy Res. 2019; 153:68–70.

22. Scangos KW, Khambhati AN, Daly PM, Makhoul GS, Sugrue LP, Zamanian H, et al. Closed-loop neuromodulation in an individual with treatment-resistant depression. Nat Med. 2021; 27(10):1696–700.

23. Wong SM, Arski ON, Warsi NM, Pang EW, Kerr E, Smith ML, et al. Phase Resetting in the Anterior Cingulate Cortex Subserves Childhood Attention and Is Impaired by Epilepsy. Cereb Cortex. 2021; 32(1):29–40.

24. Warsi NM, Wong SM, Suresh H, Arski ON, Yan H, Ebden M, et al. Interictal discharges delay target-directed eye movements and impair attentional set-shifting in children with epilepsy. Epilepsia [Internet]. 2022; . Available from: http://dx.doi.org/10.1111/epi.17365

25. Levantini V, Muratori P, Inguaggiato E, Masi G, Milone A, Valente E, et al. EYES Are The Window to the Mind: Eye-Tracking Technology as a Novel Approach to Study Clinical Characteristics of ADHD. Psychiatry Res. 2020; 290:113135.

26. Cheung CHM, McLoughlin G, Brandeis D, Banaschewski T, Asherson P, Kuntsi J. Neurophysiological Correlates of Attentional Fluctuation in Attention-Deficit/Hyperactivity Disorder. Brain Topogr. 2017; 30(3):320–32.

CONTEMPORARY TRENDS IN BREAST RECONSTRUCTION USE AND IMPACT ON SURVIVAL AMONG WOMEN WITH INFLAMMATORY BREAST CANCER

Ananya Gopika Nair[1], Vasily Giannakeas[2,3], John L. Semple[1,2,4,5],Steven A.Narod[1,2,3,6], David W. Lim[2,4]

[1] Temerty Faculty of Medicine, University of Toronto, Toronto, Ontario, Canada
[2] Women's College Research Institute, Women's College Hospital, Toronto, Ontario, Canada
[3] Dalla Lana School of Public Health, University of Toronto, Toronto, Ontario, Canada
[4] Department of Surgery, Women's College Hospital, Toronto, Ontario, Canada
[5] Division of Plastic, Reconstructive and Aesthetic Surgery, Department of Surgery, University of Toronto, Toronto, Ontario, Canada
[6] Institute of Medical Science, University of Toronto, Toronto, Ontario, Canada

Background: Inflammatory breast cancer (IBC) is a rare and aggressive form of locally advanced disease that accounts for 1–5% of all breast cancer diagnoses[1]. Historically, IBC was associated with a poor prognosis[2,3]. However, with advances in trimodal therapy reported 5-year survival rates and locoregional control have improved significantly[4-6].

Breast reconstruction has previously been considered a relative contraindication in IBC patients due to concerns for margin positivity, high risk of local recurrence, poor long-term survival, and potential delay of adjuvant treatments from surgical complications[7]. Given these concerns, any attempt at breast reconstruction has been recommended to occur in a delayed setting. Recent small, single-institution series have found that immediate breast reconstruction is associated with low wound complication rates and did not delay initiation of subsequent therapy[8-10]. Similarly, several larger cohort studies have found no association between breast reconstruction and worse oncologic outcomes such as local recurrence, cancer-specific survival, or overall survival[11-13].

Current surgical guidelines and recommendations propose delaying reconstruction until after definitive treatment, if at all[7]. Nevertheless, an increasing proportion of women with IBC are having breast reconstruction at the time of initial surgical therapy[12,13]. In this study, we evaluated contemporary trends and predictors of immediate breast reconstruction use among women with IBC in the Surveillance, Epidemiology, and End Results (SEER) database, and determined the impact of breast reconstruction on survival.

Methods: We conducted a case-listing session using SEER*Stat statistical software, version 8.3.6 (National Cancer Institute, Bethesda, MD, USA) to retrieve all patients with IBC (T4d) in the SEER database between 1 January 2004 and 31 December 2015. Female patients were included if they had a non-metastatic IBC diagnosis as indicated by the American Joint Committee on Cancer (AJCC) stage. Women younger than 18 years or older than 85 years of age at diagnosis, with a previous history of cancer, unknown stage, treated with breast conservation, or receiving unknown or no surgical treatment were excluded. Since patient informed consent was not required, our study was exempted from review by the Women's College Hospital Research Ethics Board. We adhered to the Strengthening the Reporting of Observational Studies in Epidemiology Statement (STROBE) guidelines for reporting observational studies[14]. For each patient, demographic data, clinicopathologic, surgical treatment, follow-up time, and vital status were collected.

To account for selection bias among women having reconstruction, a propensity-matched analysis was conducted (one reconstruction patient to three no reconstruction patients). Women were matched by year of diagnosis (within 2 years), age at diagnosis (within 2 years), surgical procedure (unilateral or bilateral mastectomy), and propensity score (demographic, clinicopathological, surgical treatment factors).

Results: We identified 4076 patients with IBC meeting the inclusion criteria with 388 (9.5%) women undergoing immediate breast reconstruction. Demographic, tumor, and treatment variables are presented in Table 1. Notably, 895 women (22.0%) chose to have a bilateral mastectomy. The mean age at diagnosis was 55.1 ± 12.5 years, with the women being predominantly Caucasian (79.5%), living in a metropolitan setting (78.7%), and earning a median income between $55,000 and $74,999 (48.9%). The mean tumor size was 6.1 ± 5.0 cm. Most patients had nodal involvement (85.2%) and high-grade tumors (60.6%) (Table 1). Women who underwent immediate breast reconstruction were younger at diagnosis compared with women who did not have breast reconstruction (49.2 years vs. 55.7 years; $p<0.0001$). These women were more likely to have a higher median income ($p<0.0001$) and live in a

metropolitan area (p<0.0001). There was no difference in tumor size, grade, nodal, ER and PR status between the two groups. Notably, 44% of women who underwent breast reconstruction also had bilateral mastectomy, while only 20% of women having a unilateral mastectomy had reconstruction (p<0.0001).

Contemporary Trends in Breast Reconstruction Use
The proportion of women undergoing immediate breast reconstruction increased from 6.2% in 2004 to 15.3% in 2015. Concurrently, the proportion of women undergoing contralateral prophylactic mastectomy (CPM) increased from 12.9% in 2004 to 29.6% in 2015 (Fig. 1).

Predictors of Immediate Breast Reconstruction Use
Compared with women diagnosed between the ages of 60 and 69 years, <40 years (odds ratio [OR] 2.32; p <0.0001), between the ages of 40 and 49 years (OR 1.86; p = 0.0004) and 50 and 59 years (OR 1.50; p = 0.02) predicted breast reconstruction use (Table 2). A high income (>$75,000) also predicted breast reconstruction use (OR 1.32, 95% CI 1.03–1.70; p = 0.027). Women living in a non- metropolitan setting were less likely to have breast reconstruction (HR 0.63, 95% CI 0.44–0.92; p <0.02). Notably, women having a bilateral mastectomy also strongly predicted breast reconstruction use (OR 2.50, 95% CI 1.98–3.14; p<0.0001). Race, tumor size and grade, nodal burden, and receptor status did not predict breast reconstruction use.

Breast Reconstruction and Breast Cancer-Specific Mortality
Among women with IBC, the crude 10-year breast cancer- specific survival (BCSS) was 62.9% for women having immediate breast reconstruction and 47.6% for women not having breast reconstruction. The cancer-specific mortality was lower among women who had not undergone reconstruction (crude HR 0.72, 95% CI 0.60–0.86; p <0.001) (Fig. 2a). In the propensity-matched analysis, 336 women having immediate breast reconstruction were matched with 1008 women without breast reconstruction (Table 3). In the matched analysis, the 10-year BCSS among women having breast reconstruction (56.6%) and no reconstruction (62.2%) was similar (adjusted HR 0.96, 95% CI 0.79–1.16; p = 0.65) (Fig. 2b).

Discussion:
In this population-based cohort study, we identified no difference in 10-year BCSS between women with and without immediate breast reconstruction. While reconstruction was previously discouraged for this population, considering their improving long-term survival and concerns for psychosocial well-being, the decision for breast reconstruction merits renewed consideration.

Historically, IBC patients treated with surgery alone had a poor prognosis, with survival time of 22 months and 5-year survival rates of 5.6%[15]. Multimodal therapy has significantly improved overall survival[7,16], with 5-year survival rates between 40–70%, and 10- and 15-year survival rates at 35% and 20–30%, respectively[4,5,17-19]. In our matched analysis, 10-year survival rates at 56.6% and 62.2% among IBC patients having and not having breast reconstruction, respectively, demonstrates that IBC patients have potential for long-term survival, even after reconstruction.

We observed a doubling in uptake of immediate breast reconstruction from 2004 to 2015 among IBC patients. The increasing rates of breast reconstruction parallel an increasing use of CPM[12,13]. This is not surprising as the consideration for breast reconstruction and CPM occur in tandem[20]. The predictors of breast reconstruction use identified in our study reveal the profile of the IBC patient currently receiving breast reconstruction and suggest disparities in access to breast reconstruction. As reported previously[12,] and observed in our data, younger women are more likely to pursue reconstruction. Similarly, living in a metropolitan area and earning a high

income were predictive of reconstruction. This keeping with prior reports that socioeconomically disadvantaged groups (rural residence, no private insurance, lower education, and income) experience barriers in accessing healthcare and breast reconstruction[12,22,23].

Previous studies have attempted to quantify the impact of breast reconstruction on oncologic and mortality outcomes in IBC patients, with mixed results[8,12,13,23,24]. Karadsheh et al. conducted a 12-year retrospective study of 12,544 IBC patients (1307 patients with reconstruction) from the National Cancer Database and found no significant difference in mortality in a matched analysis (adjusted HR 0.95, 95% CI 0.85–1.06, p = 0.37)[12]. Patel and colleagues also found no difference in survival, although their SEER analysis was restricted to women with IBC over the age of 65[24]. Chen et al. found no difference in BCSS or overall survival. In a subgroup analysis of patients who received both CPM and breast reconstruction had a decreased risk of death compared with unilateral mastectomy alone (HR 0.609, 95% CI 0.39–0.933, p = 0.02), but did not adjust for covariates[13]. In contrast, Chang et al. observed IBC patients having reconstruction had better survival than those without (~75 vs. 25% at 100 months; p = 0.04)[8]. However, 88% of reconstruction patients in the study had delayed reconstruction, and their analysis did not match for covariates. To overcome these limitations, we used a large population-based database and propensity-matched analysis and observed no difference in 10-year BCSS.

Our results contrast those of Hoffman et al., who also similarly used propensity-matched analysis with the National Cancer Database. Among 6589 women (5954 non-reconstructed and 635 immediate breast reconstruction), after matching for demographic, socioeconomic, pathologic, and clinical characteristics, immediate breast reconstruction conferred improved overall survival (HR 0.60, 95% CI 0.40–0.92; p = 0.02)[23]. Our differential results may be due to differences in the types of patients captured in the two respective population-based databases and the data that are available. Nevertheless, the overarching evidence suggests that breast reconstruction is not detrimental to survival among IBC patients. Importantly, we aimed to analyse the impact of immediate breast reconstruction on survival, given the concern that immediate breast reconstruction may delay necessary adjuvant therapy and worsen breast cancer-specific mortality[7]. Others have also reported that while immediate breast reconstruction may be associated with increased rates of surgical complications, there has not been an associated delay in initiating postoperative adjuvant radiation therapy[9,10].

There are imitations to our study, including its retrospective nature. The accuracy of the data is dependent on the health care team's documentation of patient care information. Second, the treatment assignment was not random, thus there may be latent confounding factors within the treatment decisions that were associated with other favorable prognostic factors that are not available in the SEER database. Due to limitations of the SEER registries, information on the type of reconstruction was incomplete (e.g., categories such as 'reconstruction not otherwise specified'). Patients having future delayed breast reconstruction were not captured, and our analysis was thus restricted to women having immediate breast reconstruction. Details on delivery sequence, completion and clinical response of chemotherapy, surgical complications, initiation of adjuvant therapy, endocrine therapy, and recurrences were not available.

Conclusions: We observed that while breast reconstruction use is increasing among women with IBC, there is no difference in breast cancer-specific survival between women having versus not having immediate breast reconstruction. Considering the continued improvement in survival for women with IBC, the role of breast reconstruction deserves re-exploration. With tri-modality treatment, women with IBC can be expected to live long enough to derive the psychosocial benefits offered by immediate breast reconstruction. Breast reconstruction may therefore be an appropriate consideration for IBC patients who desire the procedure.

Table 1: Predictors of immediate breast reconstruction use among inflammatory breast cancer patients

Parameter	Class	OR (95% CI)	*p* value
Age at diagnosis, years	<40	2.32 (1.58–3.38)	< 0.0001
	40–49	1.86 (1.32–2.63)	0.0004
	50–59	1.50 (1.07–2.09)	0.0176
	60–69	1.00 [Reference]	
	70–79	0.30 (0.14–0.63)	0.0017
	80–84	0.29 (0.07–1.20)	0.0879
Year of diagnosis	Per year increase	1.04 (0.97-1.11)	0.2639
Race	White	1.00 [Reference]	
	Black	1.06 (0.77–1.45)	0.7317
	East Asian	0.85 (0.33–2.23)	0.7482
	Other/unknown	1.04 (0.52–2.10)	0.9142
	Southeast Asian	0.52 (0.23–1.14)	0.1037
Income, US$	High ($75,000+)	1.32 (1.03–1.70)	0.027
	Median ($55,000–$74,999)	1.00 [Reference]	
	Low (<$55,000)	0.69 (0.49–0.98)	0.0399
Rurality	Metropolitan (≥250,000 people)	1.00 [Reference]	
	Non-metropolitan (<250,000 people)	0.63 (0.44–0.92)	0.0177
Tumor grade	I	1.00 [Reference]	
	II	0.83 (0.42–1.61)	0.5774
	III/IV	0.71 (0.37–1.37)	0.3116
	Unknown	0.78 (0.38–1.60)	0.4989
Tumor size, cm	<1	1.00 [Reference]	
	1–2	1.12 (0.44–2.81)	0.8151
	2–3	1.30 (0.54–3.17)	0.5601
	3–5	1.12 (0.47–2.64)	0.7964
	5+	1.17 (0.51–2.67)	0.7064
	Unknown	1.07 (0.45–2.54)	0.8859
Nodal status	N0	1.00 [Reference]	
	N1	0.96 (0.68–1.34)	0.7957
	N2	0.83 (0.57–1.21)	0.3255
	N3	0.79 (0.54–1.16)	0.2322
	Unknown	0.72 (0.16–3.21)	0.6668
ER status	Negative	1.00 [Reference]	
	Positive	0.79 (0.58–1.08)	0.1378
	Unknown	1.01 (0.26–3.92)	0.9888
PR status	Negative	1.00 [Reference]	
	Positive	1.33 (0.97–1.81)	0.073
	Unknown	1.00 (0.29–3.44)	0.9988
HER2 status	Negative	1.00 [Reference]	
	Positive	1.18 (0.88–1.59)	0.2675
	Unknown	0.48 (0.17–1.40)	0.1793
	Not available	0.78 (0.50–1.23)	0.2812
Cancer surgery	Unilateral mastectomy	1.00 [Reference]	
	Bilateral Mastectomy	2.50 (1.98–3.14)	< 0.0001

Abbreviations: CI: confidence interval; ER: estrogen receptor; OR: odds ratio; PR: progesterone receptor

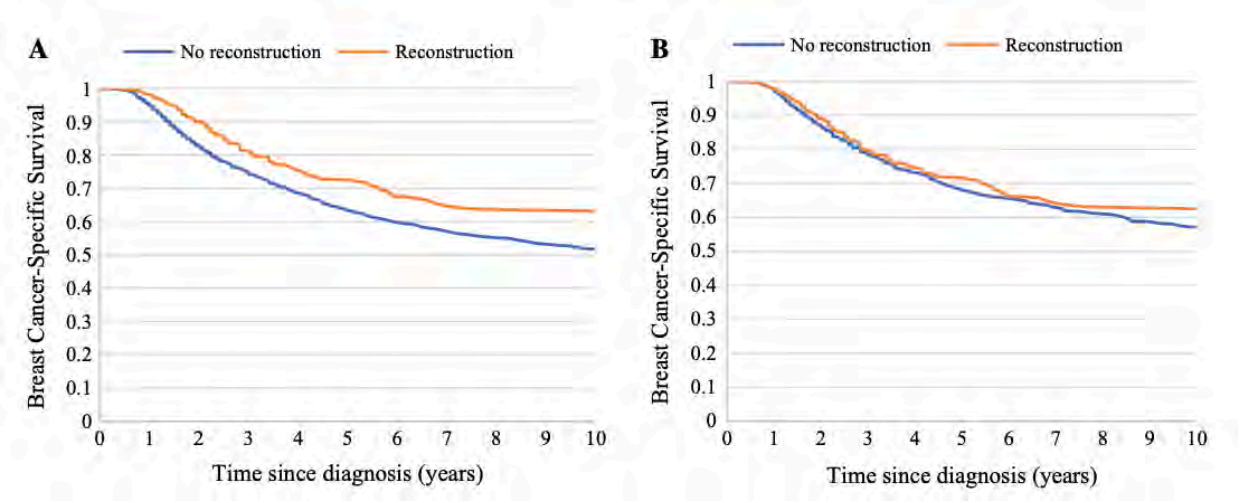

Figure 1. Breast cancer-specific survival. **A** Crude and **B** adjusted propensity-matched Kaplan-Meier curves for patients with breast reconstruction and no breast reconstruction after mastectomy in the SEER database from 2004 to 2015.

Table 2: Matching characteristics of the propensity-matched cohort (matching one reconstruction with three no reconstruction patients)

Parameter	No reconstruction	Reconstruction	*p* value
No. of patients	1008 (75.0)	336 (25.0)	
Age at diagnosis, years [mean (SD)]	50.1 (10.2)	50.1 (10.3)	0.9523
Year of diagnosis [mean (SD)]	2009.8 (3.5)	2009.8 (3.6)	0.9466
2004–2006	237 (23.5)	83 (24.7)	0.9556
2007–2009	213 (21.1)	67 (19.9)	
2010–2012	263 (26.1)	88 (26.2)	
2013–2015	295 (29.3)	98 (29.2)	
Race			0.9995
White	796 (79.0)	266 (79.2)	
Black	148 (14.7)	49 (14.6)	
Southeast Asian	27 (2.7)	9 (2.7)	
East Asian	23 (2.3)	7 (2.1)	
Other/unknown	14 (1.4)	5 (1.5)	
Income, US$			0.8171
Low (< $55,000)	163 (16.2)	58 (17.3)	
Median ($55,000–$74,999)	535 (53.1)	172 (51.2)	
High ($75,000+)	310 (30.8)	106 (31.5)	
Rurality			0.937
Metropolitan (≥ 250,000 people)	880 (87.3)	294 (87.5)	
Non-metropolitan (< 250,000 people)	126 (12.5)	41 (12.2)	
Missing	2 (0.2)	1 (0.3)	
Stage			0.8943
IIIB	814 (80.8)	272 (81.0)	
IIIC	189 (18.8)	63 (18.8)	
IIINOS	5 (0.5)	1 (0.3)	
Grade			0.8874
I	33 (3.3)	11 (3.3)	
II	285 (28.3)	88 (26.2)	
III	582 (57.7)	198 (58.9)	
Unknown	108 (10.7)	39 (11.6)	
Tumor size, cm [mean (SD)]	6.0 (4.9)	6.3 (5.1)	0.4203
< 1	15 (1.5)	7 (2.1)	0.9961
1–2	67 (6.6)	22 (6.5)	
2–3	102 (10.1)	30 (8.9)	
3–4	90 (8.9)	30 (8.9)	
4–5	73 (7.2)	25 (7.4)	
5–6	64 (6.3)	27 (8.0)	
6–7	66 (6.5)	21 (6.3)	
7–8	193 (19.1)	59 (17.6)	
8–9	57 (5.7)	19 (5.7)	
9–10	16 (1.6)	6 (1.8)	
10+	136 (13.5)	47 (14.0)	
Unknown	129 (12.8)	43 (12.8)	
Nodal status			0.9653
N1	451 (44.7)	146 (43.5)	
N2	210 (20.8)	75 (22.3)	
N3	189 (18.8)	63 (18.8)	
N0	153 (15.2)	51 (15.2)	

Table 2 (continued)

Parameter	No reconstruction	Reconstruction	*p* value
Unknown	5 (0.5)	1 (0.3)	
ER status			0.9673
Positive	526 (52.2)	174 (51.8)	
Negative	456 (45.2)	154 (45.8)	
Unknown	26 (2.6)	8 (2.4)	
PR status			0.9701
Positive	431 (42.8)	145 (43.2)	
Negative	549 (54.5)	181 (53.9)	
Unknown	28 (2.8)	10 (3.0)	
HER2 status			0.9267
Positive	209 (20.7)	70 (20.8)	
Negative	341 (33.8)	112 (33.3)	
Unknown	8 (0.8)	4 (1.2)	
NA	450 (44.6)	150 (44.6)	
Surgery			1
Bilateral mastectomy	390 (38.7)	130 (38.7)	
Unilateral mastectomy	618 (61.3)	206 (61.3)	
Follow-up time, years [mean (SD)]	5.9 (3.8)	6.1 (3.9)	0.3694
Vital status			0.4316
Alive	571 (56.6)	209 (62.2)	
Breast	373 (37.0)	112 (33.3)	
Other cancer	17 (1.7)	6 (1.8)	
Heart diseases	13 (1.3)	3 (0.9)	
Other diseases	20 (2.0)	3 (0.9)	
Unknown COD	14 (1.4)	3 (0.9)	

Data are expressed as n (%) unless otherwise specified

Abbreviations: COD: cause of death; ER: estrogen receptor; PR: progesterone receptor; SD: standard deviation; NA: not available

References

1. Menta A, Fouad TM, Lucci A, et al. Inflammatory breast cancer: what to know about this unique, aggressive breast cancer. Surg Clin North Am. (2018). https://doi:10.1016/j.suc.2018.03.009

2. Yang CH, Cristofanilli M. Systemic treatments for inflammatory breast cancer. Breast Dis. (2006). https://doi:10.3233/bd-2006-22107

3. Cristofanilli M, Valero V, Buzdar AU, et al. Inflammatory breast cancer (IBC) and patterns of recurrence: understanding the biology of a unique disease. Cancer. (2007). https://doi:10.1002/cncr.22927

4. Thoms WW, McNeese M, Fletcher GH, Buzdar AU, Eva Singletary S, Jane Oswald M. Multimodal treatment for inflammatory breast cancer. Int J Radiat Oncol Biol Phys. (1989). https://doi:10.1016/0360-3016(89)90060-6

5. Baldini E, Gardin G, Evangelista G, Prochilo T, Collecchi P, Lionetto R. Long-term results of combined-modality therapy for inflammatory breast carcinoma. Clin Breast Cancer. (2004). https://doi:10.3816/cbc.2004.n.042

6. Rehman S, Reddy CA, Tendulkar RD. Modern outcomes of inflammatory breast cancer. Int J Radiat Oncol Biol Phys. (2012). https://doi:10.1016/j.ijrobp.2012.01.030

7. Adesoye T, Lucci A. Current surgical management of inflammatory breast cancer. Ann Surg Oncol. (2021). https://doi:10.1245/s10434-021-10522-z

8. Chang EI, Chang EI, Ito R, et al. Challenging a traditional paradigm: 12-year experience with autologous free flap breast reconstruction for inflammatory breast cancer. Plast Reconstr Surg. (2015). https://doi:10.1097/prs.0000000000000900

9. Santos PM, Bogen H, Taunk NK, Tchou J, Wu L, Freedman GM. Reconstruction does not impact local control or survival outcomes in inflammatory breast cancer patients treated with trimodality therapy. Int J Radiat Oncol Biol Phys. 2019. 103(5):E23 [poster abstract].

10. Simpson AB, McCray D, Wengler C, et al. Immediate reconstruction in inflammatory breast cancer: challenging current care. Ann Surg Oncol. (2016). https://doi:10.1245/s10434-016-5554-z

11. Mortenson MM, Schneider PD, Khatri VP, et al. Immediate breast reconstruction after mastectomy increases wound complications: however, initiation of adjuvant chemotherapy is not delayed. Arch Surg. (2004). https://doi:10.1001/archsurg.139.9.988

12. Karadsheh MJ, Katsnelson JY, Ruth KJ, et al. Breast reconstruction in inflammatory breast cancer: an analysis of predictors, trends, and survival from the National Cancer Database. Plast Reconstrc Surg Glob Open. (2021). https://doi:10.1097/GOX.0000000000003528

13. Chen H, Wu K, Wang M, Wang F, Zhang M, Zhang P. A standard mastectomy should not be the only recommended breast surgical treatment for non-metastatic inflammatory

breast cancer: a large population-based study in the Surveillance, Epidemiology, and End Results database 18. Breast. (2017). https://doi:10.1016/j.breast.2017.06.002

14. von Elm E, Altman DG, Egger M, et al. The Strengthening the Reporting of Observational Studies in Epidemiology (STROBE) statement: guidelines for reporting observational studies. Lancet. (2007). https://doi:10.1016/S0140-6736(07)61602-X

15. Hance KW, Anderson WF, Devesa SS, Young HA, Levine PH. Trends in inflammatory breast carcinoma incidence and survival: the surveillance, epidemiology, and end results program at the National Cancer Institute. J Natl Cancer Inst. (2005). https://doi:10.1093/jnci/dji172

16. Anderson WF, Schairer C, Chen BE, Hance KW, Levine PH. Epidemiology of inflammatory breast cancer (IBC). Breast dis. (2006). https://doi:10.3233/bd-2006-22103

17. Li BD, Sicard MA, Ampil F, et al. Trimodal therapy for inflammatory breast cancer: a surgeon's perspective. Oncology. (2010). https://doi:10.1159/000318529

18. van Uden DJP, van Maaren MC, Bult P, et al. Pathologic complete response and overall survival in breast cancer subtypes in stage III inflammatory breast cancer. Breast Cancer Res Treat. (2019). https://doi:10.1007/s10549-019-05219-7

19. Cortazar P, Zhang L, Untch M, et al. Pathologic complete response and long-term clinical benefit in breast cancer: the CTNeoBC pooled analysis. Lancet. (2014). https://doi:10.1016/S0140-6736(13)62422-8

20. Montgomery LL, Tran KN, Heelan MC, et al. Issues of regret in women with contralateral prophylactic mastectomies. Ann Surg Oncol. (1999). https://doi:10.1007/s10434-999-0542-1

21. Lim DW, Retrouvey H, Kerrebijn I, et al. Longitudinal study of psychosocial outcomes following surgery in women with unilateral nonhereditary breast cancer. Ann Surg Oncol. (2021). https://doi:10.1245/s10434-021-09928-6

22. Schumacher JR, Taylor LJ, Tucholka JL, et al. Socioeconomic factors associated with post-mastectomy immediate reconstruction in a contemporary cohort of breast cancer survivors. Ann Surg Oncol. (2017). https://doi:10.1245/s10434-017-5933-0

23. Hoffman DI, Santos PM, Goldbach M, et al. Immediate breast reconstruction for inflammatory breast cancer: trends in use and clinical outcomes 2004–2016. Ann Surg Oncol. (2021) https://doi:10.1245/s10434-021-10404-4

24. Patel SA, Ng M, Nardello SM, Ruth K, Bleicher RJ. Immediate breast reconstruction for women having inflammatory breast cancer in the United States. Cancer Med. (2018). https://doi:10.1002/cam4.1546